Technische Universität München
TUM School of Engineering and Design

Downstream process development for the compatible solute Nγ-acetyl-L-2,4 diaminobutyric acid from saline fermentation of *Halomonas elongata*

Lea Martin

Vollständiger Abdruck der von der TUM School of Engineering and Design der Technischen Universität München zur Erlangung einer Doktorin der Ingenieurwissenschaften (Dr.-Ing.) genehmigten Dissertation.

Vorsitz: Prof. Dr. Petra Mela

Prüfer*innen der Dissertation:

1. Prof. Dr. rer. nat. Sonja Berensmeier

2. Prof. Allan S. Myerson, Ph.D.

Die Dissertation wurde am 02.05.2023 bei der Technischen Universität München eingereicht und durch die TUM School of Engineering and Design am 26.09.2023 angenommen.

Acknowledgements

Mein größter Dank geht an Prof. Dr. Sonja Berensmeier; liebe Sonja du hast mir weit über die Doktorarbeit hinaus alles ermöglicht. Ich bin dir sehr dankbar für die Jahre in denen du mich betreut hast, ich mich entfalten und viel lernen durfte und auch meinen eigenen Weg gehen konnte. Du warst da in den Momenten, als ich die Unterstützung am allermeisten gebraucht habe.
Außerdem ein wirklich großes Dankeschön an Dr. Sebastian Schwaminger – lieber Basti, ohne dich wären ich und diese Arbeit weit unter meinen und ihren Möglichkeiten geblieben. Du warst mein Bürokollege aber du bist und wirst immer mein Mentor und Vorbild sein. Vielen Dank für die vielen Ideen, den Input, die Diskussionen, die Freundschaft und deine Unterstützung in allen Lebenslagen (und für das Korrekturlesen der Arbeit).
Dann möchte ich mich bei allen Mitgliedern des HOBBIT-Projekts bedanken. Wir waren ein harmonisches und interdisziplinäres Team, es war sehr spannend ein Thema zu bearbeiten, welches so vernetzt war mit Fragestellungen anderer Fachrichtungen. Danke für die sehr gute und erfolgreiche Zusammenarbeit. Besonders gilt das natürlich für Karina Hobmeier. Liebe Karina, wir sind zusammen in das "Abenteuer Doktorarbeit" gestartet, haben die Höhen und Tiefen gemeinsam gemeistert und haben uns perfekt ergänzt. Vielen Dank, dass ich wirklich mit jeder Problemstellung zu dir kommen konnte und, dass aus unserer Zusammenarbeit eine Freundschaft geworden ist.
Diese Arbeit wäre nicht die Selbe ohne alle Studenten und Studentinnen. Vielen Dank an Berin Kackar, Jennifer Meiler, Katja Stingl, Andreas Will, Lennart Zimmermann, Leonie Wittmann, Tuan Hoang Son und Andrew Walters für eure Unterstützung.
Liebes STT-Team, mein Dank geht natürlich auch an euch alle. Ihr habt mich über die Jahre als Kollegen begleitet und ihr seid mir als Freunde geblieben: Lars, Silvia, Conny, Ljubo, Basti, Tatjana, Michi, Magdalena, Paula, Stefan D., Yasmin, Alex, Eva, Gregor, Lucía, Chiara, Leo und Marko. Ein spezielles Dankeschön an Stefan (mein Wakeboard-Buddy und ein mehr als würdiger Nachfolger für Basti in unserem Büro) für das Korrekturlesen der Arbeit und für das Auffüllen meiner (eigentlich seiner) Süßigkeitenschublade.
Ich hatte außerdem das große Glück, innerhalb und außerhalb der TUM sehr kompetente und hilfsbereite Menschen zu treffen, die mir mit Rat und Tat und Equipment zur Seite standen. Vielen Dank hier an Dr. Wilhelm Klein für die Zusammenarbeit zur Strukturanalyse

der Kristalle und an Magdalene Spicher für die Verarbeitung und Messung unendlich vieler Proben mit *ICP-MS*. Besonderen Dank außerdem an Simon Schiele für interessante Einblicke in die Kristallisation und Christian Schmidt für die Unterstützung bei Filtrationsfragestellungen.

Last but not least – Danke an meine Familie und Freunde die diesen, auch manchmal stressigen Weg mit mir gegangen sind. Vane, Sami, Lisa, Vroni und Lina, ich bin so dankbar, dass ihr immer für mich da seid und ich alles mit euch teilen kann. Liebe Mama, lieber Papa, liebe Anne und lieber Clemens, ihr unterstützt mich ausnahmslos immer und es rührt mich sehr, wie stolz ihr auf mich seid.

Abstract

Compatible solutes are water-soluble, low molecular weight, and neutrally net-charged molecules, which are accumulated by halophilic organisms to preserve the functionality of the cellular components in the saline environment. Due to their protective characteristics, these molecules offer industrial relevance as functional ingredients in cosmetic and healthcare products. Further, halophilic organisms as production strains benefit from low susceptibility to contamination as a high salt concentration is required in the cultivation process. The moderate halophilic bacteria *Halomonas elongata* is already of industrial relevance as it produces the active component ectoine. The precursor molecule in the ectoine-metabolism of *H. elongata*, *Nγ-acetyl-L-2,4-diaminobutyric acid* (γ–NADA), shows comparable protective functionalities and, thus, the potential as a valuable product. Here, we show a fermentation process to produce γ–NADA and a downstream process (*DSP*) adjusted to the saline conditions. γ–NADA proved to be a better stabilizer against thermal stress for the proteins BSA and streptavidin than the established solutes ectoine, hydroxyectoine, and trehalose. The salt-dependent accumulation of γ–NADA was shown for the mutant *Halomonas elongata* ΔectC. A reproducible batch-fermentation process was established in *lab* and small *pilot-scale* in 1 M salt conditions with a productivity of 60-70 mg L^{-1} h^{-1}. These high salt concentrations shaped the proposed *downstream process* (*DSP*). In a filtration cascade comprising microfiltration (*MF*), ultrafiltration (*UF*), and nanofiltration (*NF*), cell debris, macromolecular impurities, and salts are separated while simultaneously concentrating the target molecule γ–NADA. After a final crystallization step, γ–NADA can be obtained with high purity and recovered as a stable solid. Suitable membranes and optimal conditions for each filtration step (*MF*, *UF*, and *NF*) were identified in a membrane screening performed with a complex solution from fermentation to include all occurring separation effects and perfectly mimicked the real process conditions. The solubility of γ–NADA in different solvents and solvent mixtures was verified dependent on the temperature to establish cooling and antisolvent crystallization for the small molecule. Here, water was identified as a suitable solvent, favorite due to the aqueous environment of a biotechnological product. Further, ethanol (*EtOH*) was proven as a suitable antisolvent, significantly reducing the solubility of γ–NADA to recover the solid product. Both crystallization methods result in needle-shaped crystals of the amino acid derivative. In water, the molecule crystallizes in chiral orthorhombic space

group $P2_12_12_1$. Under the examined conditions, the cooling and antisolvent crystallization of γ–NADA reached a yield of 48 % and 86 %, respectively. All findings were combined to the purification process of γ–NADA, starting with lysate from the *pilot-scale* fermentation. After the filtration cascade, γ–NADA was successfully concentrated to 16 g L^{-1} with a purity of 45 % - suitable conditions for the antisolvent crystallization. γ–NADA was recovered as a crystalline product with a purity $>$ 94 % after a combined antisolvent and cooling crystallization. The proposed *DSP* could be the starting point for industrial production of γ–NADA.

Kurzzusammenfassung

Kompatible Solute sind wasserlösliche, niedermolekulare und neutral geladene Moleküle, die von halophilen Organismen akkumuliert werden, um die Funktionalität der zellulären Komponenten in der salzhaltigen Umgebung zu erhalten. Aufgrund ihrer schützenden Eigenschaften sind diese Moleküle für die Industrie als funktionelle Inhaltsstoffe in Kosmetik- und Gesundheitsprodukten von Bedeutung. Da für den Kultivierungsprozess halophiler Bakterien eine hohe Salzkonzentration erforderlich ist, profitiert die Verwendung dieser Organismen als Produktionsstamm von einer geringen Anfälligkeit für Kontaminationen, Das moderat halophile Bakterium *Halomonas elongata* ist bereits industriell von Bedeutung, da es den Wirkstoff Ectoin produziert. Das Vorläufermolekül im Ectoin-Stoffwechsel von *H. elongata*, *Nγ-acetyl-L-2,4-Diaminobuttersäure* (γ–NADA), zeigt vergleichbare Schutzfunktionen und damit das Potenzial als wertvolles Produkt. Wir demonstrieren hier einen Fermentationsprozess zur Herstellung von γ–NADA und einen Reinigungsprozess (*DSP*), der an die salzhaltigen Bedingungen angepasst ist. γ–NADA erwies sich für die Proteine BSA und Streptavidin als besserer Stabilisator gegen thermischen Stress als die etablierten Solute Ectoin, Hydroxyectoin und Trehalose. Die salzabhängige Akkumulation von γ–NADA wurde für die Mutante *Halomonas elongata* ΔectC gezeigt und ein reproduzierbarer *Batch*-Fermentationsprozess im Labor und im kleinen Pilotmaßstab unter 1 M Salzbedingungen mit einer Produktivität von 60-70 mg L^{-1} h^{-1} etabliert. Diese hohen Salzkonzentrationen prägen den geplanten Downstream-Prozess (*DSP*). In einer Filtrationskaskade aus Mikrofiltration (*MF*), Ultrafiltration (*UF*) und Nanofiltration (*NF*) werden Zelltrümmer, makromolekulare Verunreinigungen und Salze abgetrennt und gleichzeitig das Zielmolekül γ–NADA konzentriert. Nach einem abschließenden Kristallisationsschritt kann γ–NADA mit hoher Reinheit und als stabiler Feststoff gewonnen werden. Geeignete Membranen und optimale Bedingungen für jeden Filtrationsschritt (*MF*, *UF* und *NF*) wurden in einem Membranscreening ermittelt. Um alle auftretenden Trenneffekte zu berücksichtigen und die realen Prozessbedingungen abzubilden wurde dieses mit einer komplexen Fermentationslösung durchgeführt. Die Löslichkeit von γ–NADA in verschiedenen Lösemitteln und Lösemittelgemischen wurde in Abhängigkeit der Temperatur überprüft, um eine Kühlung und eine Antisolventenkristallisation des *small molecules* zu erreichen. Dabei wurde Wasser als geeignetes Lösungsmittel identifiziert, welches aufgrund der wässrigen Umgebung eines biotechnologischen Produkts

bevorzugt wird. Darüber hinaus erwies sich Ethanol (*EtOH*) als geeignetes Antisolvent, da es die Löslichkeit von γ–NADA deutlich herabsetzt, um ein feste Produkt zu gewinnen. Beide Kristallisationsmethoden führen zu nadelförmigen Kristallen des Aminosäurederivats. In Wasser kristallisiert das Molekül in der chiralen orthorhombischen Raumgruppe $P2_12_12_1$. Unter den untersuchten Bedingungen konnte eine Ausbeute von 48 % bzw. 86 % für die Kühl- und Antisolvent-Kristallisation erreicht werden. Alle Ergebnisse wurden zu einem Reinigungsprozess für γ–NADA kombiniert, beginnend mit dem Lysat aus der Fermentation im Pilotmaßstab. Nach der Filtrationskaskade wurde γ–NADA erfolgreich auf 16 g L^{-1} mit einer Reinheit von 45 % konzentriert - geeignete Bedingungen für die Antisolvent-Kristallisation. Nach einer kombinierten Antisolvent- und Kühlkristallisation wurde γ–NADA als kristallines Produkt mit einer Reinheit von > 94 % gewonnen. Der vorgeschlagene *DSP* könnte der Ausgangspunkt für die industrielle Produktion von γ–NADA sein.

Table of Contents

Nomenclature

Abbreviations

ACN	Acetonitrile
AFDW	Ash-free dry weight
BAM	Bundesanstalt für Materialforschung und -prüfung
BCA	Bicinchoninic acid assay
BMBF	Federal Ministry of Education and Research (Germany)
BSA	Bovine serum albumin
BTM	Dry weight biomass
cDPG	Cyclic 2,3 -diphosphoglycerate
CF	Concentration factor
CoA	Coenzyme A
Cosmo-RS	Conductor like screening model for real solvents
CSD	Crystal size distribution
DGP	Diglycerol-phosphate
DIP	di-myoinositol-phosphate
DMF	Dimethylformamide
DMSO	Dimethyl sulfoxide
DNA	Deoxyribonucleic acid
DoeA	ectoine hydroxylase
DoeB	Nα-acetyl-L-2,4-diaminobutyric acid deacetylase
DSP	Downstream process
E. coli	Escherichia coli
EctA	L-2,4-diaminobutyric acid Nγ-acetyltransferase
EctC	ectoine synthase

EctD	ectoine hydroxylase
EPS	extracellular polymeric substances
EtOH	Ethanol
H. elongata	Halomonas elongata
FBRM	Focused beam reflectance measurement
FTIR	Fourier-transform infrared
HOBBIT	Acronym for project
HPLC	High performance liquid chromatography
ICP-MS	Inductively coupled plasma - mass spectrometry
ID	Inner diameter
IR	Infrared
LB	Lysogeny broth
MeOH	Methanol
MF	Microfiltration
MM63	Minimal medium 63
MSZW	Metastable zone width
MWCO	Molecular weight cutoff
nanoDSF	Nano differential scanning fluorimetry
α-NADA	Nα-acetyl-L-2,4-diaminobutyric acid
γ-NADA	Nγ-acetyl-L-2,4-diaminobutyric acid
NF	Nanofiltration
OD_{600}	Optical density at 600 nm
PES	Polyethersulfone
PHA	polyhydroxykanoate
pO_2	Oxygen partial pressure
PVDF	Polyvinylidenfluorid
RO	Reverse osmosis
RT	Room temperature
SDS	Sodium dodecylsulfate
SEM	Scanning electron microscopy
TE	Trace element solution
TGA	Thermal gravimetric analysis

TeaABC	Ectoine uptake system
UF	Ultrafiltration
VCF	Volume concentration factor

Symbols

A	Filter area	m^2
$AFDW$	Ash free dry weight	g L^{-1}
a_i	Activity	-
c_i	Concentration	M, g L^{-1}
c_X	Cell concentration	g L^{-1}
c_S	Substrate concentration	g L^{-1}
CF	Concentration factor	-
γ_i	Activity coefficient	-
ΔG	Gibbs free energy	J
ΔH	Enthalpy	J
Δp_{TM}	Transmembrane pressure	Pa
ΔS	Entropy	J K^{-1}
Δx	Thickness of filtration layer	m
η	Viscosity	Pa s
g	Order of growth rate	-
G	Growth rate crystallization	s^{-1}
k_g	Kinetic coefficient crystallization	s^{-1}
K_S	Half saturation/affinity constante	M
L	Characteristic dimension of crystal	m
m_i	Mass	g
μ	Growth rate	h^{-1}
μ_{max}	Maximum growth rate	h^{-1}
μ_i	Chemical potential	J mol^{-1}
n	Number of cell division	-
n	Population density	m^3, kg
ν	Kinematic viscosity	m^2 s^{-1}
P_i	Permeation	-
P_i	Purity	%
p_C	Pressure concentrate-side	Pa
p_F	Pressure feed-side	Pa
p_P	Pressure permeate-side	Pa

π	Pi	-
QJ_i	Fractionation purity	-
Q_F	Feed flux	L h^{-1}
Q_P	Permeate flux	L m^{-2} h^{-1}
r	Pore radius	m
r	Nucleus size	m
r_c	Critical nucleus size	m
$\tilde{R}$	Molar gas constante	m^2 kg s^{-2} K^{-1} mol^{-1}
R_f	Fouling resistance	m^{-1}
R_i	Rejection	-
R_m	Membrane resistance	m^{-1}
	Conductivity	mS cm^{-1}
S_i	Saturation	-
t	Time	s
T	Temperature	°C, K
u	Flow velocity	m s^{-1}
τ	Residence time	s
V	Volume	mL min^{-1}
VCF	Volume concentration factor	-
x	position	m
x	mole fraction	-
Y	Yield	%

1 Introduction

Biotechnology, an industry that is becoming increasingly relevant in pharmaceutics and cosmetics, claims itself 'green'. Yet energy consumption is high to maintain the obligate sterile process conditions during production and obtain the demanded final product purity, which requires several successive steps. Here, bacteria strains called extremophiles have the advantage of growing exclusively under their 'extreme' conditions, saving the demand on sterilization steps before and after their production process, as undesirable cell growth of contaminants is inhibited. Developing efficient but energy-saving production processes is most relevant for both industries to reduce the most important factor, 'costs', in their production processes and for society to maintain a reasonable living standard. Yet, from a social perspective, the ecologic advantage of less energy consumption with constant production output should also be in focus. Worldwide climate change and ecocide threaten the existence of many human beings, fauna, and flora species and will cause high costs. This shows that ecological and economic consequences go hand in hand, which, even more, should force the development of low-energy production processes.

Another advantage of extremophilic organisms is their diverse and innovative molecule portfolio to fight the harsh conditions they can survive. The halophilic organism *Halomonas elongata* grows best in a salinity range of 0.5 - 2 M NaCl; here, contaminants do not have a chance. Thus sterility is given. One of the strategies of halophilic organisms to survive salinities is the production and accumulation of small molecules known as compatible solutes. They maintain osmotic pressure without interfering with the metabolism and protect the enzymatic cell machinery. *Halomonas elongata* accumulates ectoine as the main compatible solute, yet many of its metabolic precursors and successors show cell protective functions. One of these functional molecules is Nγ-acetyl-L-2,4-diaminobutyric acid (γ–NADA), the direct precursor of ectoine and an amino acid derivative with qualified protective abilities. Here, the interdisciplinarity of the *HOBBIT* (***H**al**o**philic **b**acteria for **Bi**ocat**a**lysis*) project allows a holistic consideration of the whole process development spectrum to bring this innovative compound, γ–NADA, to the market. Starting with metabolic understanding and development of the producer strain *Halomonas elongata*, a production and purification process is designed, and the product is finally refined by polymerization to increase the economic value. The basis

of the project is at the level of strain development. Here, the knock-out mutant *Halomonas elongata* ΔectC is engineered and forms the platform to produce γ–NADA instead of ectoine. The growth and production behavior of the strain are evaluated on a small scale and translated in a lab- and pilot-scale batch-fermentation. With the development of an efficient and salt-tolerant downstream process (*DSP*), the molecule of interest, γ–NADA, will be purified and can be both a high-value end product and a precursor for bio-polymer production [1].

Objectives

The goals of the *DSP* development for γ–NADA are both, a product as pure as possible and also a process without energy intense desalting procedures and thus, an overall reduced energy input with reduced production costs. Yet, the high NaCl concentration in the cultivation will mainly shape the *DSP* as it excludes many 'standard' separation methods from the start. Figure 1.1 illustrates the purification and desalting strategy for γ–NADA.

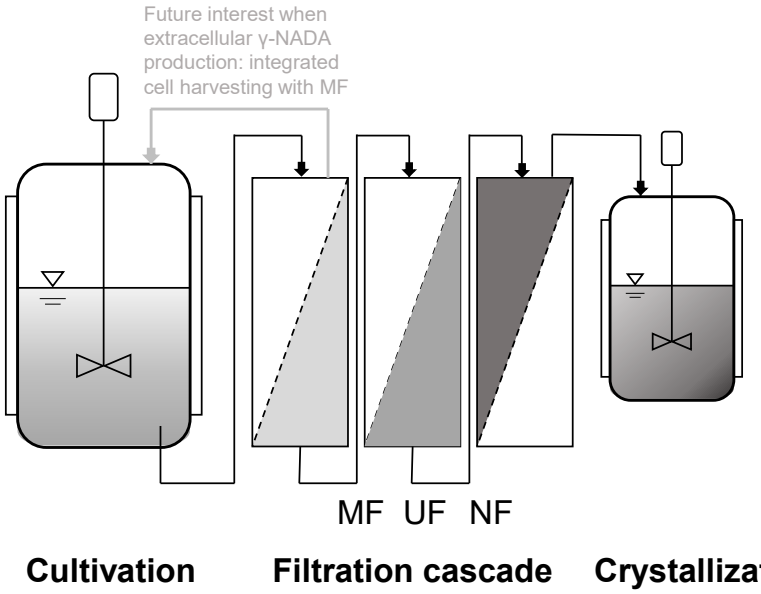

Figure 1.1: Production and purification process for the compatible solute γ–NADA. The molecule is produced in the *Halomonas elongata* ΔectC mutant, which does not accumulate ectoine, the final metabolic solute in the wildtype, but the precursor molecule γ–NADA. The *DSP* idea is a filtration cascade for the concentration and desalting of the target with a downstream crystallization to obtain a solid and pure product with a small number of process steps.

After the cultivation in high-salt media of the *Halomonas elongata* mutant, lacking of ectoine synthase to accumulate γ–NADA, in high-salt media a filtration cascade is performed. First, the microfiltration *MF* step separates cells and large, organic macromolecules. Once a *leaky*-mutant for γ–NADA is available, as it is for ectoine [2], *MF* could be integrated in the reactor

system for cell retention. Here, the risk of contamination is very much reduced, due to the salinity of the media, which would simply make a continuous setup possible. Downstream of the *MF* an ultrafiltration *UF* and nanofiltration *NF* retains dissolved organic molecules and finally concentrates γ–NADA, respectively. The whole cascade thus, must establish the suitable conditions - product concentration and impurity and NaCl content - for the following crystallization step. The target molecule will be solidified and selectively separated from the remaining NaCl in the process stream to obtain a product of maximum purity.

2 Theoretical Background

This chapter gives a profound overview of the production and purification of biotechnologically produced, organic molecules. Beside information about the used bacterial strain *Halomonas elongata* and its compatible solutes, the applied process units, cultivation, filtration, and crystallization, are also defined and described.

2.1 Halophilic organism and their metabolic products

In biotechnology, probably *Escherichia coli* (*E. coli*) and yeast such as *Pichia pastoris* are the most common microbial production strains for a bunch of products. Their metabolism is fully elucidated, genetic modifications are easy and reported and optimized strains for the production of foreign molecules are available. Yet, innovative compounds are found in more specialized, yet extremophilic organisms (reviewed in for example [3, 4]). The halophilic bacteria strain *Halomonas elongata* survives in saline environment by accumulating different osmolytes, mainly ectoine, to overcome the osmotic stress situation. This strain is already validated as potent industrial producer for ectoine, also bringing the advantage of low contamination risk and thus reducing the effort in biotechnological production [2]. These characteristics pave the way for new products from this class with modified and somehow optimized strains.

2.1.1 Characteristic of halophilic organisms and their survival strategies

Halophilic organisms are a sub-type of extremophiles which are able to live in surroundings with high salinity. They are grouped in *slightly halophilic* with a salinity range of 0.2 – 0.5 M, *moderately halophilic* in the range of 0.5 – 2.0 M, *borderline extremely* from 2.0 – 3.0 M, and *extremely halophilic* from 3.0 – 4.0 M [5, 6]. This high ionic strength forces the organism to find strategies to overcome the osmotic pressure, which results in both, adapted metabolic pathways and innovative, functional molecules to maintain enzyme stability and functionality.

These characteristics qualifies halophilic organism as interesting producer of new compounds for various industrial sectors - health care, cosmetics, chemistry. The biotechnological production benefits from the high salt content in the cultivation medium, which greatly reduces the risk of contamination in the process as the majority of microorganisms are limited to physiological salt condition. Since the maintenance of sterility in bioprocesses is associated with high energy consumption, the potential use of halophiles in open or non-sterile process set-ups could reduced arising costs to a high degree. Johnson *et al.* [7] demonstrated in their *eco-biotechnological* process, that a continuous and non-sterile production of polyhydroxyalkanoates (*PHA*) is possible over 4 years. Further, the biotechnological process with halophilic organism get out of dependence of fresh water - sea water, with a salt content of approximately 3.5 % NaCl, could be used without intense desalination. The combination of using sea water and non-sterile conditions was already shown by Yue *et al.* [8], producing bioplastics with the halophile *Halomonas campaniensis* strain.

Water is able to pass the semipermeable biological cell membrane unhindered. Yet, in unbalanced salt conditions of the intra- and extracellular space, there is always the tendency to equalize this situation by water permeating. An excess of salt in the surrounding environment, an hypertonic environment, leads to a loss of cytoplasmic water and drying out of the cell. The reverse hypotonic environment, where intracellular salinity exceeds the extracellular, causes an inward oriented water flux and with this, a burst of the cells. Here, halophilic organisms, which have to deal with a high NaCl amount (a hypertonic environment) have mainly two strategies to survive in this challenging situation - the *salt-in* and the *organic-osmolyte* strategy [9–11]. The *salt-in* strategy describes the uptake of KCl in the cell's cytoplasm to adjust the intracellular solute content to the surrounding one [12, 13]. This means that the whole protein-based metabolic machinery is aligned to the higher salt concentration to maintain cellular processes. Yet, organisms employing this strategy are restricted to a specific salinity range and cannot adapt to concentration changes in their habitat. The *organic-osmolyte* strategy overcomes this drawback as osmoprotective compounds are accumulated in the cells to reduce the osmotic pressure. These so called *compatible solutes* are mainly small, polar and water-soluble, but neutrally net-charged molecules which do not directly interact with the cell metabolism, although accumulated up to several molar concentration [14]. In response to changes in surrounding salinity, a fast release of intracellular solutes via mechanosensitive channels [15], an uptake of these compounds through transporter systems [14, 16] and biosynthesis by the organism itself is possible. These strategies make the organisms more flexible to environmental discontinuities. However the detail release strategy of the solute ectoine produced by *Halomonas elongata* is not yet fully elucidated. Vandrich *et al.* [17] recently showed that mechanosensitive channels only have a subordinate role in the ejection of ectoine.

2.1.2 Compatible solutes and their diverse application range

Several molecules are classified as compatible solutes - sugars, polyols, betaines, amino acids and their derivatives [14, 18]; all having in common to stabilize the cell system without directly intervene in the metabolism. Kunte [14] reviews that, dependent on the tolerable salt concentration, the tendency to accumulate specific compounds is as follows: less salt-tolerant organism use low-complex sugars, halotolerant accumulate sugar-polyols and halophilic organism use amino acids and their derivatives. Literature agrees, that the effect of compatible solutes on protein stability can be described by the *preferential exclusion model* [19–21]. The small molecules are excluded from the protein's vicinity and thus, by giving space to water molecules in the direct surrounding of the proteins, the hydration shell is stabilized [22, 23].

Ectoine and its relevance in industrial production with *Halomonas elongata*

One of the most industrial relevant compatible solute is ectoine. It was first described in *Ectothiorhodospira halochloris* [24], yet it is industrially produced in the halophilic bacteria strain *Halomonas elongata* in several tons per year [2]. Figure 2.1 shows the metabolic pathway in *H. elongata* wildtype, starting from aspartate in several enzymatic conversions to ectoine [25].

In the biotechnological production of ectoine in high salt medium, several strategies are performed to yield the maximum amount of ectoine (reviewed in Crowley [19]). First, with the *bacterial milking*, described by Sauer & Galinski [26], ectoine is spontaneously released from the cytoplasm by repetitive osmotic down-shocking cycles with pure H_2O. Here, a artificial hypotonic environment is created and thus, to prevent the cell from bursting, the ectoine solute content has to be lowered by excretion. Supernatant can than be further processed, while remaining, undamaged cells are recycled. As already described above, the exact excretion mechanism is still unknown, however, mechanosensitive channels appear to play a minor role [17]. Secondly, a *leaky* mutant, which permanently excretes ectoine in the surrounding medium, is applied in the production process. The deletion of several transporter genes in an ectoine uptake system (*TeaABC*) resulted in an overproducing and excreting *H. elongata* strain - the *leaky* mutant [2, 16]. Here, the main advantage is that the cell amount and target titer are decoupled, which results in a high ectoine yield per process run. Several studies showed, that ectoine stabilizes whole cell systems, but also macromolecules in general [27, 28]. Hence, research on potential application fields is diverse - process and formulation optimization [29, 30], protein folding disease [31], respiratory infections [32, 33], skin care [34, 35], and side effects in cancer therapy [36].

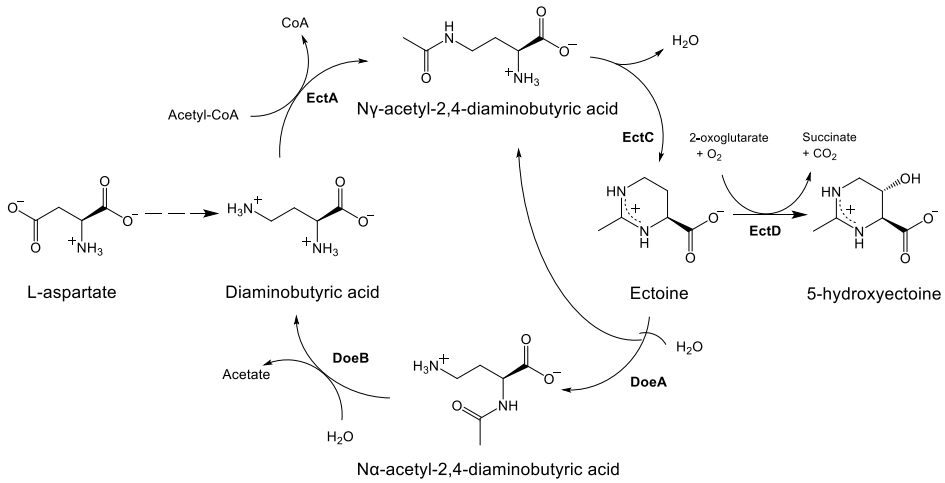

Figure 2.1: Ectoine synthesis pathway in *Halomonas elongata* wildtype, starting from L-aspartate which is converted in several steps to diaminobutyric acid. Via the enzymes L-2,4-diaminobutyric acid transaminase (*EctA*) and ectoine synthase (*EctC*) the conversion to Nγ-acetyl-L-2,4-diaminobutyric acid (γ–NADA) and ectoine is catalyzed, respectively. Ectoine hydroxylase (*EctD*) hydroxylates ectoine to hydroxyectoine, while ectoine hydrolase *DoeA*) degrades ectoine to Nα-acetyl-L-2,4-diaminobutyric acid (α–NADA). Adapted with changes from [25].

Nγ-acetyl-L-2,4-diaminobutyric acid – the auspicious precursor of ectoine

As the applicability of compatible solutes manifests itself and the market continues to grow, there is also a demand for novel, innovative compounds. In the metabolism of *H. elongata* (see Figure 2.1) several interesting candidates occur. Hydroxyectoine, which is already on the market and proofed its potential [30, 37, 38], but as well Nγ-acetyl-L-2,4-diaminobutyric acid (γ-NADA), the precursor molecule of ectoine. It was the first time extracted from *Euphorbia pulcherrima* by Liss [39] and was also found in sugar-beet [40]. The first indication, that γ–NADA can also act as compatible solute in *Halomonas elongata* and *Salmonella enterica* gave Cánovas *et al.* [41] and García-Estepa *et al.* [27], respectively. Cánovas *et al.* [42] further showed, that also isolated γ–NADA stabilizes the enzyme *rabbit muscle lactate dehydrogenase in vitro* against thermal treatment, even better than ectoine does. These findings announce a potential, which was recently shown by Ahmadi *et al.* [1]. Here, γ–NADA was polymerized and used as drug delivery system for potential dermal treatments. This thesis focus on the biotechnological production and the purification process of γ–NADA, to bring research and industrial relevance one step further.

2.2 Cultivation in biotechnological production processes

Bacteria cells reproduce by cell division. The cell concentration c_X after a certain number of cell division n can be calculated with in initial cell concentration c_{X_0} from Equation 2.1.

$$c_X = c_{X_0} \cdot 2^n \quad [\text{g L}^{-1}] \quad (2.1)$$

$$\frac{dc_X}{dt} = c_X \cdot \mu \quad [\text{g L}^{-1}\ \text{h}^{-1}] \quad (2.2)$$

$$c_X(t) = c_{X_0} + e^{\mu_{max} \cdot t} \quad [\text{g L}^{-1}] \quad (2.3)$$

Cell growth in batch bioprocesses can then be described as the change of cell concentration c_X during the process time t, defined in Equation 2.2, which is the cell concentration c_X times the specific growth rate μ. The maximum, specific growth rate μ_{max}, which is achieved in the *exponential growth phase*, can be calculated from Equation 2.3. Here, $c_X(t)$ describes the biomass content at a specific process time t and c_{X_0} the initial cell concentration. The maximum specific growth rate μ_{max} is specific for the cultivated organism. While *E. coli* and *S. cerevisiae*, two established producer strains in biotechnology, have a μ_{max} of 2 h^{-1} and 0.47 h^{-1}, respectively [43], *H. elongata*'s μ_{max} is approximately 0.4 h^{-1} in a range of 0.5 - 1.0 M NaCl [44].

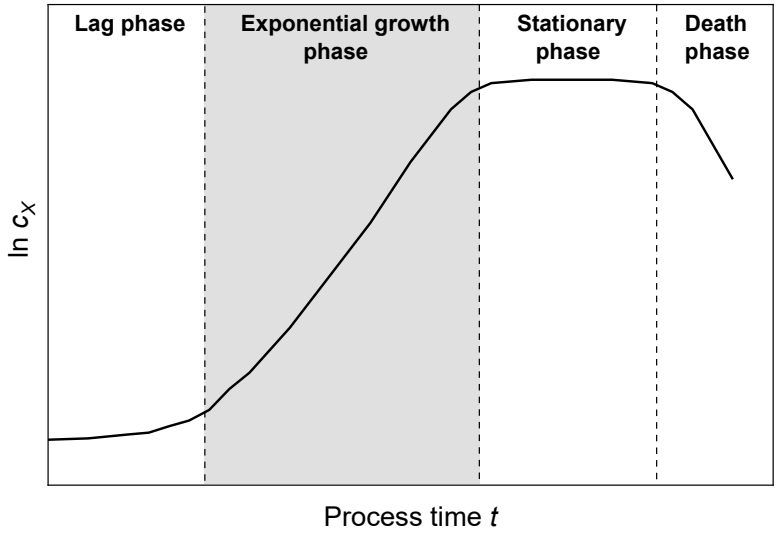

Figure 2.2: Logarithmic plot of cell growth during batch cultivation.

Figure 2.2 shows the simplified description of bacterial growth behavior in a batch-process. At the beginning of the process, inoculated bacteria cells adapt to the new environmental conditions, described as the *lag phase*. In the subsequent *exponential growth phase*, the maximum cell growth rate μ_{max} is reached. Here, required substrate and aeration is abundantly available, thus no limitations hamper cell growth. In the *stationary phase*, the provided substrate is consumed and therefor cell growth stops until the cells begin to die, which marks the start of the *death phase* [45].

2.2.1 Process methods – batch, fed-batch and continuous set-up

Growth, if no other limitations exist, is coupled to the supply of available but limited substrate c_S. This is described by the *Monod-kinetic* in Equation 2.4 with K_S being the half-saturation/affinity constant [46].

$$\mu(t) = \mu_{max} \cdot \frac{c_S(t)}{c_S(t) + K_S} \quad [\mathrm{h}^{-1}] \quad (2.4)$$

This description is coupled to two assumptions: only one substrate is limiting and no toxic by-products emerge [45]. In general three different cultivation methods, shown in Figure 2.3, exist, which differ in the way, how substrate is added. In batch cultivation (Figure 2.3a), a defined concentration of substrate c_S is provided at the beginning of the process and consumed over time, while cell concentration c_X and concentration of products c_i increase. As there is no volume stream into or out of the process, volume V stays constant. Batch cultivation is the easiest of the three methods to perform – it does not require detail knowledge about the process or complex infrastructure, the risk of contamination is reduced as no feed is added and process duration is short. Yet, final cell and product yield is limited to the initial substrate concentration which, if too high, promotes the formation of sometimes harmful by-products. The fed-batch process in Figure 2.3b is characterized by the continuous supply of substrate and medium components, described by F_{in}, thus V increases over time. Same as for the batch process, c_X, c_S and c_i change during process, however here, the limited substrate supply is overcome by the continuous feeding procedure and with this increases the productive process time. The feeding rate can be flexibly adapted and with this growth and production are triggered. Here, reactor volume and aeration are the limiting factors. The third method is the continuous process, shown in Figure 2.3c. Here, both an influx and outgoing stream (F_{in} and F_{out}), equal in volume flow, keep the volume constant. As c_S is consumed and ,with F_{out}, c_X and c_i are transported out of the process these parameter stay

constant after an defined equilibration time. This method requires the most knowledge of the cultivation process, as both streams have to be adapted to the growth and production rate and the substrate consumption. Hence, the productivity and process control are high, since a metabolic steady-state is reached and maintained. In some cases, genetic changes are favored due to the high number of cell divisions during the long-lasting process.

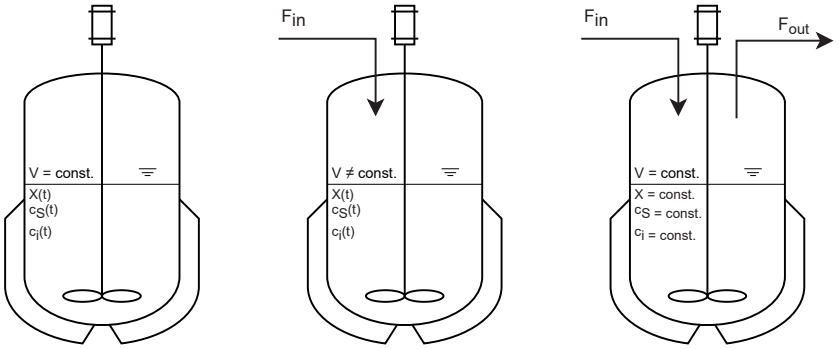

(a) Batch process. **(b)** Fed-batch process. **(c)** Continuous process.

Figure 2.3: Process description of batch (a), fed-batch (b) and continuous (c) cultivation in bioprocessing. Volume V is constant for batch and continuous processes, while it increases in fed-batch. Biomass concentration c_X, substrate concentration c_S and concentration c_i of product species i are a function over time in batch and fed-batch, while remain constant in continuous set-up. F_{in} and F_{out} describe the incoming and outcoming process streams, respectively.

Here, cultivation is performed in batch cultivation. The used producer strain *Halomonas elongata* ΔectC, a halophilic organism, requires NaCl in the medium to trigger the production of the target – the compatible solute γ-NADA. Thus, not only Glucose, the limiting substrate, has to be provided, but also NaCl is essential in the medium.

2.2.2 NaCl-dependent growth and compound production in halophilic bacteria strains

Dötsch *et al.* [44] described a growth optimum of *H. elongata* at a NaCl concentration just above 0.5 M, the tolerable range of NaCl is yet broad. Interestingly, less NaCl is even worse than a higher NaCl concentration, here growth is maintained until 3.6 M. Yet, with increasing salinity the ectoine production increases. In Hobmeier [47] the dependency is simplified to

a linear correlation with the ectoine and NaCl concentration $c_{Ectoine}$ in μmol mg^{-1}_{AFDW} and c_{NaCl} in M, respectively:

$$c_{Ectoine} = 0.837 \cdot c_{NaCl} + 0.012 \quad [\mu\text{mol mg}^{-1}] \quad (2.5)$$

Compared to the *salt-in* strategy described above in subsection 2.1.1, the *organic-osmolyte* strategy is more energy-intensive, as solutes have to be produced or actively taken up, depending on the salinity of the surrounding. Therefore, with increasing need for solutes to overcome the osmotic pressure, less energy can be used for growth which is thus reduced [10].

As just described, the production process of γ–NADA thrives from the high salt content, which brings several advantages in the upstream, yet downstream processing might be more challenging. Shown in Figure 1.1 in chapter 1, the first *DSP* step is the microfiltration. Membrane processes, as described in the following section 2.3 combine both, the selectivity to purify the desired compound and the tolerance to a high salt concentration, which is not the case for many other *DSP* units.

2.3 Membrane processes

2.3.1 Classification and filtration modes

Dependent on the applied operating pressure and the pore size of the membrane, which correlates with the *molecular weight cut off* (*MWCO*), pressure-driven membrane processes can be classified as shown in Figure 2.4.

In biotechnology, microfiltration (*MF*), with an operating transmembrane pressure (Δp_{TM}) range of 0.3 to 3 bar (see Figure 2.4), is mainly used to separate undissolved particles as organic macromolecules, whole bacteria cells and cell debris [49]. The separation is based on size exclusion of the retained particles by the pore size of the membrane, the permeating suspension is free from turbidity and easier to process in further steps. The diverse application is reviewed in [49]. In ultrafiltration (*UF*), separation is also based on the size of the species, yet pore size is smaller than in *MF*. Thus, the applicable pressure is increased to a range of 0.5 to 10 bar to overcome the bigger resistance. *UF* is for example used in food [50] and dairy

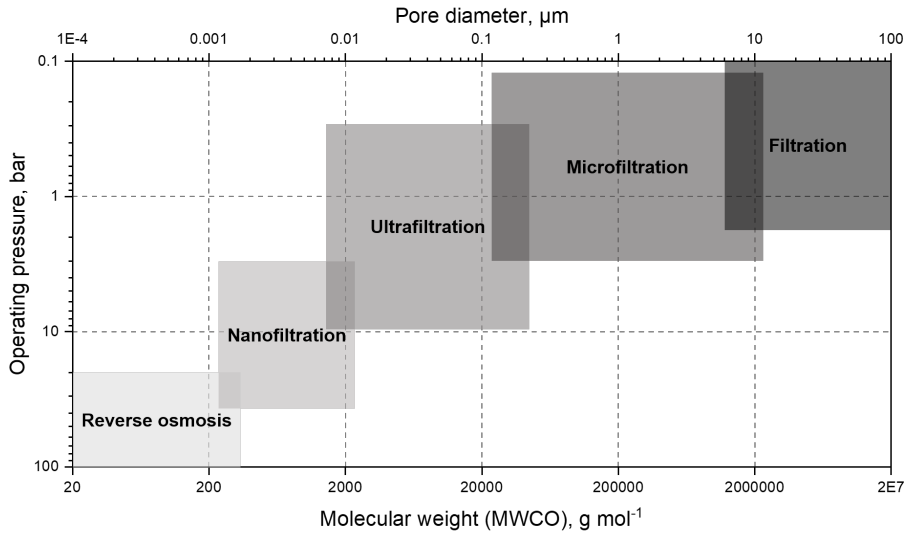

Figure 2.4: Classification of general filtration processes: reverse osmosis, nano-, ultra- and microfiltration dependent on *MWCO*, the operating pressure and the pore diameter. Adapted from [48].

production, for virus separation, discoloration and protein separation. Nanofiltration (*NF*), fills the gap between *UF* and reverse osmosis (*RO*). Here, a pressure between 3 to 30 bar is generally applied to retain small, organic molecules and multivalent ions, yet monovalent ions can permeate nearly unhindered. Electrostatic interactions between the membrane and ions retain such with a higher charge density, thus separation of differently ions is possible [51–53]. The applied pressure is highest in reverse osmosis (*RO*), which is mainly used in desalination. As any type of ions can be retained, it is a standardized process for fresh water production [48, 54]. The driving force in the introduced filtration classes is the transmembrane pressure (Δp_{TM}), which is defined as the pressure difference between the feed and the permeate side of the membrane (see Equation 2.6). In a *cross-flow* set-up, the pressure on the feed-side inlet (p_F) and on the concentrate-side outlet (p_C) is averaged and the pressure on the permeate side p_P is subtracted. For polymeric membranes, as used here, p_P is close to zero and can be usually neglected.

$$\Delta p_{TM} = \frac{p_F + p_C}{2} - p_P \quad \text{[bar]} \quad (2.6)$$

The filtration process can be run in basically two different modes, namely *dead-end* and *cross-flow* filtration. The general principles are illustrated in Figure 2.5. In *dead-end* filtration, the feed stream flows vertically through the membrane and the retained species build up an ever

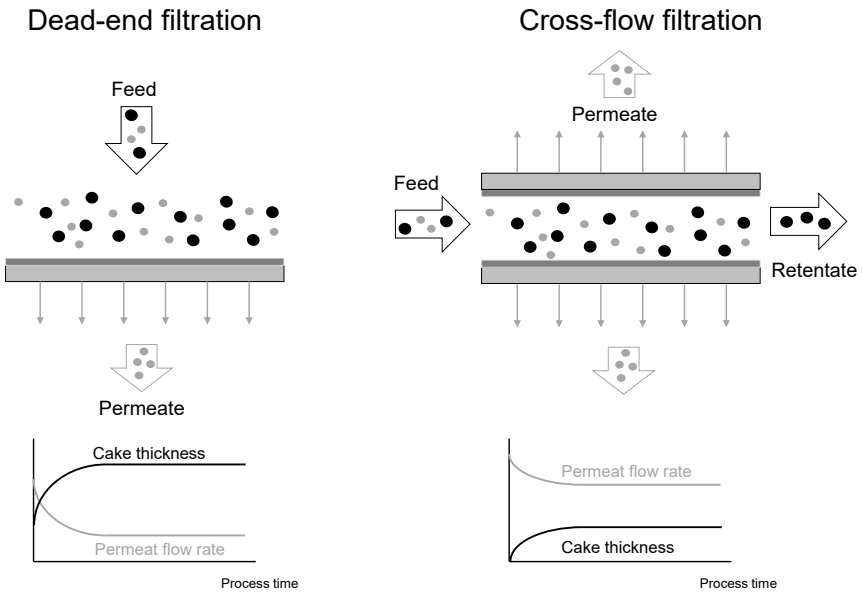

(a) *Dead-end* filtration. **(b)** *Cross-flow* filtration.

Figure 2.5: Filtration modes in biotechnological processes.In *dead-end* filtration the feed pass through the membrane vertically, whereas in *cross-flow* filtration the feed flows tangentially over the membrane. Adapted from [55]

.

growing filter cake (see Figure 2.5a). This is the limiting factor in the process, hence at some point in the process, the filter cake becomes too dense and thick and permeate flux decreases to an uneconomic level. With ongoing process, the filter cake itself plays the major role in retaining the present particles, thus the retention behavior might change over time. *Cross-flow* filtration, on the other hand, is performed with a tangential feed flow, while retentate can be recirculated in the feed tank (see Figure 2.5b). Same as in *dead-end* filtration, a filter cake results, yet the shear forces of the tangential feed flux keep the thickness and density constant at a certain, reduced level.

$$P_i = \frac{c_{i,P}}{c_{i,F}} \quad [\text{-}] \quad (2.7)$$

$$R_i = 1 - P_i = 1 - \frac{c_{i,P}}{c_{i,F}} \quad [\text{-}] \quad (2.8)$$

The quantitative estimation of the filtration performance is given by the amount of permeated or retained target species, the permeation P_i and rejection R_i, respectively. P_i is defined by

the species concentration in the permeate $c_{i,P}$ divided by the species feed concentration $c_{i,F}$ (see Equation 2.7. If the membrane is unrestricted permeable for the observed species, $c_{i,P}$ is equal to the concentration in the feed $c_{i,F}$, thus P_i is 1. When in contrast, the target is rejected by the membrane, $c_{i,P}$ is depleted and P_i reduced to minimum zero. Here, rejection of the observed species R_i, given in Equation 2.8, approaches 1.

Membrane modules in *cross-flow* filtration

The tangential feed flux in a *cross-flow* filtration is realized with different modular configurations of the membrane. The principles of a *flat-sheet* membrane, a *spiral wound* module, and a *hollow fiber* module are shown in Figure 2.6.

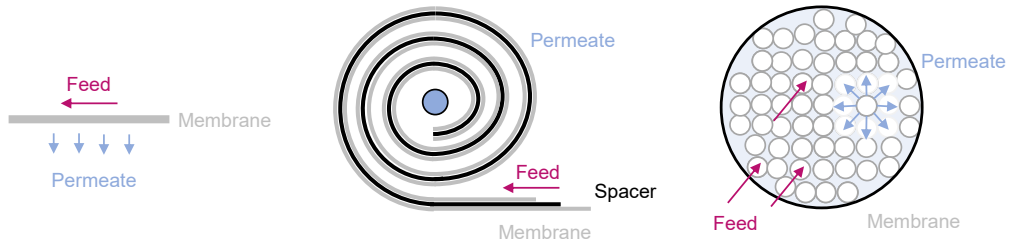

(a) *Flat-sheet* membrane. **(b)** *Spiral wound* module. **(c)** *Hollow fiber* module.

Figure 2.6: Membrane modules for *cross-flow* filtration.

.

As described above and shown in Figure 2.5, in *cross-flow* filtration, the feed flows tangentially accross the membrane. In a filtration set-up with *flat-sheet* membranes (see Figure 2.6a) the permeate is collected on the reverse side of the membrane (see Figure 2.6a). *Flat-sheet* membranes are easy in use, yet lack of sufficient, effective membrane area. This is overcome by the wrapped construction of the *spiral wound* module in Figure 2.6b. In the *spiral wound* configuration, two *flat-sheet* membranes, placed on top of each other and separated by a spacer (membrane envelop), are wrapped around a tube which collects the permeate. The feed flows across the outward facing side of the membrane and the permeate is collected and transported at the spacer-facing side. The *spiral wound* module is considered as scaled-up and more industrially relevant version of the *flat-sheet* membrane [56, 57]. In *hollow fiber* modules, tubular membranes with a thin diameter (hollow fibers) are bundled in parallel. Here, the feed is pumped through the inner part of the hollow fiber and permeat is collected on the outside and channeled through the housing (Figure 2.6c). Wang & Liang [58] review several implementations and optimizations of this design in detail. The compact structure of the bundled fibers enables a dense packing and thus, a very high surface area [59, 60] and the tube-like design makes the processing of a feed with high solid concentration possible. Yet,

irreversible fouling and breaking of the hollow fibers is a drawback and the flux is generally lower compared to *flat-sheet* configurations [60]. Although, the packing density is less than for *hollow fibers*, *spiral wound* modules reach a high surface to volume ratio. It is also less prone to fouling since cleaning is more straight forward. Yet, due to the wrapped packing, *spiral wound* modules cannot process a feed stream with a high solid concentration. Nevertheless, Schwinge *et al.* [61] mention, that the industrial relevance of this set-up results from the good compromise in it's operation.

2.3.2 Filtration effects and fouling mechanisms

Separation effects

The exclusion of species due to membrane filtration can be mainly categorized in the separation due to physical hindrance and due to charge effects. Several models to describe and predict these effects are available, as for example reviewed in Wang *et al.* [62]. Schmidt *et al.* [63] considers *steric* and *Donnan exclusion* which is extended with the *dielectric exclusion* in Epsztein *et al.* [53], Vezzani & Bandini [64], Roy & Warsinger [65], and Bandini & Vezzani [66].

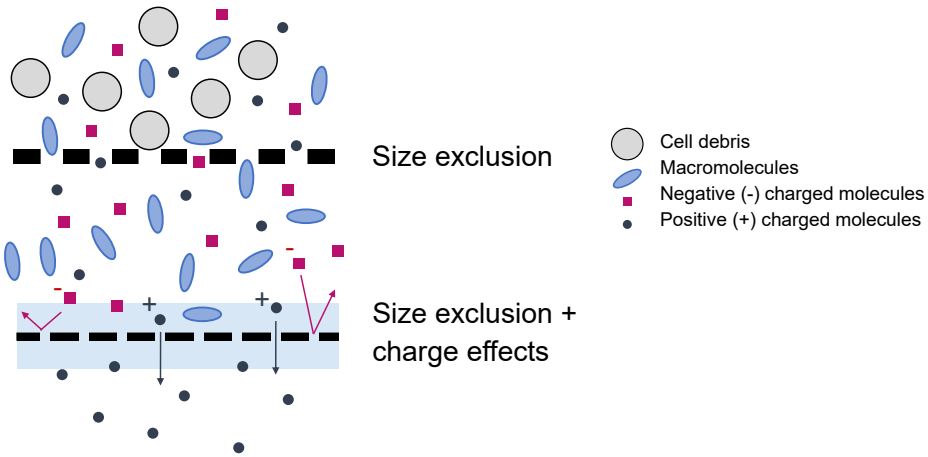

Figure 2.7: Separation effects occurring in the filtration of cultivation suspensions for the separation of γ-*NADA*.

Figure 2.7 images the separation effects of the main components which might be present in a feed from biotechnological cultivation – cell debris, macromolecules, charged ions and molecules. The bigger the pore size, as it is for *MF* and *UF*, the exclusion of molecules mainly results from the steric hindrance of the membrane pores. Here, the hydrated size of feed components are relevant [53], yet also the shape plays a role. With decreasing pore size,

the charge of the membrane becomes relevant for the separation principle. This is described as *Donnan effect* [67–69]: equally charged molecules or ions are repelled while oppositely charged ones are attracted and able to pass. This is more pronounced for multivalent ions, than for monovalent ions, making a separation according to the valency of ions possible in *NF* [53]. The smaller the ions and the higher the net charge, the effect increases [53]. However, for uncharged molecules still the steric rejection is the dominant effect [70]. For charged amino acids, Timmer *et al.* [71] further describes, that when the *Donnan effect* is the dominant separation effect, the salt composition and the target concentration additionally have an effect on rejection. Further, the separation is more efficient, the more is the separation dependent on *Donnan exclusion* [71]. Yet, Schaep *et al.* [72] demonstrated that *Donnan exclusion* does not completely explain the observed retention of different salt types, but the higher the diffusion coefficient of the salt species, the less retention is observed with charged *NF* membranes supporting diffusion as contributing separation effect. *Dielectric exclusion* also influences charged molecule, yet independent of their charge compared to the membranes charge [65]. Here, the pore 'forces' the ion to strip off its hydration shell to pass the membrane, which results in a energy barrier hindering the permeation [73]. The charge effects are mainly described for *NF*, yet also for *UF* it is reported [71]. The size exclusion is present in all areas of filtration and is also the main separation effect for uncharged molecules, independent of size. Here, the transport of uncharged molecules occurs by convection and by diffusion, due to the pressure difference (Δp) and concentration differences (Δc) in pressure-driven membrane processes, respectively [72].

The above described effects can be manipulated in filtration processes by pH, ionic strength and the corresponding choice of salt (reviewed in [74]). The effect of electrostatic interactions in *UF* on protein separation, manipulated by ion species, ion concentration, and pH, is summarized in the review by Rohani & Zydney [75]. The pH influences the net charge of the protein and with this the interaction with the charged membrane surface. A high surface charge of the protein promotes either attractive or repulsive forces and with this a higher retention. Same is reported for the charge of the membrane - higher charge means a higher retention. Increasing the ionic strength reduces this effect due to shielding effects of the buffer ions. Yet, the higher the valencies of the used salt species, the higher is the charge effect on the protein and with this the effect on the separation process. Further aspects discussed in [75] are the surface charge distribution of the protein and the changes in surrounding conditions while membrane transfer.
As mentioned above, charge effects become more dominant in *NF*. Teixeira *et al.* [76] showed the complex interplay of the charge of the membrane (triggered by the pH) and the retention of different ion species of different valencies. At pH approximately the isoelectric point (pI) of the membrane, the retention of ion species is low as the membrane has a neutral net charge and separation is only dependent on the size of the molecule. Increasing the pH results in

a highly charged membrane surface, however, shielding effects of opposite charged ions at high ionic strength reduce this effect. The charged surface groups of the membrane take up more space due to restructuring, repulsive effects and narrow the effective pore size which, as a consequence, reduces the permeate flux and increases the retention of the ions. Further, the high retention increases the osmotic pressure at the membrane surface, which reduces the effective pressure in the filtration process and thus decreases the permeate flux (Equation 2.9). Yet, the effect of pH and salt on the filtration performance in *NF* is very dependent on the solute properties and membrane characteristics, as reviewed and pointed out in Luo & Wan [74]. The effect of pH on the salt retention is highly dependent on the salt species: the retention of salts of equivalent anions and cations (e.g. KCl, $MgSO_4$) decreases with the pH shifting to the *pI* of the membrane, while the retention of salts with different ion valency (e.g. $MgCl_2$) can be described with a sigmoidal curve over the pH range. This is explained by the more dominant repulsive effects (*Donnan effect*) between ions with higher valencies and the membrane. In general, the retention of salts decreases with increasing salt concentration. The effect of the ionic strength on the retention of salts can also be explained by the *Donnan effect* and a shielding performance of the equally charged ions to reduce the surface charge of the membrane [74]. The effect of both on amino acids occurs to be more complex. Here both, the charge of the membrane and the charge of the molecule are affected by variations in pH and ionic strength [77]. Further, a mixture of different amino acids and inorganic salts is less predictable, as both types of molecules, dependent of their charge at respective pH, contribute individually to shielding and electrostatic effects. Further, described by Van der Bruggen *et al.* [78], the polarity of molecules can play a role in the separation, since the dipole orients towards the membrane and eases the permeation.

Fouling mechanism

One parameter, which mainly defines the economic performance of the filtration process is the permeate flux (Q_P), defined in Equation 2.9:

$$Q_P = \frac{r^2 \cdot \Delta p_{TM}}{8 \cdot \eta \cdot \Delta x} \qquad [\mathrm{L\ m^{-2}\ h^{-1}}] \quad (2.9)$$

Here, r is the average pore radius of the membrane, η the viscosity of the filtration suspension and Δx the thickness of the filtration layer. Q_P is further dependent on the above described driving force Δp_{TM}; with increasing Δp_{TM}, Q_P rises. A higher Δp_{TM} consequently results in an increased Q_P but promotes fouling phenomena that now influence the layer thickness

Δx. This mechanism is the main reasons for a reduced permeate flux over the process time. As Figure 2.8 shows, concentration polarization denotes the formation of a concentration

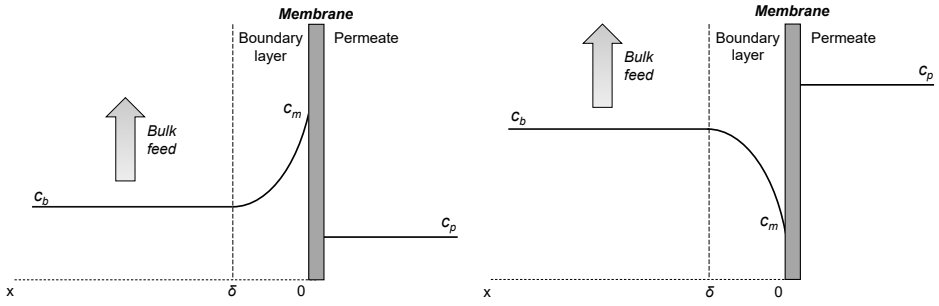

(a) Retained species. **(b)** Permeated species.

Figure 2.8: Concentration profile with concentration polarization: (A) mass transfer limited by the membrane and (B) mass transfer limited by the boundary layer. Adapted from [79].

gradient upstream of the filtration membrane. With ongoing convective transport of the target species to the membrane surface, yet when rejected, the concentration close to the membrane increases related to the bulk concentration (Figure 2.8a). Due to the resulting diffusive back transport in the bulk, a stationary boundary layer occurs. On the other hand, if the species permeates the membrane unhindered, concentration close to the membrane is reduced (Figure 2.8b). These concentration profiles work against the driving force for the separation, Δp_{TM}, and thus reduce Q_P, as shown in Equation 2.9. Beside, concentration polarization enhances membrane fouling, which describes the reduction of the membrane performance due to accumulation of suspension particles on or in the membrane's surface and pores. Here can be distinguished between *particulate fouling*, *organic and inorganic fouling* and *biofouling*, according to the causing foulants (reviewed in [80, 81]). Figure 2.9 illustrates the four different models which describe the general appearing particulate fouling mechanism.

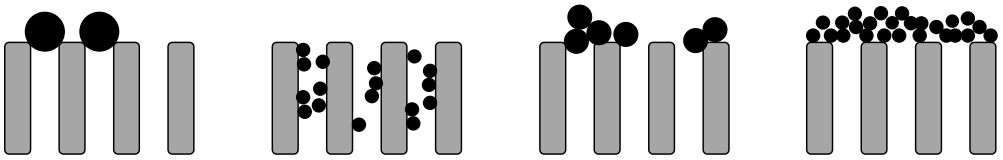

(a) Complete. **(b)** Standard. **(c)** Intermediate. **(d)** Cake layer.

Figure 2.9: Types of pore blocking which initiate fouling in membrane filtration: Complete (a), standard (b) and (c) intermediate blocking, which promote cake layer formation (d) as next fouling step. Adapted from [82]

The complete pore blocking in Figure 2.9a describes that the plugging of pores by one particle each, while in the standard pore blocking model in Figure 2.9b particles penetrate the pores and deposit on the pore opening and the inner pore wall. The intermediate pore blocking in Figure 2.9c is characterized by the coagulation of particles which than can block the pores. As can be seen in Figure 2.9d, the final stage of fouling is the formation of a cake layer, which, with ongoing process, can form a gel layer [82]. Yet, these layers differ in their characteristics as composition and charge, which could be a reason of a higher filtration resistance cause by the gel layer compared to a filtration cake [83]. An increasing hydraulic resistance due to the reduced permeability and the progressive deposition of foulants can further compact the filter cake and results in a decreasing permeate flux Q_P. Further, the filter cake itself shapes the membrane performance, as pore size and permeability for several species change [80, 82, 84, 85]. *Organic* and *inorganic fouling* traces back to dissolved species which adsorb and precipitate on the membrane surface. Last, *biofouling* is an additional but independent problem in bioprocesses, which occurs from bacterial attaching and growth in and on the membrane. Here, the main components of the bio-film are the cell mass and extracellular polymeric substances (*EPS*). More hydrophobic membranes with a rough surface preferably tends to bio-film building [86, 87].

As a result, the control of fouling is the key challenge in filtration as fouling is responsible for the declining process efficiency due to reduction of Q_P. Here, understanding the mechanism and adjusting the process conditions can counteract the fouling effects: preconditioning the feed suspension, modifying the membrane material, finding optimal operating conditions, and introducing and establishing suitable cleaning protocols [85].

2.4 Crystallization

In the γ–NADA production process, introduced in chapter 1, the filtration cascade is followed by a final crystallization step. Crystallization's goal is the formation of solid and, at the same time, pure substances from solution, melts, and even gas phase. Here, special requirements to the final product are aimed. Success, yield, and efficiency of the crystallization process are dependent on several solution conditions which are described and referred to the process in the following.

2.4.1 Solution properties in crystallization

The crystallization of a specified solute from a solution is dependent on the properties of the solute suspension at given conditions - temperature, pressure, solvent composition. Here, phase diagrams (see Figure 2.10) define the equilibrium composition of a solution under certain conditions, yet solubility of the target molecule simplifies the explanation and is mainly used to describe the behavior of the solute in solution. It is defined by the amount of solute which can be maximally dissolved in a saturated solution at given temperature and given solvent [88].
Thermodynamically, crystallization results from the disparity of the chemical potential $\Delta\mu_i$ of the respective target molecule *i* in saturated and supersaturated solutions (see Equation 2.10). Here, a_i and a_i^* are the activities of the component in the given and saturated solutions, respectively, with $\tilde{R}$ the molar gas constant and T the temperature at given conditions. When a_i exceeds a_i^*, supersaturation is reached (compare Figure 2.10).

$$\Delta\mu_i = \mu_i - \mu_i^* = \tilde{R}T \cdot ln\frac{a_i}{a_i^*} \quad [\text{J mol}^{-1}] \quad (2.10)$$

$$S_{a,i} \equiv \frac{a_i}{a_i^*} = exp\left(\frac{\Delta\mu_i}{\tilde{R}T}\right) \quad [-] \quad (2.11)$$

$$a_i = \tilde{x}_i \cdot \gamma_i \quad [-] \quad (2.12)$$

$$S_{x,i} = \frac{\tilde{x}_i}{\tilde{x}_i^*} = \frac{x_i}{x_i^*} = \frac{c_i}{c_i^*} \quad [-] \quad (2.13)$$

The saturation $S_{a,i}$ can be calculated from the quotient of the two activities a_i and a_i^* (see Equation 2.11). Since the activity a_i is defined by the molar fraction of the compound $\tilde{x}_i$ and the activity coefficient γ_i (see Equation 2.12) and γ_i can be approximated to equal values when supersaturation is low, the saturation $S_{x,i}$ simplifies to the quotient of the molar fractions $\tilde{x}_i$ or mass fractions x_i or concentration c_i in saturated and supersaturated solutions (see Equation 2.13) [89].

Figure 2.10 shows the temperature-dependent solubility of a species. According to Equation 2.13, the solubility curve describes the state at which $S_{x,i}$ is 1 as in a saturated solution

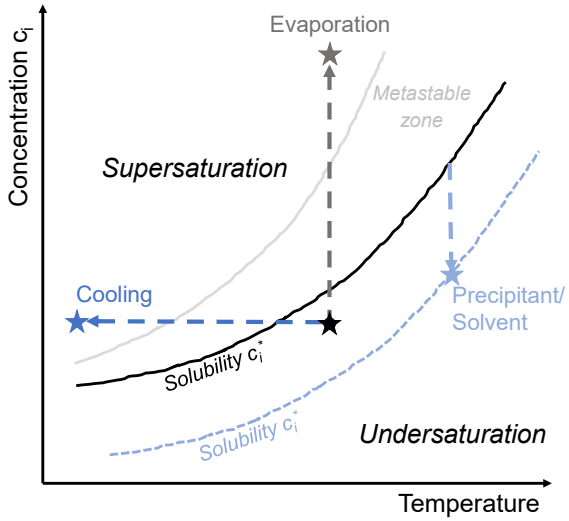

Figure 2.10: Temperature-dependent solubility curve of exemplary solute in solution. Dashed arrows describe the changes of equilibrium condition due to main crystallization methods, namely *cooling crystallization*, *evaporation crystallization* and crystallization due to adding a precipitation agent or solvent (*antisolvent crystallization*).

c_i and c_i^* are equal. Supersaturation and undersaturation describe the conditions at which the maximum solubility is exceeded and undercutted, respectively. To initiate nucleation (subsection 2.4.2), which is the initial step for crystallization, the solubility curve has to be exceeded until a critical supersaturation is generated. In a crystallization process, the condition is achieved by various methods – cooling, evaporation and adding precipitation reagents and solvents. Which method is the most suitable is dependent on the molecule to be crystallized, the solvent(s), the applicability in the process, the required characteristics of the solid product and the behavior of the system during crystallization.

Crystallization methods

In *cooling crystallization*, supersaturation is generated with cooling the solution to a critical temperature, shown by the dashed dark blue arrow in Figure 2.10. For many substances, solubility is temperature-dependent, which can be described by the enthalpy of the system, defined as Gibb's free energy in Equation 2.14. If dissolving of a solute is an endothermic

system ($\Delta G > 0$) the solubility increases with increasing temperature, if endothermic ($\Delta G < 0$) solubility decreases.

$$\Delta G = \Delta H - T\Delta S \quad [\mathrm{J}] \quad (2.14)$$

Thus, in a system where temperature positively affects solubility, *cooling crystallization* can be applied. Yet, remaining solubility of the solute at the cooled temperature and the steepness of the solubility curve establish if this method is applicable in the process. Here, less remaining solubility and a very steep slope are favored for a maximum yield and efficiency.

As the name suggests, in *evaporation crystallization*, the supersaturated state is reached through evaporation of the solvent. Here, concentration of the solute increases, shown by the grey dashed arrow in Figure 2.10, and exceeds the solubility at some point. As evaporation is a relative energy intense method, *evaporation crystallization* is mainly suitable for solvents with a high vapor pressure. In application, vacuum is used to reduce the evaporation temperature.

The addition of a second solvent (*antisolvent*) or a precipitation agent changes the solubility conditions for the solute, shown by the shifted solubility curve in Figure 2.10. With this, the current state slides into the supersaturation area, making a nucleation and a further crystallization possible. In *antisolvent crystallization* the decision for a suitable solvent pair is crucial – the first one in which the solute has an high solubility and another one with a poor solubility. Further important, the chosen solvents have to be miscible.

2.4.2 Nucleation and crystal growth

Regardless of the chosen crystallization method, supersaturation, a non-equilibrium state, has to be reached to induce nucleation and further crystal growth.

Nucleation

The first step in a crystallization process – nucleation – can be either a spontaneous process or can be triggered by external input like seeding material. According to this, the nucleation mechanism is divided into *primary* and *secondary nucleation*, describing the nuclei formation

from a supersaturated, crystal-free solution and from a solution spiked with already existing parent crystals of the target species, respectively. *Primary nucleation* can be further subdivided in *homogeneous* and *heterogeneous nucleation*. Both describe the nuclei formation from a solution with completely dissolved target species, yet in *heterogeneous nucleation* surfaces of foreign substances (equipment walls, dust, impurities) ease the initiation of nucleation of the target. *Secondary nucleation* takes place when nucleation is induced by crystal surfaces, crystal interaction and abrasion of crystals, but from the same material as the solute. Thus, seeding of crystal material is advantageous in the process, as less supersaturation is required to initiate secondary nucleation compared to primary nucleation.

$$\Delta G = \Delta G_S + \Delta G_\nu = 4\pi r^2 \sigma + \frac{4}{3}\pi r^3 \Delta G_\nu \qquad \text{[J]} \quad (2.15)$$

Theory, describing the initial nucleation bases on *homogeneous nucleation*, though mainly *heterogeneous nucleation* exists in reality. In classical nucleation theory (*CNT*), which traces back to Volmer & Weber [90] and Becker & Döring [91], a pre-nucleation cluster has to exceed a critical nucleus size r_c to result in a stable nuclei. Therefor a energy barrier ΔG^* must be overcome which is shown in Figure 2.11. The equation for ΔG is given in dependence of r in Equation 2.15 [92].

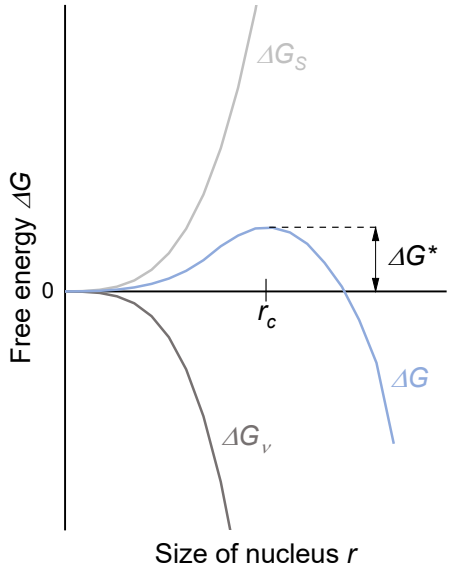

Figure 2.11: Gibbs free energy ΔG barrier dependent on the size of nucleus. For a successful nucleation and thus crystallization, a 'critical nucleus´size r_c has to be overcome. Adapted from [92].

The solidification during crystallization reduces ΔG as the state is more stable compared to the supersaturated state of the molecule in solution. Thus, as shown in Figure 2.11, ΔG_ν, the free energy change for phase transformation, becomes negative with increasing nucleus size. In contrast, the free energy change of surface formation ΔG_S increases with increasing

r. When a critical nucleus size r_c is reached, a stable nuclei can be formed and crystal growth can occur, resulting in the decrease of ΔG. Yet, classical nucleation theory is bound to several assumptions, summed up in for example Erdemir *et al.* [93] and Karthika *et al.* [94], and often does not match experimental observations. Another widely accepted theory is the *two-step model* of nucleation, initiated by Gebauer *et al.* [95]. Here, the solute molecules in solution first arrange to a cluster of sufficient dimension [95] and then form a stable nuclei due to structure-forming rearranges. The difference of both nucleation pathways is shown in Figure 2.12.

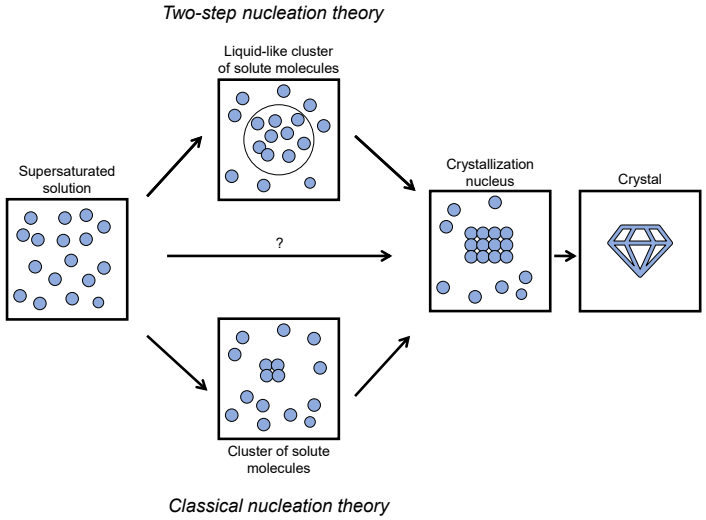

Figure 2.12: Schematic comparison of classical nucleation theory *CNT* and *two-step* model of nucleation. Adapted from [92]

.

The applicability of the *two-step model* was described for both, the crystallization of proteins and for the crystallization of small molecules by Knezic *et al.* [96] and Zaccaro *et al.* [97], respectively. Further, the second step of the model appears to be the rate limiting, as shown for proteins by Pan *et al.* [98].

As already mentioned, nucleation theories describe *homogeneous nucleation*, yet mainly *heterogeneous nucleation* occurs. Here, the activation energy barrier, as shown in Figure 2.11, is lowered and thus, nucleation and with this crystallization can take place at much lower supersaturation conditions. This effect depends on the contact angle between the solution and the foreign material – less than 180° results in a decreased energy barrier [92].

Process control and methods to induce nucleation

Nucleation takes place if the solution is supersaturated under the given conditions, yet nucleation does not always happen spontaneous. Here, the *metastable zone*, shown in Figure 2.10, defines a state range where solubility is already exceeded but nucleation does not happen due to kinetic barriers. In this range, nucleation can be controlled, which is important in crystallization processes in which standardized sizes and morphology have to be maintained to gain a constant product quality. Working in the *metastable zone* prevents nucleation-dominated crystallization which often results in many but small crystals. Smaller crystals complicate downstream handling like filtration, yet are sometimes desired as for example bioavailability increases with increasing surface. Since supersaturation in the *metastable zone* is not sufficient for spontaneous nucleation it requires a initiator to lower the energy barrier and start nucleation. A method to caused nucleation is *seeding* of the solution. In industrial crystallization mainly *homogeneous seeding* is performed by adding seeding material of the target solute which ensures process control due to control over crystallization start, less batch-to-batch variations, control over particle size and shape and preventing undesired phases. To maintain a good process control during seeding, 0.1-1.0 % of seed crystals are recommended in a slurred mixture with the appropriate solvent [92].

Crystal growth

When a stable nuclei is formed, the actual crystal formation is initiated. Here, the solute molecules arrange in a highly ordered lattice structure which results in defined crystal systems, for example summed up and described in [99]. The process of crystal growth is defined by the transport of the solute molecules to the crystal surface, by an equilibrium of subsequent adsorption, diffusion and desorption effects and by the final insert of the molecule in the crystal system. Here, the growth can be both, diffusion limited and limited by the rate of molecule integration.

$$G = k_g \cdot (S_i - 1)^g \qquad [\mathrm{s}^{-1}] \quad (2.16)$$

The growth rate G is dependent on the saturation S_i (see Equation 2.13) and further defined by a kinetic coefficient k_g and the order of the growth rate g, see Equation 2.16. Since the growth rate of the different crystal faces differ, the *crystal habit* occurs in various geometries. As shown in Martin *et al.* [100], the molecule of interest, γ–NADA, crystallizes in an external needle shape demonstrating clearly the differences in growth kinetics of the crystal faces. Yet, the outer appearance is not mandatory, additives and impurities [101, 102], solvents [103] and process conditions can significantly change the *crystal habit* and with this affect

the purification process of the solidified molecule. This has to be taken into account regarding the purification of γ–NADA with a crystallization step. NaCl, as one of the main impurity, shapes the surrounding conditions and thus, as described above, might have an effect on the final crystalline product. Here, the upstream filtration cascade has to ensure both, a first purification of the product stream and sufficiently adjusted and constant conditions in which crystallization of the target is feasible.

2.4.3 Operation modes and reactor set-up in crystallization

The in subsection 2.4.1 described critical reactions, nucleation and crystal growth, can be controlled through the operation modes and technical implementation. As shown in Figure 2.13, the crystallization process can be performed in batch or continuous mode, while two main set-ups are used for the continuous workflow, mixed suspension mixed product removal reactor (*MSMPR*), comparable to the continuous stirred tank reactor (*CSTR*) [104], and the plug-flow reactor (*PFR*).

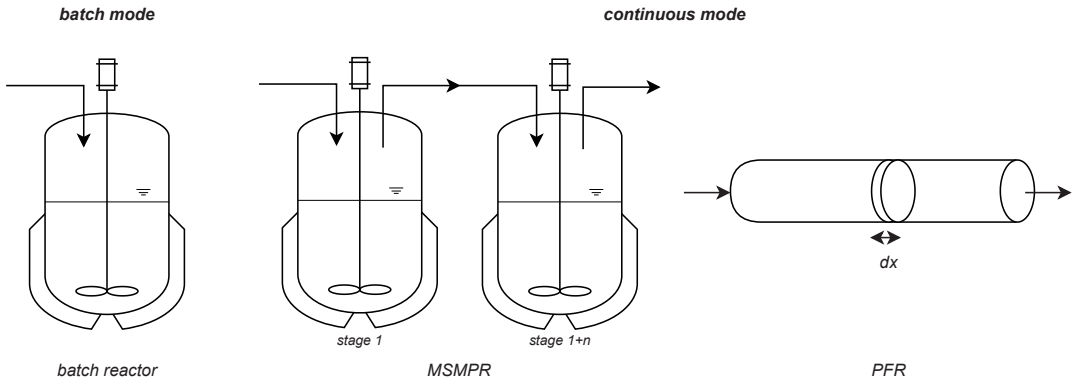

Figure 2.13: Schema of the batch and continuous operation modes for crystallization. A batch reactor mainly is designed as a stirred tank reactor, while in the continuous set-up several designs are dominant - mixed suspension mixed product removal (*MSMPR*) and plug-flow reactors (*PFR*).

When crystallization is performed in batch mode, the crystallization solution with defined amount of solute is initially transferred in the reactor and supersaturation is created, dependent on the crystallization method described in subsection 2.4.1. Due to the ongoing crystallization process, the concentration of solute in solution decreases over the process time (see Figure A.1a). This relation is given in the population balance in Equation 2.17 with

the following assumptions: a well mixed reactor with constant volume in the process, crystal growth rate and crystal size are decoupled, and size of nuclei is insignificant [105].

$$\frac{dn}{dt} + G\frac{dn}{dL} = 0 \tag{2.17}$$

The population density n, which describes the amount of crystals per unit volume of size, changes over time t and over the crystal size L, dependent on the crystal growth rate G (see Equation 2.16).
In continuous crystallization, mainly two set-ups are in relevant use: mixed suspension mixed product removal reactors (*MSMPR*), exemplarily reviewed in Eren *et al.* [106], and plug-flow reactors (*PFR*) [107, 108] . In both, a continuous inlet and outlet stream, define the concentration of the solute in the reactor. In a *MSMPR* the solute concentration in each stage n reaches a steady-state, yet decreasing with the number of stages (see Figure A.1b), while in the *PFR* the concentration decreases over the length of the reactor (see Figure A.1c in Figure A.1) [109]. The balance equation of the *MSMPR* for 1 to n stages is given in Equation 2.18 and Equation 2.19, respectively [110].

$$G_1\tau_1 \cdot \frac{dn_1}{dL} = 0 \tag{2.18}$$

$$G_n\tau_n \cdot \frac{dn_n}{dL} = n_{n-1} \tag{2.19}$$

The crystallization process in a multi-stage *MSMPR* is described as a function of the crystal growth rate G, the residence time τ, and the change of n over the crystal size L (compare [110]). It is further assumed, that each stage operates at a steady-state, no agglomeration or breaking of the crystals happens, an equal crystal size distribution *CSD* of final product and in the reactor is given, and a solid-free feed stream enters stage 1 [110]. The balance equation of a *PFR* is given in Equation 2.20 [108].

$$u_x\frac{dn}{dx} + G\frac{dn}{dL} = 0 \tag{2.20}$$

Here, the change of the amount of crystals n is dependent on both, the crystal size L and the position x in the tubular *PFR*. Further, the growth rate G and the flow velocity u_x are relevant. Here, no radial or axial dispersion is assumed, the growth rate does not change with the crystal size and, as for the *MSMPR*, no agglomeration or breaking of the crystals happen.

Especially pharmaceutical products have to reach certain requirements to ensure a reproducible standard of quality. However, batch processes exploit their simplicity and versatile application, the drawback of batch-to-batch variations, long process times and possible scale-up difficulties guides industrial production more and more to continuous processes [106]. The main advantage of a continuous crystallization set-up is the high process control to reach the characteristic quality and quantity of the desired product. The supersaturation level in the steady-state of each stage (in a *MSMPR*) and at the inlet of a *PFR* [111, 112] and the residence time [113, 114] control the final crystal size and crystal size distribution (*CSD*) in the process: a higher supersaturation generates a smaller *CSD*, however the longer the residence time τ in the reactor, the more dominant is the crystal growth compared to nucleation, resulting in larger crystals [106, 115]. Also the yield can be improved with more stages in the *MSMPR* cascade and longer residence time, yet, as Li *et al.* [116] points out, an acceptable compromise of yield and efficiency needs to be found. Recycling of the outlet streams could further improve the process yield, however, as Alvarez *et al.* [110] explains, might reduce the final purity. Different continuously operated reactor set-ups further optimize the quality of the product. Each stage n of subsequent *MSMPR* can be operated at individual conditions [110, 116]. Variations in *PFR* designs, also create different crystallization conditions over the length of the reactor: Kwon *et al.* [107] divided the *PFR* in sections with different crystallization temperatures to control shape and size in the process while Alvarez & Myerson [108] used a (non-conventional) plug-flow reactor design with multiple injection points for antisolvent to control the final product size, however, the effect is dependent on the molecules' kinetic. Also Ferguson *et al.* [117] limits the successful crystallization in an antisolvent *PFR* set-up (shown with benzoic acid) to molecules with a fast kinetic, due to the short residence time. Thus, the decision for the best operation mode is also dependent on the molecule. Complex reactions might require a batch process, although, industrial use moves to continuous workflows.

3 Material and Methods

3.1 Material

Table 3.1: List of chemicals.

Product	**Supplier**
Streptavidin	Serva
α-Amylase from *Aspergillus oryzae*	Sigma-Aldrich
Acetonitrile	VWR International GmbH, Darmstadt, Germany
Agar	Carl Roth GmbH & Co. KG, Karlsruhe, Germany
BSA	Carl Roth GmbH & Co. KG, Karlsruhe, Germany
BH_3O_3	AppliChem GmbH, Darmstadt, Germany
cDPG	provided by bitop
$CoCl_2 \cdot 6\,H_2O$	Merck KGaA, Darmstadt, Germany
$CuSO_4 \cdot 5\,H_2O$	Carl Roth GmbH & Co. KG, Karlsruhe, Germany
DGP	provided by bitop
DIP	provided by bitop
EDTA	Carl Roth GmbH & Co. KG, Karlsruhe, Germany
Ethanol	VWR International GmbH, Darmstadt, Germany
$FeSO_4$	Carl Roth GmbH & Co. KG, Karlsruhe, Germany
fiorin	provided by bitop
Hydrochloric acid	VWR International GmbH, Darmstadt, Germany
Glucose	AppliChem GmbH, Darmstadt, Germany
Glycerol	Merck KGaA, Darmstadt, Germany
Hydrolysed ectoine material	provided by bitop
Isopropanol	VWR International GmbH, Darmstadt, Germany

$KAI(SO_4)_2 \cdot 12\,H_2O$	Merck KGaA, Darmstadt, Germany
KH_2PO_4	Carl Roth GmbH & Co. KG, Karlsruhe, Germany
K_2HPO_4	Carl Roth GmbH & Co. KG, Karlsruhe, Germany
Methanol	VWR International GmbH, Darmstadt, Germany
$MgSO_4$	Carl Roth GmbH & Co. KG, Karlsruhe, Germany
$MnSO_4 \cdot H_2O$	VWR International GmbH, Darmstadt, Germany
$(NH_4)_2SO_4$	Merck KGaA, Darmstadt, Germany
$NiCl_2 \cdot 6\,H_2O$	Merck KGaA, Darmstadt, Germany
P-3-ultrasil 112	Ecolab Deutschland GmbH, Monheim, Germany
P-3-ultrasil 75	Ecolab Deutschland GmbH, Monheim, Germany
Pierce™BCA Protein Assay Kit	Thermo Fischer Scientific Inc., Waltham, United States
Potassium hydroxide	VWR International GmbH, Darmstadt, Germany
Sodium chloride	AppliChem GmbH, Darmstadt, Germany
Sodium hydroxide	Carl Roth GmbH & Co. KG, Karlsruhe, Germany
Trehalose	Carl Roth GmbH & Co. KG, Karlsruhe, Germany
Tris base	VWR International GmbH, Darmstadt, Germany
Tryptone	Carl Roth GmbH & Co. KG, Karlsruhe, Germany
Yeast extract BioChemica	AppliChem GmbH, Darmstadt, Germany
$ZnSO_4 \cdot 7\,H_2O$	Merck KGaA, Darmstadt, Germany

Table 3.2: List of consumables.

Name	**Specification**	**Supplier**
Aluminium oxide pans		Thepro GbR, Heinsberg, Germany
Cuvettes		
HPLC columns	YMC-Pack Polyamine II; 12nm, S-5 μm, 250 x 4.6 mm ID	YMC Europe GmbH, Dinslaken, Germany
MF flatsheet membrane	FR	Synder filtration, Vacaville, United states
MF flatsheet membrane	V0.2	Synder filtration, Vacaville, United states

NF flatsheet membrane	NFW	Synder filtration, Vacaville, United states
NF flatsheet membrane	DK	GE Water & Process Technologies, Trevose, United States
NF flatsheet membrane	DL	GE Water & Process Technologies, Trevose, United States
NF flatsheet membrane	FilmTec™ NF	DuPont Water Solutions, Wilmington, United States
NF flatsheet membrane	FilmTec™ NF270	DuPont Water Solutions, Wilmington, United States
NF flatsheet membrane	Dairy NF™	Hydranautics – A Nitto Group Company, Oceanside, United States
NF flatsheet membrane	XN45	TriSep Corporation, Goleta, United States
Prometheus NT.48 capillaries	nanoDSF High Sensitivity Grade	NanoTemper Technologies, Munich, Germany
UF flatsheet membrane	ST	Synder filtration, Vacaville, United states
UF flatsheet membrane	MQ	Synder filtration, Vacaville, United states
UF flatsheet membrane	LY	Synder filtration, Vacaville, United states
96 well microtiter plate	Nunc™	Thermo Fischer Scientific Inc., Waltham, United States

Table 3.3: List of equipment.

Name	**Specification**	**Supplier**
Bioreactor 2L	Biostat® B plus	Sartorius AG, Göttingen, Germany
Bioreactor 50 L	LP75	Bioengineering AG, Zurich, Switzerland
Diffractometer	STOE	Stadivari, Darmstadt, Germany

Disc separator	CSA 8-06-476	GEA Group AG, Düsseldorf, Germany
Filtration plant	Cube80 VA	SIMA-tec, Schwalmtal, Germany
Freeze dryer	Alpha 1-2 LDplus	Martin Christ Gefriertrocknungsanlagen GmbH, Osterode am Harz, Germany
FTIR	ALPHA spectrometer	Bruker Optics, Ettlingen, Germany
HPLC	1260 Infinity II	Agilent Technologies, Inc., Santa Clara, United States
Incubator	MaxQ™2000	Thermo Fisher Scientific Inc., Waltham, United States
Incubator	WiseCube	witeg Labortechnik GmbH, Wertheim, Germany
nanoDSF	Prometheus NT.48	NanoTemper Technologies, Munich, Germany
pH-meter		Mettler-Toledo GmbH, Gießen, Germany
Photometer	Biospectrometer basic	Eppendorf AG, Hamburg, Germany
Raman	SENTERRE spectrometer	Bruker Optics, Ettlingen, Germany
SEM	JSM-6390	JEOL GmbH, Freising, Germany
Thermal gravimetric analysis	TGA/DSC 3+	METTLER TOLEDO, Columbus, United States
Ultracentrifuge	Beckman LE-70 Optima, rotor 70-Ti	Beckman Coulter, Krefeld, Germany

3.2 Methods

In the following sections, the experimental methods for the characterization of the molecule (subsection 3.2.1) and the process development for *USP* (subsection 3.2.2, subsection 3.2.3) and *DSP* (subsection 3.2.4, subsection 3.2.5) are described in detail. The analysis to determine the characteristic data is described in subsection 3.2.6. The following student researchers were involved in parts of the experimental work as part of their studies: Andrew Walters, Jennifer Meiler, Lennart Zimmermann and Leonie Wittmann.

3.2.1 Characterization of Nγ-acetyl-L-2,4-diaminobutyric acid

XRD measurements

X -ray single crystal diffraction (*XRD*) was kindly performed by Dr. Wilhelm Klein from the Chair of Inorganic Chemistry with Focus on Novel Materials (TUM) to investigate the crystal structure of γ-NADA after cooling crystallization. Crystals were put on a glass fiber and, if necessary, cooled with a N_2 gas stream. Measurements were performed at 100 K, 200 K and 300 K with a *STOE StadiVari (Damrstadt, Germany)* (Mo Kα radiation) diffractometer, a *DECTRIS PILATUS 300K (Baden-Dättwil, Switzerland)* detector and an *Oxford Cryostream 800 system (Oxford, United Kingdom)*. Detailled description can be found in [100].

Raman and Fourier-transform infrared (*FTIR*) spectroscopy

Raman (*Raman SENTERRA spectrometer (Bruker Optics, Ettlingen, Germany)*) and *FTIR* spectroscopy (*ALPHAspectrometer with matching platinum attenuated total reflection (ATR) module, Bruker Optics, Ettlingen, Germany*) for the characterization of the γ-NADA crystals were performed as described in Martin *et al.* [100]. For both methods, three independent measurements were conducted at room temperature with dried γ–NADA crystals from cooling crystallization and 24 scans per sample. Raman measurements were performed with 488 nm excitation wavelength and 40 mW laser power. The baseline was subtracted with the rubber band method in the *OPUS* software.

***nanoDSF* for the determination of the thermal stability of proteins**

Thermal protein stability was determined according to the changes in proteins' autofluorescence during denaturation with *nanoDSF* (*Prometheus NT.48, NanoTemper Technologies, Munich, Germany*). Three different proteins, namely bovin serum albumin (BSA), amylase from *aspergillus oryzae* and streptavidin, were tested in a concentration of 0.5 g L^{-1}, solely and in the presence of several compatible solutes. Beside the here in detail discussed ectoine, hydroxyectoine, γ-NADA from cooling crystallization (see subsection 3.2.5) and trehalose also di-nyo-inositol 1,1-phosphate (DIP), cyclic bisdiphosphoglycerat (cDPG), diglycerol phosphate (DGP) and fiorin were used, all in a concentration of 0.5 M. Further two buffer conditions, 10 mM potassium phosphate (KPO_4) and 80 mM Tris-HCl buffer, both pH 7.6, and four different NaCl conditions (0, 0.1, 0.5, 1.0 M) were examined. Dependent on the native thermal stability of the tested proteins, samples were heated with a heating gradient of 1 K min^{-1} in a temperature range of 20 – 85 °C, 20 – 80 °C and 20 – 95 °C for BSA, amylase and streptavidin, respectively. All experiments were performed in *Prometheus NT.48 Series nanoDSF Grade High Sensitivity Capillaries*.

3.2.2 Cultivation of *Halomonas elongata* ΔectC

Halomonas elongata ΔectC cultivation was performed in MM63 medium with 0.5 M and 1.0 M NaCl as well as in two different bioreactors, namely the *Biostat® B plus* 2 L reactor by Sartorius and the 50 L reactor *LP75* from Bioengineering.

Initially, a single *H. elongata* ΔectC colony, picked from a 1 M LB plate (Table 3.4), was cultivated in 1 M LB medium (Table 3.5) at 30 °C overnight (preculture I). To adapt to later cultivation conditions, preculture I was inoculated 1:100 in shaking flask with MM63 medium (Table 3.6) without trace element solution (TE) and incubated overnight at 30 °C (preculture II).

Table 3.4: LB Medium with 1 M NaCl for plating.

Component	Concentration
Tryptone	10 g L^{-1}
Yeast extract	5 g L^{-1}
NaCl	1 M
Agar	15 g L^{-1}

Table 3.5: LB Medium with 1 M NaCl.

Component	Concentration
Tryptone	10 g L^{-1}
Yeast extract	5 g L^{-1}
NaCl	1 M

For the MM63 medium a combined 4x stock solution of the salt components (KH_2PO_4, KOH, $(NH_4)_2SO_4$, NaCl) and separate stock solutions for glucose, $MgSO_4$ and $FeSO_4$ were prepared according to Table 3.6. Salt component stock, glucose stock and $MgSO_4$ stock were autoclaved, whereas $FeSO_4$ and TE were steril filtered to avoid precipitation of the components. The TE was prepared according to Table 3.7, following the order of named ingredients to avoid complexation of the components. Finale MM63 medium ingredient concentrations are reached by mixing the stock solutions and fill up to the required volume with sterile ddH_2O.

Table 3.6: MM63 minimal medium.

Component	Concentration	Stock concentration
KH_2PO_4	100 mM	400 mM
KOH	75 mM	300 mM
$(NH_4)_2SO_4$	60 mM	240 mM
NaCl	0.5 - 1 M	2 - 4 M
$C_6H_{12}O_6$	15 g L^{-1}	300 g L^{-1}
$MgSO_4$	1 mM	1 M
$FeSO_4$	12 μM	variable
Trace element solution	3 mL L^{-1}	

The next day, preculture II was centrifuged at room temperature (*RT*) for 20 min and 3200 *g*. The cell pellet was resuspended in fresh MM63 medium (Table 3.6) to reach an OD of 15 and 25 for 1.5 L and 50 L cultivation, respectively. Thus, inoculation volume to reach a similar start OD of 0.1 was 10 mL and 200 mL for 1.5 L and 50 L batch cultivation, respectively. The conditions for the main cultivation of *H. elongata* ΔectC in a 1.5 L and a 50 L reactor system are presented in Table 3.8.

During cultivation, samples from cultivation broth were take periodically over the whole process time. OD_{600} was measured with the *BioSpectrometer basic* from Eppendorf against

Table 3.7: Trace element solution; pH 7 to adjust

Component	Concentration	Weight in
$MnSO_4 \cdot H_2O$	3 mM	0.4532 g
$ZnSO_4 \cdot 7\,H_2O$	1 mM	0.1818 g
$CoCl_2 \cdot 6\,H_2O$	1 mM	0.1864 g
$CuSO_4 \cdot 5\,H_2O$	40 μM	0.1030 g
$KAI(SO_4)_2 \cdot 12\,H_2O$	4 μM	0.0204 g
BH_3O_3	162 μM	0.0110 g
$NiCl_2 \cdot 6\,H_2O$	105 μM	0.0273 g
EDTA	5 mM	1.5008 g

Table 3.8: Cultivation conditions *Halomonas elongata* ΔectC.

	Set value	Control
Temperature	30 °C	controlled
pH	7	controlled
Pressure	1 atm	
Stirring speed	> 300	controlled
Aeration	1.25 vvm	
Oxygen saturation	30%	controlled
Medium	MM63	

MM63 medium at 600 nm in 10 mm cuvettes. Further, γ-NADA concentration was analyzed. Here, cultivation broth was centrifuged for 10 min at 17000 *g*. Supernatant was discarded after centrifugation. The cell pellet was resuspended in ddH_2O and frozen up at least overnight. After thawing, γ-NADA was excreted via freeze-thaw mechanism [118] and the γ-NADA enriched supernatant was analysed in HPLC (see subsection 3.2.6).

When provided glucose was exhausted (indicated by sudden pO_2 rise), the cultivation was stopped and cells were harvested. Cultivation broth from 1.5 L reactor were centrifuged for 15 min and 3260 *g*. Supernatant was discarded and the remaining cell pellet was resuspended in ddH_2O to receive an approximated OD_{600} of 25. Then, cells were frozen and stored at -20 °C. Cells from the 50 L reactor were harvested and separated with the help of a disk separator. Here, cultivation volume was recycled from the reactor to the separator and back

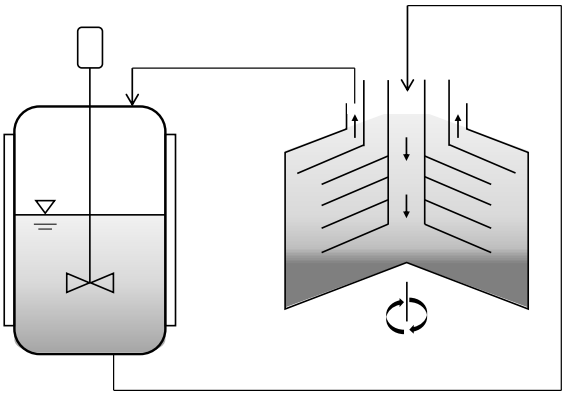

Figure 3.1: Recycling setup for the cell harvesting and cell concentration after cultivation of *H. elongata* ΔectC in the 50 L reactor.

to concentrate the cells as much as possible (see Figure 3.1). For filling the separator, a volume flow of 250 L h^{-1} was used until a first ejection of the cells. After, flow was set to 150 L h^{-1} with a filling time of 15 min and an ejection time of 160 ms. Moreover back-pressure was et to 3.7 bar. When OD_{600} in the reactor was less than 0.5, the separation was stopped and harvested cell volume was filled up to 20 L with ddH_2O and further frozen and stored at -20 °C.

3.2.3 Determination of the ash free dry weight from *Halomonas elongata* ΔectC

The high salinity in the cultivation medium of *H. elongata* ΔectC limits standard biomass quantification. Thus, thermal gravimetric analysis (TGA) was performed to accurately distinguish between water, biomass and ash content in the sample. Thus, in following the biomass of *H. elongata* from cultivation is given as ash free dry weight (*AFDW*).

During a cultivation in 1.5 L scale with 1 M NaCl and 15 g L^{-1} glucose, up to 40 mL samples were taken at different OD_{600} levels and centrifuged with 4000 *g* for 20 min at room temperature (*RT*). The supernatant was discarded, however OD_{600} was previously analyzed for correcting the OD-*AFDW* correlation according to Equation 3.1.

$$OD_{600} = OD_{600,cultivation} - OD_{600,supernatant} \quad [-] \quad (3.1)$$

Remaining cell pellet was resuspended in 1 mL of 1.4 M NaCl, transferred to a reaction tube and again centrifuged for 5 min at 14000 *g* at *RT*. Supernatant was discarded. The resuspension step was repeated and the dissolved cells were transferred to be previously weighted reaction tube, centrifuged and the pellet was frozen at -80 °C for subsequent lyophillization (*Alpha 1-2 LDplus, Martin Christ Gefriertrocknungsanlagen GmbH, Osterode am Harz, Germany*).

Freeze-dried samples in a range of 5 - 17 mg were analyzed in TGA (*TGA/DSC 3+, METTLER TOLEDO, Columbus, United States*), using 50 μL aluminum oxide pans (*THEPRO GbR, Heinsberg, Germany*). After 10 min equilibration of the system at 30 °C samples were heated with 10 K min^{-1} up o 1050 °C in a synthetic air stream of 20 L h^{-1}. *AFDW* was finally evaluated from the detected mass loss between 160 °C and the equilibrium state at the end of the measurement (> 1000 °C) and the weight of the freeze-dried sample.

3.2.4 Filtration

For the implementation of a filtration cascade in the downstream process for γ-NADA, first a screening of five microfiltration (*MF*), three ultrafiltration (*UF*) and seven nanofiltration (*NF*) *flat-sheet* membranes from different suppliers was performed (compare Table 3.9). The filtration was operated in *cross-flow* mode (see Figure 2.5b in subsection 2.3.1) with a *Cube80-VA* system from *SIMA-tec*. Figure 3.2 shows the corresponding piping and instrumentation diagram (*PID*).

The feed flow rate is adjusted manually based on the power of the pump and is recorded downstream of the membrane cell on the concentrate side (FI/FIR01). The pressure before (PIR01) and after (PIR02) the membrane is measured and, based on the pressure difference, the transmembrane pressure (*TMP*) (Equation 3.4) is calculated and indicated by the instrument. *TMP* can be adjusted with the manual valve, placed before the flow rate sensors (FIR/FI01). Further, the permeate flux (FIR02) (Equation 2.9), the conductivity of the permeate (QIR01) and the temperature at the membrane (TIR01) are recorded. The temperature can be controlled with an external chiller, connected to the heat exchanger.

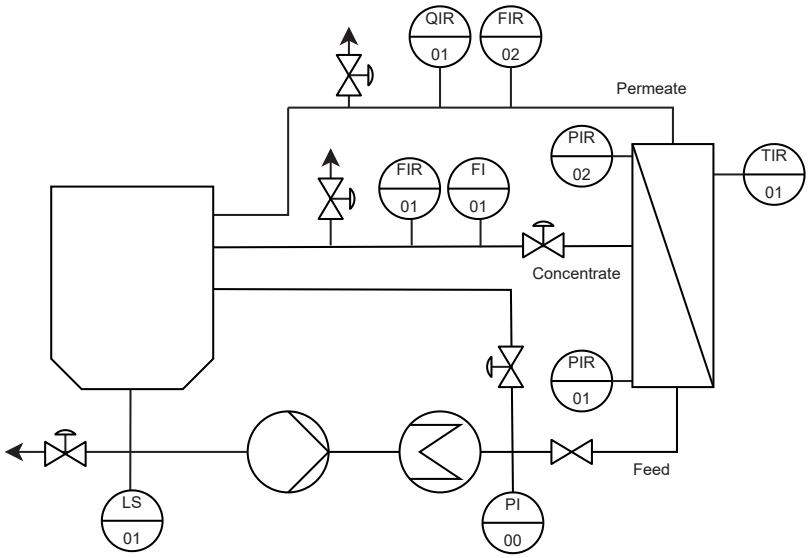

Figure 3.2: *PID* of the cross-flow filtration system *Cube80-VA* from *SIMA-tec*. Pressure (PI/PIR), temperature (TIR), conductivity (QIR) and the flow rate (FI/FIR) are recorded and if the level in the feed tank falls below the minimum level (LS) a safety-switch off for the pump is initiated. *Flat-sheet* membranes are installed in the filtration membrane cell. Adapted from information of supplier [119].

Membrane preparation and membrane resistance determination

Membranes listed in Table 3.9 were either purchased from the manufacturer or were kindly provided from the *Department of Soft Matter Science and Dairy Technology (150e)* at the University of Hohenheim.

Before using the *flat-sheet* membranes they were conditioned with the workflow shown in Figure 3.3. The hydration step is performed in a water bath, whereas conditioning, compacting and cleaning are performed with the membrane inserted in the *Cube80-VA* filtration plant. According to the information of the supplier of the system, the membrane is placed in the membrane cell facing the *PTFE* spacer and reticular spacer with its' active side. The cross-striped and longitudinal-striped collecting plates for the permeate are placed on top in that order. The conditioning, compacting and cleaning of the membranes is performed with applied pressure (see Figure 3.3). Cleaned membranes were stored in 2 % glycerol at 4 °C. Thus reused membranes where washed with ddH_2O until conductivity in the concentrate was lower 10 µS cm^{-1}.

Before and after the filtration process and after the cleaning protocol the membrane (R_m) and the fouling (R_f) resistance were calculated with Equation 3.2 and Equation 3.3, respectively.

Table 3.9: Filtration membranes.

Membrane type	Supplier	Name	Material	Cut-off
Microfiltration	Synder	FR	PVDF	850 kDa
	Nadir	MP005	PES	0.05 µm
	Pall	Supor 200	PES	0.2 µm
	Synder	V0.2	PVDF	0.2 µm
	Pall	Supor 450	PES	0.45 µm
Ultrafiltration	Synder	ST	PES	10 kDa
	Synder	MQ	PES	50 kDa
	Synder	LY	PES	100 kDa
Nanofiltration	Desal/GE	DK	Propietary	150 - 300 Da
	Desal/GE	DL	Propiertary	150 - 300 Da
	Nitto	Dairy NF	Composite polyamid	150 - 250 Da
	DOW	NF	Polyamid	200 - 400 Da
	DOW	NF270	Polyamid	200 - 400 Da
	Synder	NFW	Polyamid	300 - 500 Da
	Trisep	XN45	Piperazine	300 - 500 Da

Inlet pressure p_1 was set to the values listed in Table 3.10 and the feed flowrate Q_f was set to 10 L h^{-1}. Outlet pressure p_2 and permeate flowrate Q_P were noted from online recording or analog measurements. Here, a kinematic viscosity ν of $0.893 \cdot 10^{-6}$ m^2 s^{-1}, $0.724 \cdot 10^{-6}$ m^2 s^{-1} and $0.602 \cdot 10^{-6}$ m^2 s^{-1} for 25 °C, 35 °C, and 45 °C at 0.1 MPa is assumed, respectively.

Table 3.10: Initial pressure p_1 for the calculation of membrane (R_f) and fouling (R_m) resistance determination.

Membrane type	Inlet pressure p_1					
	1	**2**	**3**	**4**	**5**	**6**
Microfiltration	0.2 bar	0.4 bar	0.6 bar	0.8 bar	1.0 bar	1.2 bar
Ultrafiltration	2 bar	3 bar	3.5 bar	4 bar	7 bar	
Nanofiltration	3 bar	3.5 bar	4 bar	5 bar	8 bar	10 bar

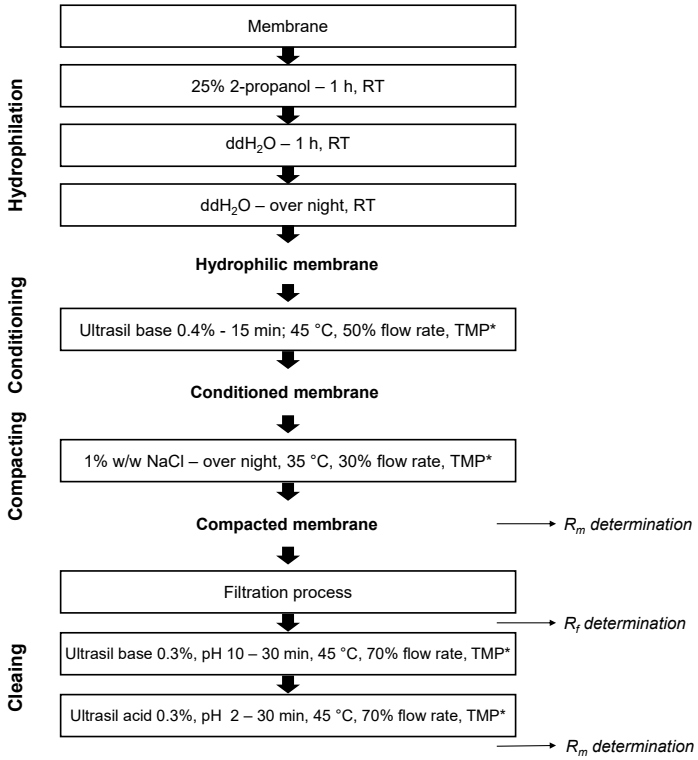

Figure 3.3: Preparation protocol of *flat-sheet* membranes. Applied pressure (TMP*) for *MF* membranes: conditioning 2 bar, compacting 2 bar, cleaning 2 bar; *UF* membranes: conditioning 2 bar, compacting 8 bar, cleaning 5 bar; *NF* membranes: conditioning 20 bar, compacting 40 bar, cleaning 25 bar.

$$R_m = \frac{\Delta p_{TM} \cdot A}{32 \cdot \nu \cdot Q_P} \quad [\mathrm{m}^{-1}] \quad (3.2)$$

$$R_f = \frac{\Delta p_{TM} \cdot A}{32 \cdot \nu \cdot Q_P} - R_m \quad [\mathrm{m}^{-1}] \quad (3.3)$$

$$\Delta p_{TM} = \frac{p_1 + p_2}{2} \quad [\mathrm{bar}] \quad (3.4)$$

$$Recovery = 1 - \frac{R_{m,after}}{R_{m,before}} \quad [\text{-}] \quad (3.5)$$

The obtained recovery (see Equation 3.5) clarifies the cleaning efficiency and reusability of the membrane. The closer the recovery remains to 1, the more successful is the cleaning protocol.

Membrane screening

The membrane screening was performed with all *flat-sheet* membranes of different filtration types listed in Table 3.9. The related screening transmembrane pressure (Δp_{TM}) and feed flowrate (Q_F) conditions are shown in Table 3.11. According to Hartinger *et al.* [120], filtration performance is not affected when Δp_{TM} is altered in ascending order. Thus, for each membrane, screening experiments were performed in a row, starting with the lower Δp_{TM} value at 10 and 60 L h^{-1} and subsequently running the experiments at the higher Δp_{TM} with both Q_F conditions. Thawed fermentation broth of the 50 L cultivation (subsection 3.2.2) was directly used as feed solution in the *MF* membrane screening, whereas for *UF* and *NF* screening the fermentation suspension has been initially ultracentrifuged after thawing. Here, cells were centrifuged at 21000 *g* for 45 min at 4 °C (*Beckman LE-70 Optima, rotor 70-Ti, Beckman Coulter, Krefeld, Germany*) and remaining supernatant was used as feed in *UF* and *NF* screening. The screening experiments were performed in steady state experiments at 35 °C.

Table 3.11: Membrane screening conditions for microfiltration (*MF*), ultrafiltration (*UF*) and nanofiltration (*NF*) at 35°C.

		Transmembrane pressure Δp_{TM}				
		2 bar	3 bar	8 bar	10 bar	40 bar
Feed flowrate Q_F	10 L h^{-1}	*MF*	*MF*	-	-	-
	60 L h^{-1}	*MF*	*MF*	-	-	-
	10 L h^{-1}		*UF*	*UF*	-	-
	60 L h^{-1}	-	*UF*	*UF*	-	-
	10 L h^{-1}	-	-	-	*NF*	*NF*
	60 L h^{-1}	-	-	-	*NF*	*NF*

Therefor, *cross-flow* filtration was run in recycling mode, meaning that permeat and concentrate were pumped back into the feed tank. An initial feed sample was taken in duplicates and after 20 min a steady state equilibrium at the membrane was assumed. Duplicate samples of the permeat were taken. Accordingly, filtration conditions were adapted to the next step and the experiment was repeated without changing the feed. Finally a duplicated feed sample was taken and the membrane was washed and stored.

Concentration of γ-NADA, proteins and NaCl were analyzed in the feed ($c_{i,F}$) and in the permeate ($c_{i,P}$) samples (see subsection 3.2.6). The membrane ranking based on the permeation P_i (Equation 2.7) and rejection R_i (Equation 2.8) performance of the membranes for the respective ingredient *i*. For each filtration step (*MF*, *UF*, *NF*) the best performing membrane was chosen based on the *weighted sum method for multi-objective optimization* described by Zadeh [121] and subsequently used for optimization and whole process performance.

Optimization

The optimization of the nanofiltrations' process parameters temperature T and pressure Δp_{TM} was performed at a constant flow rate Q_F of 10 L h^{-1} and with the *Desal/GE DL* membrane exclusively. T and Δp_{TM} were varied from 25 to 45°C and 5 to 40 bar, respectively, while the respective other was kept constant. Here, the recycling mode, already described above was applied for the experimental setup.

Filtration cascade

On the basis of the membrane screening and the parameter optimization the cascade process was designed with the parameter conditions shown in Table 3.12.

Table 3.12: Membranes and conditions for the filtration cascade process according to the screening and optimization results described in section 3.2.4 Membrane screening and section 3.2.4 Optimization.

Membrane type	**Membrane**	**Feed flowrate** $\boldsymbol{Q_F}$	**Transmembrane pressure** $\Delta \mathbf{p}_{TM}$	**Temperature** T
Microfiltration	Synder V0.2	10 L h^{-1}	3 bar	45 °C
Ultrafiltration	Synder MQ50	10 L h^{-1}	2 bar	35 °C
Nanofiltration	Desal DL	10 L h^{-1}	10 bar	35 °C

The filtration steps *MF*, *UF* and *NF* were performed successively. In the beginning, permeat and concentrate were recirculated in the feed tank until the desired temperature (see Table 3.12) was reached. The final permeat was collected on ice in *MF* and *UF* and further used as feed for the next downstream filtration step. Finally, the concentrate of the *NF* was used for the final crystallization (see subsection 3.2.5). Over the process time, permeat samples were periodically taken and analyzed to have an insight on the ongoing process. After each

filtration step, volumes of concentrate and permeate were measured and duplicate samples were taken from the initial feed as well as from the remaining permeat and concentrate.

$$Y = \frac{m_{NADA}}{m_{Feed}} \quad [\%] \quad (3.6)$$

$$VCF = \frac{V_{before}}{V_{after}} \quad [\text{-}] \quad (3.7)$$

$$CF_i = \frac{c_{after}}{c_{before}} \quad [\text{-}] \quad (3.8)$$

$$P_{NADA} = \frac{m_{NADA}}{m_{NaCl} + m_{Protein}} \quad [\%] \quad (3.9)$$

The filtration process was valued according to the factors yield Y (Equation 3.6), volume concentration factor VC_f (Equation 3.7), γ-NADA concentration factor CF_{NADA} (Equation 3.8) and γ-NADA purity P_{NADA} (Equation 3.9).

3.2.5 Crystallization

Solubility of γ-NADA in various solvents

The solubility of γ–NADA in various solvents, typical for the crystallization of small molecules [122], was tested. First, the *conductor-like screening model for realistic solvents* method (*COSMO RS*) was used to estimate the solubility of γ–NADA and to narrow down the list of potential solvents for the crystallization. Subsequently, the real solubility experiments were carried out with a selection of solvents, according to the simulations.

Simulation of the solubility with COSMO-RS

For the simulation of the solubility of γ–NADA following *COSMO-RS* based tools were used: *TURBOMOLE*, *Tmolex*, and *COSMOtherm*. All simulations were conducted by Dr. Ljubomir Grozdev according to the methodology described for terpenes in Grozdev [123].
The chemical structure of γ–NADA was translated into a primary 3D structure through a *simplified molecular-input line-entry system* (*SMILES*) code. The *GEO-OPT-quick* option in *Tmolex* was further used for geometrical optimization of the 3D structure. Based on this structure, *COSMO-RS* specific parameters (*COSMO-BP-TZVP-FINE* parameterization)

were calculated, resulting in the σ-surface and chemical potential of γ–NADA, which were further implemented in the *COMSOtherm* database. The relative solubility of γ–NADA was simulated in *COSMOtherm* for the following solvents: acetic acid, acetonitrile, benzene, 1-butanol, chloroform, cyclohexane, cyclohexanol, diethylether, *DMF*, *DMSO*, ethylacetate, glycerol, ethanol, hexane, 1-hexanol, methanol, 1-octanol, propanol, propanone, toluene, water. Here, γ–NADA was considered in a solid state for all tested temperatures (0, 5, 20, 25, 30, 50, 80°C) which required an additional simulation of ΔG. After a primary simulation with a non-iterative calculation, the iterative simulation was done with a considered equilibrium for γ–NADA in each solvent at each temperature, resulting in absolute solubility values.
Same was done for the solubility calculations of γ–NADA in different solvent-water mixtures at 25°C. The ratio of water to solvent was tested in 10% increments in a range from 0-100% for acetonitrile, ethanol, methanol, and propanol.

Experimental validation of the solubility of γ–NADA

Based on the findings of the simulation described above, the solubility of γ-NADA was tested in acetic acid, ethanol, methanol, water, and 1 M NaCl dependent on the temperature. Here, the the hydrolyzed bitop sample, containing ectoine, γ-NADA, α-NADA and NaCl (exact composition shown in Table 3.13), was dissolved at the respective temperature to maximum saturation.

Table 3.13: Composition of the hydrolyzed bitop sample (hydrolyzed ectoine material) kindly provided by bitop AG. Material was dissolved in ddH_2O to maximum saturation at 50 °C. Amino acid concentration was quantified in *HPLC*, NaCl amount was quantified with *ICP-MS* (see subsection 3.2.6).

	Ectoine	**γ–NADA**	**α–NADA**	**NaCl**
w/w [%]	2.6±0.2	17.5±4.5	49.2±2.5	30.8±1.1

Samples were taken after the equilibration time of 24 h, centrifuged at the required temperature at 17000 *g* and the supernatant was analyzed in *HPLC* (see subsection 3.2.6) to determine the dissolved γ-NADA concentration. Solubility determination of γ-NADA in ethanol (*EtOH*), methanol (*MeOH*) and 2-propanol (*IPA*) fractions was performed from 0 - 100 % solvent concentration in 10 % increments. Here, purified γ-NADA crystals from cooling crystallization (see description below) were dissolved to maximum saturation overnight at room temperature and 1500 rpm stirring. Further, samples were analyzed as described above.

Cooling crystallization

For the ideal cooling crystallization experiments, the hydrolyzed bitop sample (see Table 3.13) was dissolved overnight in H_2O at 50 °C and 1000 rpm shaking or stirring to saturation. Then, supernatant was sterile filtered to avoid secondary nucleation and the saturated solution was cooled down to 20 °C overnight and 300 rpm stirring. Obtained crystals were separated from supernatant, subsequently dried and analyzed in *HPLC* (see subsection 3.2.6) by dissolving in H_2O.

The method for the cooling crystallization was adapted to crystallize γ-NADA in a 500 mL reactor system (*OptiMax 1001 Synthesis workstation, Mettler Toledo Inc*), kindly supported by Dr. Simon Schiele at the *Chair of process systems engineering, TUM*. For the evaluation of the effect of the cooling rates on the crystallization, a saturated solution of hydrolyzed bitop material (see Table 3.13) was cooled down from 50°C to 20°C with different cooling rates (0.1 K min^{-1}, 1.0 K min^{-1}, 10 K min^{-1} at a constant impeller speed of 300 rpm. The effect of variations in the impeller speed was examined at a constant cooling rate of 10 K min^{-1}. The progress of the crystallization was visualized with inline microscope pictures (*particle vision and measurement, PVM; Mettler Toledo Inc.*).

Antisolvent crystallization at ideal conditions

For the ideal antisolvent crystallization experiments in defined conditions, pre-purified γ-NADA from cooling crystallization was used. Here the hydrolyzed bitop sample (Table 3.13) was dissolve and crystallized as described above and pure γ-NADA crystals were obtained which are used further.

First, the saturation concentration of γ-NADA at room temperature (*RT*) was determined in *EtOH*, *MeOH* and *IPA* and in their respective percentages mixed with H_2O. Here, the whole range between 0 - 100 % antisolvent was examined in 10 % increments. Pure γ-NADA was dissolved in excess in the respective solvent concentration, overnight at *RT* and 1500 rpm shaking. Further, samples were centrifuged at 17000 *g* and supernatant concentration was analyzed in *HPLC* (subsection 3.2.6). Supersaturation, when batch-wise adding solvent to reach a given concentration, was determined as follows: γ-NADA was dissolved to maximum concentration overnight at *RT* and 1000 rpm stirring. Further supernatant was sterile filtered to avoid secondary nucleation. Pure solvent was added in 10 % increments to the solution to step-wise reach necessary solvent concentration. Here, solution was stirred at 350 rpm and samples were taken after 10 min equilibration time at given solvent conditions before

continuing with the next solvent step. They were prepared for *HPLC* analysis as described above. For simplicity, resulting saturation $S_{x,i}$ at the respective solvent percentage was calculated according to Equation 2.13 with the saturated concentration c_i^* from solubility experiments and the supersaturated concentration c_i from batch-wise increase experiments. Saturation and supersaturation conditions are similar, thus activity coefficients γ_i can be neglected (see Equation 2.12). Since solubility data were determined at slightly different solvent percentages compared to the additive experiments, they were fitted with a matlab DS data fit.

Antisolvent crystallization of concentrate from nanofiltration

γ–NADA in nanofiltration (*NF*) concentrate was crystallized as described above, however the step-wise adding of antisolvent was adapted. First, an initial step increasing the *EtOH* fraction to 0.45 was performed. An additional centrifugation step was performed to exclude precipitated proteins and the supernatant was further used in crystallization. Here, the *EtOH* fraction was step-wise (5 % increments) increased to a maximum of 0.85. Each described solvent condition was equilibrated for 10 min. To increase the yield, an additional cooling crystallization was performed over night under same stirring condition and cooling down to 4 °C. Obtained solid material was harvested with centrifugation and subsequently dried.

3.2.6 Analytics

HPLC analysis to quantify Nγ-acetyl-L-2,4-diaminobutyric acid

γ-NADA was analyzed in *HPLC* (*Infinity II* from Agilent Technologies) with a reversed phase setup. Here, a *YMC-Pack Polyamine II; 12nm, S-5 µm, 250 x 4.6 mm ID* with the fitting pre-column from YMC was used. The method parameter are listed in Table 3.14.

Samples were diluted with deionized water to fit into the standard concentration range of 0.05 - 0.5 g L^{-1} and subsequently steril filtered. Samples from antisolvent crystallization (see subsection 4.4.3) were previously lyophillized (*Alpha 1-2 LDplus, Martin Christ Gefriertrocknungsanlagen GmbH, Osterode am Harz, Germany*) and resuspended in deionized water to avoid disturbing effects in analysis due to the solvent content.

Table 3.14: *HPLC* method defintion.

Column	YMC-Pack Polyamine II; 12nm, S-5 μm, 250 x 4.6 mm ID
Flow rate	1 mL min^{-1}
Temperature	30 °C
Buffer composition	65/35 acetonitrile/water
Injection volume	20 μL
Detection	198 nm, 210 nm, 280 nm
Standard concentration range	0.05 - 0.5 g L^{-1}

Bicinchoninic acid (*BCA*) assay to calculated quantity of protein content

To analyze the impurity amount resulting from proteins in the process, a *BCA* assay was performed with the help of the *Pierce™ BCA Protein Assay Kit*, following the *microplate procedure (sample to WR ratio = 1:8)* instruction of the manual [124]. Samples were diluted in deionized water to fit into the standard concentration range of the standard protein BSA (0.025 - 2.0 g L^{-1}) which was included in the kit. Absorbance of the obtained complex was measured at 562 nm with the plate reader *Infinite M200* from Tecan.

Inductively coupled plasma mass spectrometry (*ICP-MS*) and AgCl precipitation to calculate NaCl concentration

Samples for *ICP-MS* analysis were directly dissolved or diluted in 3 % HNO_3 to avoid oxidation. The maximum tolerated NaCl concentration was 0.1 g L^{-1} and a volume of 10 mL was required. Samples were kindly analyzed by Magdalene Spicher at the *Fraunhofer Institute for Process Engineering and Packaging IVV* in Freising, Germany.

For the second method to quantify the NaCl content in the sample, silver nitrate precipitation was performed. Here, chloride is precipitated with the help of silver nitrate ($AgNO_3$) to silver chloride (AgCl). First, reaction tubes were dried over night at 60 °C and weight afterwards. One part of standard solution of NaCl (0.01 M - 1.0 M) was mixed with 10 parts of 0.1 M $AgNO_3$ solution. Samples were prepared the same way as NaCl standard, however more than

one part is possible when the multiplication factor is taken into account in the evaluation. Occurring AgCl precipitate is centrifuged at 17000 g for 5 min and supernatant is discarded.

$$m_{AgCl} = m_{Tube+AgCl} - m_{Tube} \quad [\text{g}] \quad (3.10)$$

Remaining solid is dried over night at 60 °C and subsequent the reaction tubes are weighted a second time. The mass of AgCl precipitate m_{AgCl} is calculated from the difference of the weighted reaction tube with precipitate $m_{Tube+AgCl}$ and the sole mass of the reaction tube m_{Tube} (see Equation 3.10). Chloride content was assumed to be similar to NaCl content.

4 Results and Discussion

4.1 Characterization of Nγ-acetyl-L-2,4-diaminobutyric acid

As more detailed described in section 2.1 and subsection 2.1.2, the compatible solute Nγ-acetyl-L-2,4-diaminobutyric acid (γ-NADA) is known mainly for being the precursor molecule of ectoine, one of the most established compatible solutes on the market. Ectoine and its potential is well described (for example reviewed in Pastor *et al.* [125]), yet little is known about the potential and characteristics of γ-NADA. The molecule was described for the first time in Liss [39], isolated from latex of *Eupborbia pulcherrimu.* Here, also a crystallization in propanol to needle-shaped morphology was explained. Years later, Cánovas *et al.* [41] showed that a *Halomonas elongata* strain is able to grow in saline environment, although lacking of ectoine synthase and thus accumulating γ-NADA as final compatible solute (see Figure 2.1). In Cánovas *et al.* [42], the potential of purified γ-NADA to stabilize enzymes in vitro, here rabbit muscle lactate dehydrogenase, was demonstrated. To fill this knowledge gap about the molecule itself and to demonstrate the potential, the characterization of γ-NADA is shown and discussed in the following sections.

4.1.1 Crystal structure and spectroscopic analysis of γ–NADA

The crystallization of γ–NADA from model solutions and from biotechnological production in *Halomonas elongata* ΔectC is described and discussed later in section 4.4. Here, the crystal structure determination of γ–NADA and the spectroscopic analysis is discussed, already published in Martin *et al.* [100].

The resulting crystal structure of the single γ–NADA molecule is shown in Figure 4.1. The deprotonated form of the oxygen atoms of the carboxylic acid groups and the third hydrogen atom at the amine group (N1) demonstrate the zwitterionic character of γ–NADA, very typical for amino acids and their derivatives. Detail length and angles of the respective bonds are given in Martin *et al.* [100].

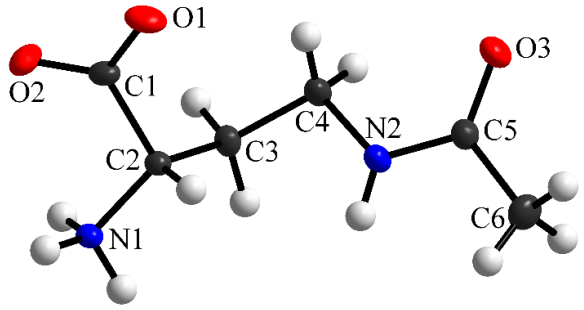

Figure 4.1: Structure determination of single γ–NADA molecule. Atoms are assigned as followed: carbon (C) as black, hydrogen (H) as white, oxygen (O) as red, and nitrogen (N) as blue. Adapted from [100].

The two- and three–dimensional connections of the γ–NADA molecules in the crystal by short and linear hydrogen bonds (H–bonds) are shown in Figure A.2. Here, the NH^{3+}···O bonds and N2–H2B···O3 form the 2D plane which is connected via N1–H1A···O1 bonds to a 3D structure. The molecule crystallizes in chiral orthorhombic space group $P2_12_12_1$.

The spectroscopic analysis of the obtained γ–NADA crystals is shown in Figure 4.2. Here, peaks and bands at specific wave numbers indicate the presence of respective bonds and atomic structures. In the characteristic 'fingerprint region' (400 - 1700 cm^{-1}) of the amino acid derivative, two peaks are very pronounced in Raman (Figure 4.2a) - 1296 cm^{-1} and 910 cm^{-1}. In IR in Figure 4.2b the peaks are generally more clustered, here a broad spectra with several peaks between 1700 an 1300 cm^{-1} stands out. As can be seen in Figure 4.1, the amino acid derivative γ–NADA has three characteristic groups - the typical carboxyl ($COOH/COO^{\breve{}}$) and amino (NH_2/NH_3^+) group and an additional amide group (O=C–NH–C) in the side chain. The most pronounced band in the "fingerprint region" (400–1700 cm^{-1}) [126] at 1537 cm^{-1} in IR represents the symmetric bending of the amino group $\delta(NH_3^+)$ [127], while signals for amide II stretching of C–N ν(C–N) and planar bending of N-H (δ(N-H)) are visible in the range of 1480-1580 cm^{-1} [128, 129]. N-H stretching (ν(NH)) in O=C–NH–C secondary amide [130] is represented slightly shifted in the bands at 3257 cm^{-1} and 3250 cm^{-1} for Raman and IR, respectively. Symmetric $\nu(COO^{\breve{}})$ and asymmetric stretching $\nu_{as}(COO^{\breve{}})$ of the carboxylic group of the amino acid is visible at a wave number of 1419/1411 cm^{-1} (Raman/IR) and 1588 cm^{-1}, respectively. A very detail assignment is shown in Martin *et al.* [100], yet the here discussed vibration bands proof and characterize the solids as γ–NADA and fit well to the described findings in crystal structure. Showing the zwitterionic character fits well in the properties of compatible solute [10, 131] and underline it's potential function as osmolyte in halophilic organism. In the following subsection 4.1.2, this potential is further demonstrated with thermal stability studies of three different proteins.

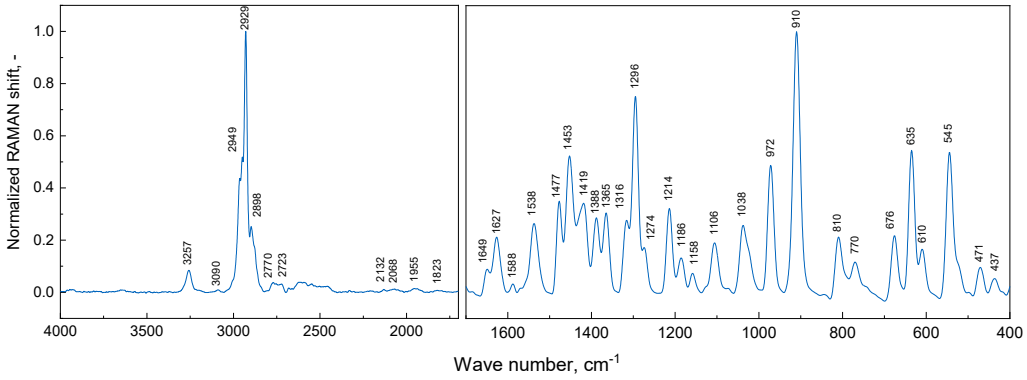

(a) Raman shift of γ–NADA crystals.

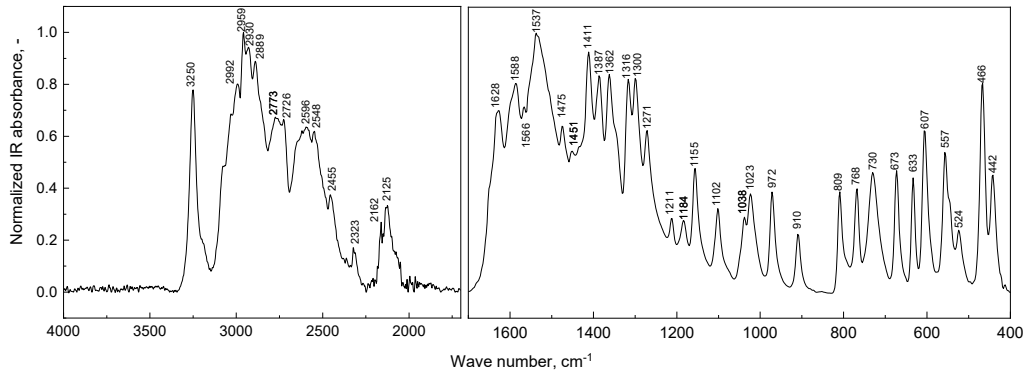

(b) IR bands of γ–NADA crystals.

Figure 4.2: Spectroscopic analysis of γ–NADA crystals with Raman (a) and IR (b) spectroscopy. Peaks are normalized to the respective highest peak in the wavenumber range of 4000 - 1700 cm^{-1} and 1700 - 400 cm^{-1}. Adapted from [100].

4.1.2 Thermal protein stabilization with γ–NADA and comparable compatible solutes

As already described above, the ability of γ–NADA to act as compatible solute in the organism and to stabilize isolated enzymes was shown by Cánovas *et al.* [41], García-Estepa *et al.* [27] and Cánovas *et al.* [42], respectively. However, the stabilization of proteins with the help of compatible solutes is mostly dependent on the solute-protein combination [132, 133]. Therefore, no too precise statement can be made on the basis of one example. Thus, the thermal stabilization potential of γ–NADA was demonstrated with three very different proteins, namely BSA, amylase and streptavidin, in four NaCl conditions and in comparison to their native stability and with established solutes as ectoine, hydroxyectoine and trehalose.

Further, with performing the stability studies with *nanoDSF*, the examination was extended to non-enzymatic proteins, like BSA and streptavidin.

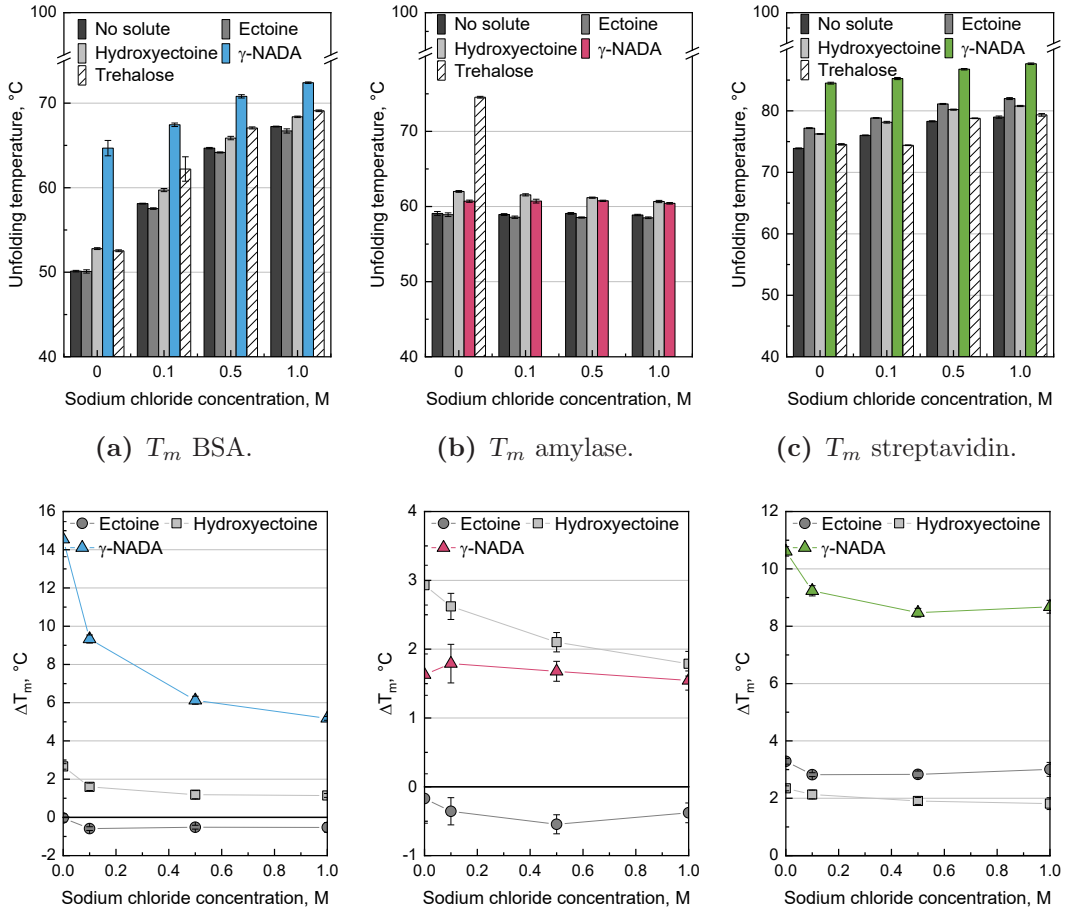

(a) T_m BSA. **(b)** T_m amylase. **(c)** T_m streptavidin.

(d) ΔT_m BSA. **(e)** ΔT_m amylase. **(f)** ΔT_m streptavidin.

Figure 4.3: Unfolding temperature T_m (a-c) and ΔT_m (d-f) of 0.5 g L^{-1} BSA (a,d), amylase (b,e) and streptavidin (c,f) with and without 0.5 M compatible solutes ectoine, hydroxyectoine, γ–NADA and trehalose at 0, 0.1, 0.5 and 1.0 M sodium chloride in 10 mM potassium phosphate buffer pH 7.6.

Figure 4.3a, Figure 4.3b and Figure 4.3c show the unfolding temperature of BSA, amylase and streptavidin, respectively, with the respective compatible solutes added and in different NaCl conditions. Figure 4.3d, Figure 4.3e and Figure 4.3f show the related temperature difference (ΔT_m, defined in Equation 4.1) dependent on the NaCl concentration.

$$\Delta T_m = T_{m;w/\ solute} - T_{m;w/o\ solute} \quad [°C] \quad (4.1)$$

Comparing the native protein stability of the proteins, streptavidin is the most thermal stable one (Figure 4.3c), yet with increasing NaCl concentration BSA catches up (Figure 4.3a). Both proteins are best stabilized with γ–NADA, however, the effect of the other compatible solutes differ. While ectoine stabilizes streptavidin second best, it is least for BSA and vice versa. Amylase, shown in Figure 4.3b, behaves completely different - trehalose is by far the best stabilizing compatible solute, the effect of hydroxyectoine and γ–NADA is very little and ectoine even destabilizes the protein. Further, NaCl does not have any effect on the native protein stability. ΔT_m in Equation 4.1 subtracts the effect of NaCl in the different saline conditions, to clarify the effect of the solutes itself (Figure 4.3d, Figure 4.3e and Figure 4.3f). Regardless of the protein, with increasing NaCl the effect of the solutes is reduced, especially pronounced for γ–NADA. As shown in Figure A.3, the percentage stabilizing effect of γ–NADA stands out for BSA and streptavidin, yet shows the steepest decline with increasing NaCl concentration. Nevertheless, also in high saline environment, γ–NADA performs best for the two proteins. As the native stability of amylase was already least affected by NaCl, also the effectiveness of the solutes is least modified. The obtained native protein stability of the respective proteins fit well with published data [134–138]. Also the effect of NaCl in the respective protein stability is already reported for BSA [138–140] and amylase [137]; for streptavidin, to our knowledge, no NaCl effect is reported yet. NaCl in solution changes the repulsion effects between the medium and the protein and thus support a more compact folding of the protein [138], meaning a better stability. The stabilizing effect of the tested solutes and especially ectoine is reported in vivo [41, 141] and for isolated proteins [28, 132, 142, 143] and further reviewed in Pastor *et al.* [125]. As mentioned above, the effect of γ–NADA against thermal treatment was already reported by Cánovas *et al.* [42]. Here, hydroxyectoine showed an even better stabilization. Yet, literature agree, that no clear statement can be made about the effectiveness of the solutes - each protein requires different solutes for best stabilization against stress [132, 133]. The effect of the compatible solutes like ectoine and hydroxyectoine is mainly described by the preferential exclusion model [19, 23, 144–146]. The same effect is also described for trehalose [147–149], yet low interaction with water is reported [150, 151], which could explain the variations of trehalose as stabilizer for proteins.

In summary, γ–NADA was proofed to be an efficient stabilizer for proteins against thermal stress. In case of BSA and streptavidin, it was even the best of the tested compatible solutes; the effect of γ–NADA on the stability of amylase was yet weak. Beside ectoine, hydroxyectoine and trehalose a bunch of different compatible solutes are on the market. They were not intensively examined here, however to give a comparison and underline the potential of γ–NADA the thermal stability of BSA was also measured for these solutes shown in Figure A.4: Cyclic 2,3-diphosphoglycerate (*cDPG*), diglycerol-phospate (*DGP*), di-myo-inositol-phosphate (*DIP*) and *fiorin*. Even in comparison with these products, γ–NADA was

best to increase the thermal stability. Beside the potential of the γ–NADA monomer, Ahmadi *et al.* [1] recently demonstrated the application of polymerized γ–NADA as drug carrier and dermal delivery system, open up a potential market. Consequently, the development of a potent production and downstream process is the essential step for a future application of γ–NADA. In the following, this step is made and discussed.

4.2 Cultivation of *Halomonas elongata* ΔectC

For the industrial production of Nγ-acetyl-L-2,4-diaminobutyric acid (γ-NADA) the Kunte Group of the Bundesanstalt für Materialforschung und -prüfung (BAM) designed a *Halomonas elongata* mutant (*Halomonas elongata* ΔectC) lacking ectoine synthase ectC (see Figure 2.1) to accumulate γ-NADA, not ectoine, as final metabolic product. As can be seen in Figure 4.4, both, the wildtype and the ΔectC mutant, do not differ in size or shape during growth and production (see Figure 4.4a and Figure 4.4b) and both show the typical elongation in the stationary phase [152] (see Figure 4.4c and Figure 4.4d).

In following batch cultivation experiments the growth behavior and the γ-NADA production of the designed strain were examined. Therefore, the impact of the sodium chloride concentration on the γ-NADA production and growth rate was considered. Additionally, the impact of the reactor size, to test the scalability and robustness of the up-stream process, were evaluated. Here, we compare a sodium chloride concentration in the cultivation media and a working reactor volume of 0.5 M and 1.0 M and 1.5 L and 50 L, respectively.

4.2.1 Correlation of OD_{600} and ash free dry weight for *Halomonas elongata* ΔectC

The measurement of the optical density OD_{600} of a cell culture is the well-established and simple method to map the organisms growth [153, 154]. However, due to the high sodium chloride content in the cultivation process, the ash free dry weight *AFDW* is used to specify the quantity of the biomass of marine organism [155], in particular *Halomonas elongata* [156]. To ensure a greater significance and comparability with the literature, a correlation of the easy and rapid-to-measure OD_{600} and the more precise *AFDW* of *H. elongata* ΔectC was established. Thermal gravimetric analysis (TGA) was performed as described in subsection 3.2.3. The weight loss, when heating the sample, can be accurately assigned to water, biomass and ash content (in this case dominated by NaCl). Thus this method eliminates disturbing sodium chloride variations in the samples, originating from the

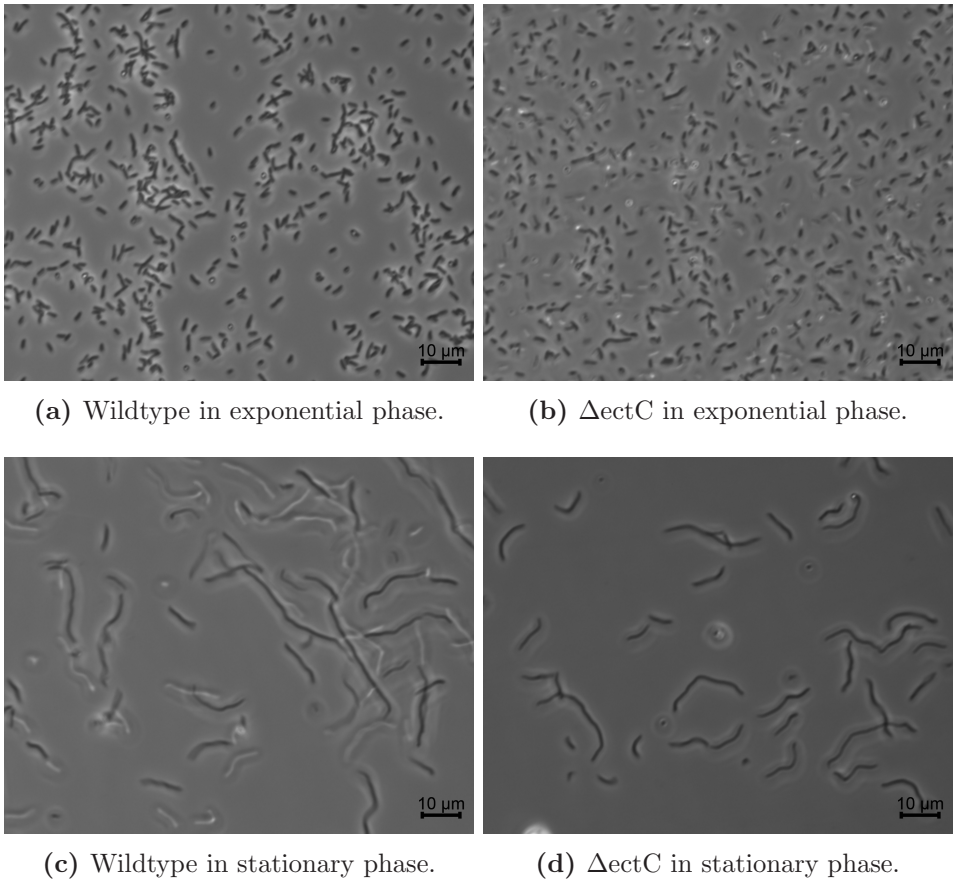

(a) Wildtype in exponential phase. **(b)** ΔectC in exponential phase.

(c) Wildtype in stationary phase. **(d)** ΔectC in stationary phase.

Figure 4.4: *H. elongata* wildtype and *H. elongata* ΔectC in both, exponential and stationary phase grown in LB complex medium with 1 M NaCl (Table 3.5). Microscope pictures were taken in phase-contrast mode, 40x magnification and additional 2.5x optovar magnification (*Axio Observer 7, Carl Zeiss Microscopy Deutschland GmbH, Oberkochen, Germany*)

high salt cultivation conditions. The loss of mass and the related heat flow per sample weight in Figure A.6 gives a vivid image of the step-wise combustion process for the respective components.

Samples were taken from a 1.5 L cultivation with 15 g L^{-1} glucose and 1 M NaCl. This type of cultivation is described in detail later in subsection 4.2.2, however growth behaviour and γ-NADA production of the specific cultivation can be seen in Figure A.5. The received correlation between the optical density OD_{600}, which was measured spectrophotometically

during cultivation in regular intervals, and the *AFDW* is shown in Figure 4.5 and can be calculated from a linear fit given in Equation 4.2.

$$AFDW = 0.2676 \cdot OD_{600} + 0.03088 \quad [\mathrm{g\ L^{-1}}] \quad (4.2)$$

Comparing the obtained correlation in Equation 4.2 with the correlation of *H. elongata* wildtype shown in [156], the remarkably high difference between the correlation factors, meaning the slope of the correlation equations, stands out. OD_{600} measurements do not

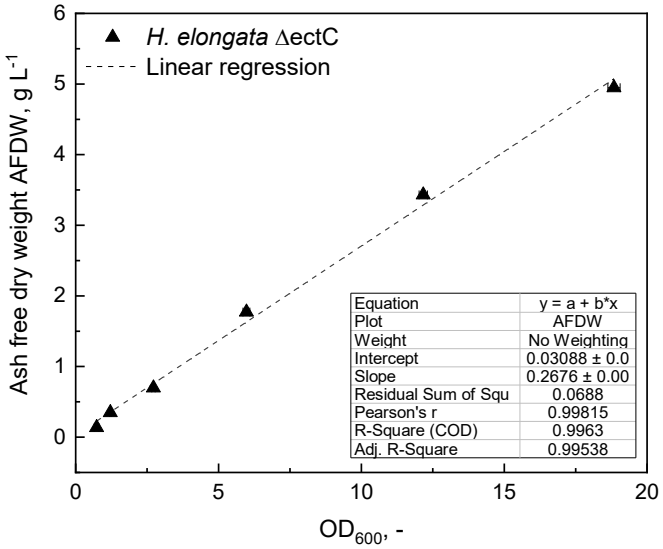

Figure 4.5: Correlation of the optical density OD_{600} and the ash free dry weight *AFDW* of *Halomonas elongata* ΔectC, cultivated in MM63 minimal medium with 1 M NaCl. In the cultivation process, the OD_{600} was measured and the corresponding *AFDW* was calculated from Equation 4.2.

base on absorbance described with the Beer–Lambert law but result from light scattering of the sample. Thus, the organisms shape, size and somehow vitality (living cells, dead cells, debris) have a major impact on the measured OD_{600} values. Comparing both strains in Figure 4.4a and Figure 4.4b, yet, no difference in both, shape and size of *H. elongata* wildtype and ΔectC are observed. However, also expression levels and metabolic systems can result in OD_{600} variations [157]. The ectoine metabolism, a major regulation system [25, 158], is interrupted in the ΔectC mutant to accumulate γ-NADA, which may cause the OD_{600} discrepancy. This hypothesis is supported by the OD_{600} - *AFDW* correlation of *H. elongata* ΔectC σ38 [159], a second *H. elongata* strain with an intermittent ectoine metabolism. Again, neither in the exponential (Figure A.8a) nor in the stationary phase (Figure A.8b) morphology variations are apparent, but still the correlation factor is similar

to the ΔectC mutant and differs from the wildtype (Figure A.7). Another cause might be the OD_{600} range the *AFDW* calculation was performed; while in Hobmeier *et al.* [156] *AFDW* correlation was measured to a maximum OD_{600} of 1.2, in this work the range went up to 18.8 and 16.2 for *H. elongata* ΔectC and ΔectC σ38, respectively, to meet the cell amount in the described 1.5 L batch cultivation scale. Care was taken to ensure that the OD_{600} of the samples overlapped, starting the correlation with an OD_{600} value of 0.73 ± 0.08.

Summed up, establishing the correlation between the OD_{600} and the *AFDW* was a necessary step to further calculate the biomass in the batch cultivations of *H. elongata* ΔectC (see subsection 4.2.2 and subsection 4.2.3). A comparison of the following γ-NADA production processes with the one of ectoine is only possible when the obtained solute yields can be related to the cell weight. Further, the non-existent compliance of the correlations of the wildtype and the ΔectC mutants give a hint to the sensitivity of the bacteria strain to disturbance of the ectoine metabolism. As described in Vreeland & Martin [160], the shape of *H. elongata* maintains over a wide NaCl range in the medium, the correlation was used for both 0.5 M and 1.0 M NaCl cultivations, described in the next section (subsection 4.2.2).

4.2.2 1.5 L *lab*-scale – comparing the cultivation in 0.5 M and 1.0 M NaCl

Since NaCl triggers the solute production in *Halomonas elongata* [44, 161], the growth behavior and production of the solute γ-NADA was evaluated for *H. elongata* ΔectC – first in 1.5 L *lab* scale (discussed here) and later in 50 L pilot scale (see subsection 4.2.3). Figure 4.6a and Figure 4.6b map the batch cultivation of *H. elongata* ΔectC in the 1.5 L reactor system (*Biostat® B Plus Twin, Sartorius AG, Göttingen, Germany*) in MM63 medium with 15 g L^{-1} glucose, supplemented with 0.5 M and 1.0 M NaCl, respectively. The initial OD_{600} was set to 0.1.

The scatter plots show the increasing OD_{600} while the bar charts represent the γ-NADA concentration over the process time. However the cultivations under the given condition were performed several times (see subsection 3.2.2), just one cultivation run for each condition is shown exemplarily in Figure 4.6. In Table 4.1 all performed batch cultivations are averaged for the respective conditions. Comparing the cultivations with 0.5 M and 1.0 M NaCl, the similar final OD_{600} but disparate growth rates, finale γ-NADA concentrations and solute yields are striking. While in 0.5 M NaCl a maximum OD_{600} of 22.5±0.7 is reached after around 15 h, meaning a growth rate of 0.33±0.03 h^{-1}, it takes over 22 h to achieve the final OD_{600} of 24.3±1.5 in 1.0 M NaCl conditions. Thus, the growth rate drops to 0.26±0.01 h^{-1}. However, since the γ-NADA concentration increases from 0.62±0.11 g L^{-1} to 1.30±0.10 g L^{-1} with doubled NaCl amount, the economically relevant space-time yield improves despite longer

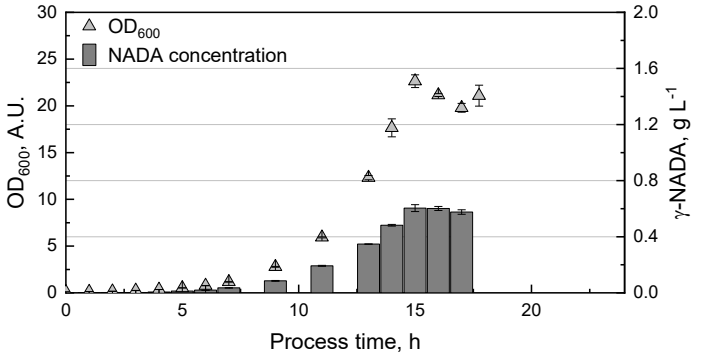

(a) 1.5 L reactor with 0.5 M NaCl.

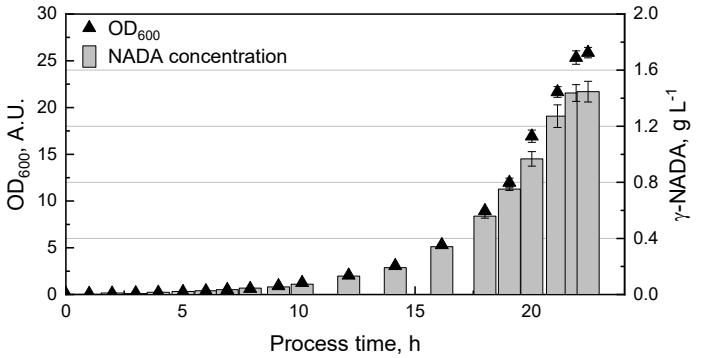

(b) 1.5 L reactor with 1.0 M NaCl.

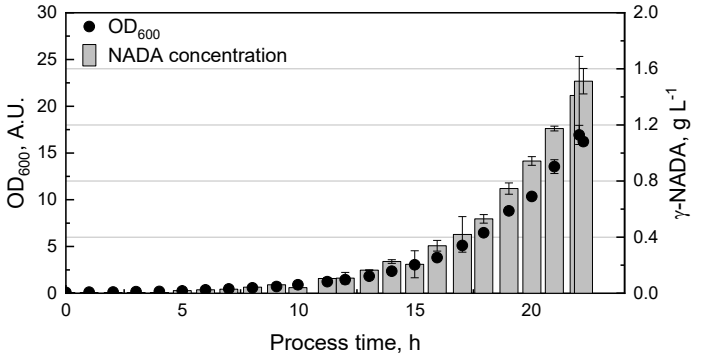

(c) 50 L reactor with 1.0 M NaCl.

Figure 4.6: Growth curve and γ-NADA concentration over the process time in 1.5 L (a,b) and 50 L (c) reactor with 0.5 M (a) and 1 M (b, c) NaCl, respectively. *H. elongata* ΔectC was cultivated in MM63 medium with 15 g L^{-1} glucose and varying salt concentration, with a controlled temperature of 30 °C and controlled pH of 7.0. Stirrer speed increases to control the pO_2 to 30%. γ-NADA was extracted from cells with freeze-thaw and analysed in HPLC. OD_{600} was measured spectrophotometically. Cultivation process was performed until provided glucose was consumed.

production time. *H. elongata* ΔectC produces 0.06±0.01 g L^{-1} h^{-1} γ-NADA in the high salt concentration, signifying an improved production rate by the factor 1.5 compared to 0.5 M conditions. Relating the produced γ-NADA amount on the biomass, which is assigned as ash free dry weight *AFDW* and calculated from the correlation in Equation 4.2, *H. elongata* ΔectC requires 0.1±0.00 and 0.2±0.01 g g^{-1} to compensate the osmotic pressure of 0.5 M and 1.0 M NaCl, respectively.

Table 4.1: Parameters for the evaluation of the cultivation of *Halomonas elongata* ΔectC in MM63 medium supplemented with 15 g L^{-1} glucose as carbon source and either 0.5 M or 1.0 M NaCl. Two working volumes, namely 1.5 L and 50 L, were tested.

Volume	**NaCl condition**	**Max. OD_{600}** [-]	**Growth rate** [h^{-1}]	**Final γ-NADA** [g L^{-1}]	**Final γ-NADA** [g g^{-1}_{AFDW}]	**Space-time yield** [g L^{-1} h^{-1}]
1.5 L	0.5 M	22.5±0.7	0.33±0.03	0.62±0.03	0.10±0.00	0.04±0.00
	1.0 M	24.3±1.5	0.26±0.01	1.30±0.18	0.20±0.01	0.06±0.01
50 L	1.0 M	16.2±0.4	0.24	1.51±0.10	0.35±0.02	0.07±0.00

The described, reduced growth rate with increasing salt concentration is known for halophilic organisms [162, 163], also for *H. elongata* [41, 156]. However, there is a salt optimum – both, Dötsch *et al.* [44] and Hobmeier *et al.* [156] describe an optimum for *H. elongata* wildtype somewhere between 0.5 M and 1.0 M NaCl. To compare the growth behavior of several *H. elongata* strains, Cánovas *et al.* [41] also designed an *H. elongata* mutant lacking of ectoine synthase and accumulating γ-NADA as final osmolyte. Here, the growth rate of the designed mutant was slower than the wildtype ones. When comparing the growth of the wildtype described in Dötsch *et al.* [44] and Hobmeier *et al.* [156] with the results of the *H. elongata* ΔectC cultivation in both NaCl conditions, shown in Table 4.1, this trend is confirmed. Even though the wildtype grows faster, the ΔectC variant produces more solute per biomass. While here 0.10 and 0.20 g g^{-1} γ-NADA are reached in 0.5 M and 1.0 M NaCl, respectively, Dötsch *et al.* [44] specifies the ectoine amount in their correlation lower for both conditions. Ono *et al.* [164] measured 35.5 μg g^{-1} and 78.1 μg g^{-1} ectoine under comparable salinities of 0.51 M and 0.86 M, respectively. These findings are consistent with the explanation of Cánovas *et al.* [41], that the NaCl sensitivity of the degraded *H. elongata* mutant for γ-NADA accumulation results from γ-NADA being the less effective solute compared to ectoine. Thus, more solute, in this case γ-NADA, has to be accumulated to withstand the osmotic pressure from the salinity conditions. This could also explain the reduced growth rate of the γ-NADA producing *H. elongata* strain. If a higher solute concentration is required to maintain the metabolism, less energy is directed to cell growth and thus growth rate decreases.

Nevertheless, the batch production process for γ-NADA in the *lab*-scale worked reproducible and robust for both tested salinities. Since the space-time yield in 1.0 M NaCl was higher with 0.06 g L^{-1} h^{-1}, this condition was chosen for the scaled-up process in the *pilot* reactor system which is described next in subsection 4.2.3.

4.2.3 50 L *pilot* scale – scale-up of the cultivation process

Since the *H. elongata* ΔectC cultivation in 1.5 L working volume with 1.0 M NaCl results in a doubled, final γ-NADA concentration and despite a longer process time in an improved space-time yield of 0.06±0.01 g L^{-1} h^{-1} (subsection 4.2.2), this condition was chosen to be scaled to a *pilot* reactor system (*LP75, Bioengineering AG, Wald, Switzerland*) with a working volume of 50 L. Figure 4.7 visualizes the process by mapping the recorded online process parameter oxygen saturation (pO_2), pH, stirrer speed and temperature in combination with the cell growth (OD_{600}).

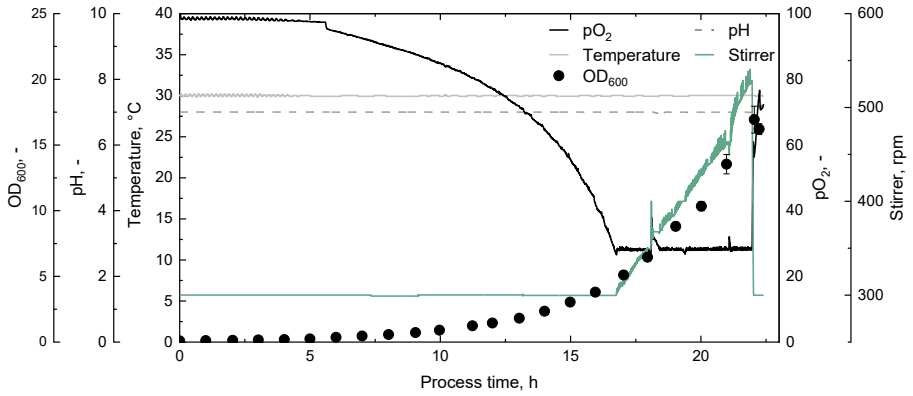

Figure 4.7: Cultivation process of *Halomonas elongata* ΔectC in MM63 medium and 1 M NaCl in 50 L reactor with recorded online parameters temperature, impeller speed, pH and pO_2 saturation. OD_{600} measurements were performed offline with spectroscopy.

Temperature and pH are controlled to 30 °C and 7, respectively, thus being constant over the whole process time. Since pO_2 control was set to 30 %, the stirrer speed increases at around 17 h to maintain the set value. The sharp pO_2 rise after 22 h, and thus the drop of the stirrer speed, indicates that the carbon sources of 15 g L^{-1} glucose is completely consumed, meaning the end of the cultivation and production process. Exponential growth of *H. elongata* ΔectC is preserved until the whole substrate is exhausted, thus indicating a robust mutant for the batch process scale-up.

A closer view on the γ-NADA concentration and associated bacterial growth (OD_{600}), in comparison to the *lab*-scale cultivation, is given in Figure 4.6c. Here again, the final process data are shown in Table 4.1. Compared to the 1.0 M cultivation in the *lab*-scale, a lower final OD_{600} of 16.2±0.4 and with this a reduced growth rate of 0.24 h^{-1} are achieved. However, the final γ-NADA concentration slightly rises to 1.51±0.10 g L^{-1}. Both effects condition the increased γ-NADA amount per biomass and the increased space-time yield, representing a successful scale-up of the cultivation process to *pilot*-scale. These findings path the way for further process advancement to industrially relevant volumes and other operating conditions. In general, up-sizing a cultivation process is not a fast-forward procedure, but every strain and production process requires different approaches [165]. Literature is repleted with established scale-up strategies [166, 167]. The scale-up of the cultivation of *H. elongata* ΔectC was performed according to a constant aeration level in the reactor. Further, a step-wise scaling of the processes from *lab*- to *pilot*- to *plant*-scale is crucial to maintain process performance [167]. Hewitt & Nienow [168] cite a couple of examples, showing that larger volumes of the process often result in less yield and Enfors *et al.* [169] conclude that this results from the cells, reacting to the less constant conditions in bigger sized reactors. However, the scale-up of the cultivation of *H. elongata* ΔectC shows that the used bacteria strain to produce γ-NADA relatively straightforward copes with altered environmental conditions in the *pilot*-scale. Thus, a further expansion of the batch process is considered likely.

In addition to a large scale, the industrial ectoine production with *H. elongata* benefits from two further process strategies – bacterial milking and the use of a leaky-mutant [2]. The "bacterial milking" procedure exploits the response of *H. elongata* to osmotic down-shocking – ejection of the intracellular solute content. Here, 155 mg g^{-1} ectoine can be harvested per process cycle [26]. Sauer & Galinski [26] further describe the evidence of γ-NADA among the excreted solutes, thus making the "bacterial milking" strategy a prospective, future process idea. In contrast, the leaky-mutant is an *H. elongata* strain with a modification in the TeaABC transporter genes [16]. This mutant not only excrete but also overproduce ectoine and further decouples biomass amount and solute yield in the process [2, 14]. Yet, this leakiness or even an overexpression has not been described for γ-NADA.

In summary, the cultivation of *H. elongata* ΔectC in a batch process worked out reproducible and scalable in both, *lab*- and *pilot*-scale. Since with higher salinity in the process a higher γ-NADA concentration and space-time yield was achieved, the cultivation condition with 1.0 M was chosen for the scale-up. A comparable product concentration and yields were gained in the *pilot*-process showing the robustness of the used bacterial strain and the applicability in a biotechnological production process.

Since the produced material of the *pilot*-scale process is further used in downstream process steps and their evaluation (section 4.3), cells from the 50 L cultivation were separated from supernatant with a disk separator (described in subsection 3.2.2), disrupted with osmotic shock and freeze-thaw and stored in 2 L aliquots for further use.

Table 4.2: Balance of the processing of the cultivation suspension after glucose was exhausted. Cells were harvested in a disc separator and cell disruption was performed with an osmotic shock by adding ddH_2O. This suspension was stored at -20 °C in aliquots for further use.

Process step	c_{before} [g L^{-1}]	c_{after} [g L^{-1}]	V_{before} [L]	V_{after} [L]	m_{before} [g]	m_{after} [g]	VCF [-]	CF [-]	Yield [%]	Recovery [%]	Purity [%]
Cell separation	-	14.0±0.6	50	3.6	-	50.2±2.0	13.9	9.23±0.7	66.5±4.8	-	-
Cell disruption	14.0±0.6	2.5±0.3	3.6	20	50.2±2.0	76.1±6.4	0.2	0.3±0.0	151.4±14.0	-	13.2±0.8

4.3 Filtration cascade

The filtration cascade, comprising a micro-, ultra- and nanofiltration step, follows the upstream cultivation, cell separation and cell disruption discussed in section 4.2. Microfiltration (*MF*) is performed as very first downstream process step to clarify the cultivation broth from cell debris and remaining particles. Subsequent ultrafiltration (*UF*) retains proteins and other dissolved molecules, whereas in nanofiltration (*NF*) the small molecule can be concentrated, however several ions are able to pass the membrane. Thus, a desalting is conceivable when the *NF* membrane retains γ-NADA while it is permeable for Na^+ and Cl^- ions.

4.3.1 Membrane and parameter screening

Developing a potent filtration cascade for the purification and concentration of γ-NADA from *H.elongata* ΔectC cultivation (see subsection 4.2.3) starts with a membrane and parameter screening for commercially available *MF*-, *UF*-, and *NF* flatsheet membranes. The specification of the membranes, provided by the supplier, are given in Table 3.9. The focus of the *MF* and *UF* membrane screening is placed on separating γ-NADA from cell debris and macromolecular contaminants, e.g., proteins, DNA. Here a high permeation (see Equation 2.7) of γ-NADA is desired. In contrast, the main goal of the *NF* is the concentration of the target with a high rejection of γ-NADA (see Equation 2.8) and a high permeation of NaCl to achieve desalting.

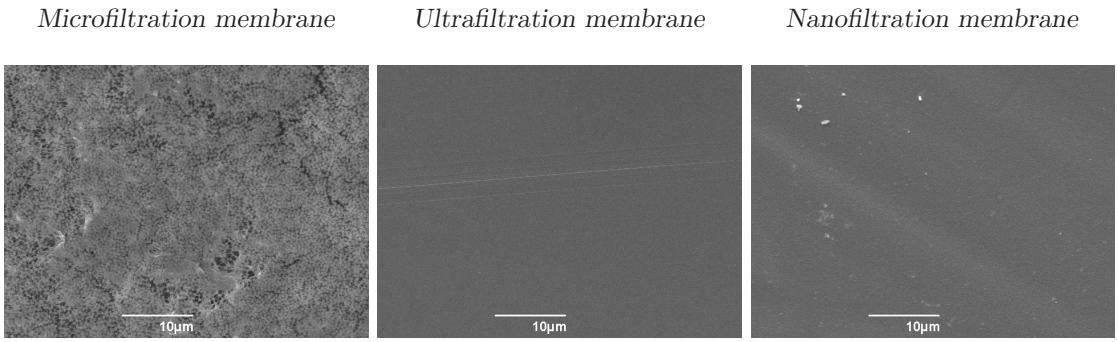

(a) *Synder V0.2* new. **(b)** *Synder MQ50* new. **(c)** *Desal/GE DL* new.

Figure 4.8: Scanning electron microscopy (*SEM*) pictures of the selected filtration membranes before using. Irradiation was performed with a 10 kV electron beam.

Figure 4.8 images the membrane surfaces of the selected, unused *MF*, *UF* and *NF* membranes with scanning electron microscopy (*SEM*). Consistent with the classification of the membranes dependent on the pore size and *MWCO*, described in subsection 2.3.1 and illustrated in Figure 2.4, the coarsely porous surface of the *Synder V0.2 MF* membrane stands out (see Figure 4.8a). The pore diameters of *UF* and *NF* membranes shown in Figure 4.8b and Figure 4.8c cannot be resolved. However, Figure 4.8 nicely visualizes both the decreasing pore sizes of the membranes and, with this, the varying pressure demand to overcome the resistance of the membranes. The following screening for *MF*, *UF* and *NF* membranes is performed with a feed flow rate (Q_F) of 10 L h^{-1} and 60 L h^{-1} each, however with different applied transmembrane pressure (Δp_{TM}) suitable for the respective filtration mode (see Table 3.11). Figure 4.9 exemplarily shows the online recorded process parameter of the conditions screening of the *Desal/Ge DL NF* membrane so that the experimental setup is illustrated. Δp_{TM} and Q_F were set to their respective constant values for 20 min equilibration time. After the 20 min period, Q_P was considered constant, permeate samples were taken, and the following conditions were adjusted. According to Hartinger *et al.* [120] filtration performance is not affected when Δp_{TM} is altered in ascending order, hence the two Q_F conditions were first performed at the lower Δp_{TM} and then at the higher Δp_{TM}.

As described in subsection 3.2.4, the screening was performed with a complex, for *UF* and *NF* preconditioned, feed composition from 50 L cultivation of *H. elongata*ΔectC (subsection 4.2.3). Thus, the permeation and rejection behavior of the components considered in each case, namely γ-NADA, proteins, and NaCl, cannot be evaluated independently. In addition, the membrane material could play a role.

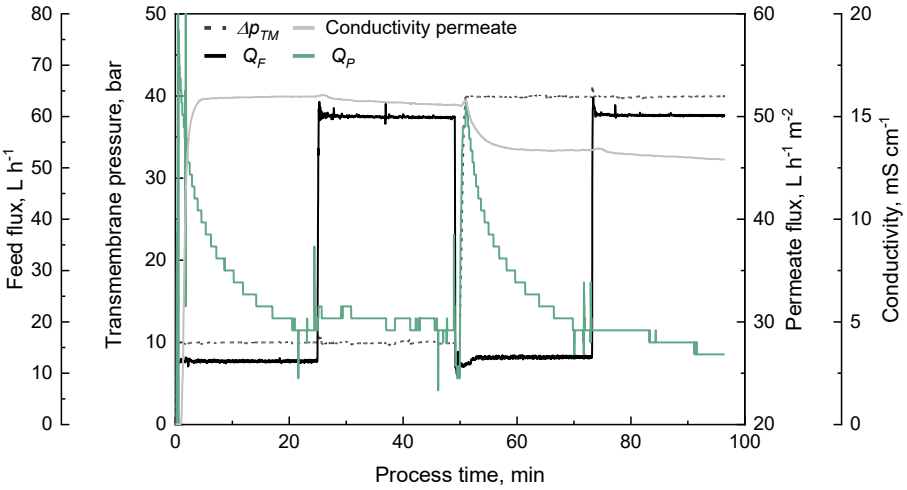

Figure 4.9: Recorded parameter during membrane screening, exemplary for *NF* membrane *Desal/GE DL*. Transmembrane pressure (Δp_{TM}), conductivity in permeate, feed flux (Q_F) and permeate flux (Q_P)are recorded online during filtration.

Microfiltration

The primary purpose of microfiltration (*MF*) is to separate undissolvable substances and, with this, clear the suspension for downstream process steps [170]. The main goal is to remove the target molecule of the biotechnological process from the producing cells [49], or lysed cell debris [55], and contaminants in micrometer size [171]. The screening of the five *MF* membranes, namely *Synder FR*, *Nadir MP005*, *Pall Supor 200*, *Synder V0.2* and *Pall Supor 450*, is performed at 35 °C and with varying Δp_{TM} and Q_F conditions listed in Table 3.11. Since the *MF* filtration step proceeds downstream of the cultivation, lysed fermentation broth from the 50 L cultivation described in subsection 4.2.3 was used as feed in the *MF* membrane screening. For each Δp_{TM} and Q_F combination, permeate samples were taken and the γ-NADA, protein and NaCl concentration was quantified according to subsection 3.2.6. The permeat flow (Q_P) is recorded online.

Figure 4.10a and Figure 4.10b show the permeation (Equation 2.7) of γ-NADA and proteins under the tested parameter conditions, respectively. Bar charts for the respective membranes are arranged with increasing pore size. Since the pore sizes of the membranes are indicated to be much greater than the molecular weight of γ-NADA (160.17 g mol^{-1}), a high permeation under all tested conditions were expected. As can be seen in Figure 4.10a, no significant difference between the membranes is visible, and neither pressure (Δp_{TM}) nor feed flux (Q_F) affect the permeation of γ-NADA. In contrast, the protein permeation shown in Figure 4.10b differs between the tested membranes. An increased permeability for proteins is expected

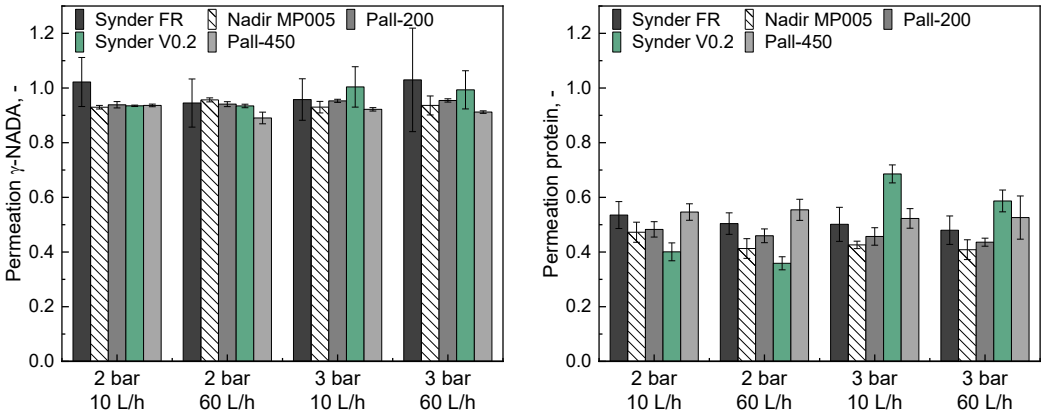

(a) γ-NADA permeation. **(b)** Protein permeation.

Figure 4.10: Microfiltration membrane screening; γ-NADA (a) and protein (b) permeation, tested for 5 different membranes, namely *Synder FR*, *Nadir MP005*, *Pall Supor 200*, *Synder V0.2* and *Pall Supor 450* shown with increasing cutoff from left to right. Transmembrane pressure (Δp_{TM}) and feed flux (Q_F) were set to 2 and 3 bar and 10 and 60 L h^{-1}, respectively.

with increasing pore size. The *Pall Supor 450* membrane with the biggest pore size of 0.45 μm indeed showed the best permeability for proteins at a Δp_{TM} of 2 bar; however, the same permeability is reached with the *Synder FR* membrane with the smallest pore size of 850 kDa. The best protein separation was obtained with *Synder V0.2* at 2 bar, yet, with increasing Δp_{TM} to 3 bar, the protein permeability of this membrane is nearly doubled. The other membranes stay unaffected of both, Q_F and Δp_{TM}. The different responses to changes in the operating conditions and the different protein permeability, independent of the membranes' pore size, might originate from the different materials specified by the suppliers (see Table 3.9). The same is observed by Hashino *et al.* [172] in filtration experiments with BSA. Here, not the pore size but the hydrophobicity of the membrane material has the most pronounced effect on the permeation and fouling in the process. Both *Synder* membranes are manufactured from polyvinylidene fluoride (*PVDF*), while the three others are composed of polyethersulfone (*PES*) (Table 3.9). These polymeric materials are among the most commonly used in *MF* processes across many research areas [49, 171] due to their mechanical and thermal stability. Yet, *PVDF* membranes generally have a more hydrophobic character than *PES* material, which might explain the low protein permeation with the *Synder V0.2* membrane. Here, a high interaction of proteins in the lysate with the hydrophobic *PVDF* membrane is expected, which could hinder the permeation [172, 173]. Yet, this effect would also be expected for the *Synder FR* membrane, also made from *PVDF*, which does not apply. In the experiments shown here, the membrane performance is assessed by the permeation of γ-NADA and proteins. Yet, bacteria and cell debris are present in the lysate, indirectly

influencing the permeation. Bacterial adhesion on the filter membranes also increases with increasing membrane hydrophobicity [174, 175]. Saeki *et al.* [174] further shows that even the occurring fouling layer differs in structure, dependent on the membrane material - hard and thin on *PVDF* and rough and thick on *PES*. Also, the surface quality and pore shape are relevant for the fouling behavior, and the process performance of the membrane [176, 177]. As shown in Dizge *et al.* [176], the initial drop of permeate flux in a membrane process is more distinct with larger pore size and rougher surfaces. *MF* contaminants can more easily penetrate larger pores and cause pore blocking than in smaller pores where particles are excluded. However, fouling due to concentration polarization was described as more pronounced with membranes with smaller pores. This might explain the higher permeability of proteins observed for the *Synder FR* membrane, although having the smallest pore size. Here, less pore blocking can be expected, and thus, less retention of biomolecules takes place. Ho & Zydney [177] showed that the membrane's pore structure - interconnected or straight - triggers protein fouling. This might also be the reason why the permeate flux Q_P, shown in Figure A.10a, does not correlate with the pore size of the tested membranes. Q_P increases with increasing Q_F when the lower Δp_{TM} of 2 bar is applied. The cake formation might be reduced here due to higher feed flux [178]. The resulting increased shear forces minimize the cake formation and height and promote a better Q_P. Also, the effect of concentration polarization on the permeate flux decreases with increasing Q_F [179]. When the higher Δp_{TM} of 3 bar is applied, Q_F does not have a pronounced effect on Q_P. Here, the higher pressure might compact the deposits, and thus, the removal is limited. All in all, not all occurring effects can be satisfactorily explained. However, this is the motivation for using the complex broth from fermentation rather than a model solution for the membrane screening. With a model solution, it would never be possible to observe all the occurring effects of the various molecules, which may reinforce or cancel each other out, but are the key deciding factors for the process design.

The membrane performance and suitability for the purification of γ-NADA were ranked according to the weight-sum method for multi-objective optimization [180–183] as described in section 3.2.4. The observed parameters are weight in descending order: γ-NADA permeation, Q_P, protein permeation, and NaCl permeation. Thus, the *MF* membrane *Synder V0.2* was identified as the best-performing membrane for the initial filtration step of the purification process of γ-NADA. This membrane was further used in an optimization step (detailed data shown in [184]). Here, an optimal temperature of 45 °C, Δp_{TM} of 3 bar and Q_F of 10 L h^{-1} were identified and applied in the long-term cascade process described in subsection 4.3.2.

Ultrafiltration

After the clarification with a *MF* step, ultrafiltration (*UF*) is performed to separate undesired proteins from the feed stream while γ-NADA remains in the permeate. Here, the previous screening is performed with three *UF* membranes, *Synder ST10*, *Synder MQ50* and *Synder LY100* (Table 3.9) and the conditions listed in Table 3.11. While in the above described *MF* screening lysed cultivation broth (see subsection 4.2.3) was used, here the solution was previously ultracentrifuged to settle and separate non-soluble contaminants, especially cell debris, and to mimic *MF* permeate. The supernatant was used as a feed solution in the *UF* membrane screening (see section 3.2.4).

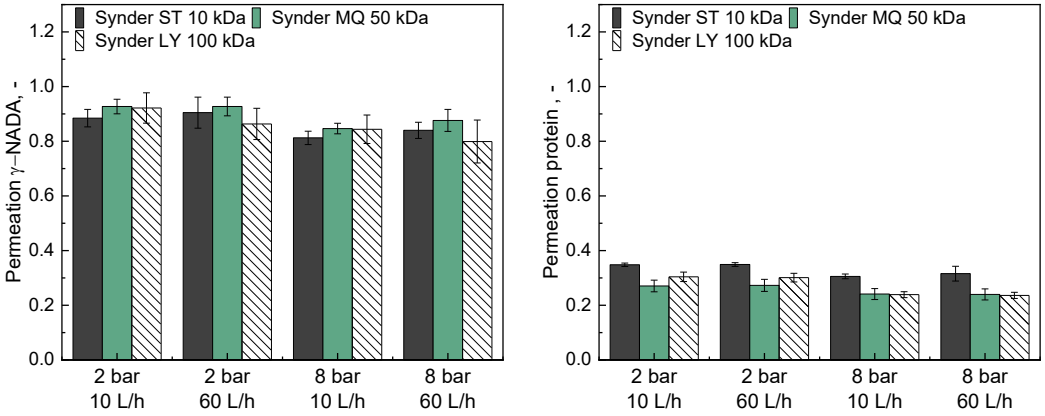

(a) γ-NADA permeation. **(b)** Protein permeation.

Figure 4.11: Ultrafiltration membrane screening; γ-NADA (a) and protein (b) permeation tested for three different membranes, namely *Synder ST10*, *Synder MQ50* and *Synder LY100* shown with increasing cutoff from left to right. Transmembrane pressure (Δp_{TM}) and feed flux (Q_F) were set to 2 and 8 bar and 10 and 60 L h^{-1}, respectively at a constant temperature of 35 °C.

Figure 4.11 shows the permeation of γ-NADA (a) and proteins (b) under screening conditions of 10 and 60 L h^{-1} and Δp_{TM} of 2 and 8 bar at a constant temperature of 35 °C.
As shown in Figure 4.11a, the observed permeation of γ–NADA does not considerably differ with different membranes. Yet, the best average-permeation of γ-NADA is achieved with the *Synder MQ50* membrane under the low-pressure conditions of 2 bar. γ-NADA permeation is not affected by Q_F; however, a slight drop of the permeation performance is observed with increased Δp_{TM}. This is particularly true for the permeation of proteins, shown in Figure 4.11b, when the *Synder LY100* membrane is screened. Similar behavior is reported by Bhattacharya *et al.* [50]; increasing Δp_{TM} results in higher retention of sugars due to the more compact and more impermeable fouling layer. However, also the inverse effect is reported [185]. As described for γ–NADA, the permeation of the charged components in the

feed, proteins, and salt (see Figure 4.11b, Figure A.9b) differs only slightly with different membranes and process conditions. However, both observed impurities follow the same trend within the applied process conditions - best desired separation with *Synder MQ50*, followed by *Synder LY100* and last *Synder ST10*. This is contrary to the observation of γ–NADA. Here, the rejection follows the reverse order when a Q_F of 10 L h^{-1} is applied, meaning the best desired permeation with the *Synder MQ* membrane. The observed membrane performance cannot be explained by different material properties, as in the case of *MF*, since all three membranes tested are composed of the same material, namely *PES*, and are purchased from the same supplier (see Table 3.9). Yet, as already described in subsection 2.3.1, charged and uncharged molecules behave differently in filtration processes. γ–NADA, an amino acid derivative, is a zwitterionic molecule [100] with a neutral net-charge at physiological conditions of the fermentation (see Table 3.8), typical for compatible solutes [14]. Thus, it's permeability seems mainly dependent on the steric hindrance of the membrane. This is also true for proteins, due to their molecular size, yet also charge might play a role. This is supported by the similar permeation of NaCl (Figure A.9b), which should not be hindered by the membrane. As described in Rohani & Zydney [75], salt disturbs the charged interaction of proteins and the membrane. Further, the effective size of the protein differs with ionic strength - the lower the ion concentration, the larger the effective protein size [73]. Thus, even without a charge interaction, protein permeation is affected by NaCl, which cause the permeability of the membranes independent of the *MWCO*.
The permeate flux (Q_P), shown in Figure A.10b, depends mostly on the *MWCO* of the tested membranes and additionally increases with increasing Δp_{TM}. This effect is more pronounced the smaller the *MWCO* of the tested membranes. In general membrane processes, a higher Δp_{TM} results in an increased Q_P. Yet, in complex solutions containing organic material, the transport of foulants to the membrane increases. With this fouling due to gel layer formation, adsorption and pore blocking, and concentration polarization becomes the dominating effects in the filtration process [186]. Thus,the initial Q_P increases with increasing Δp_{TM}, however the fouling tendency also increases [185, 187, 188]. Since the above-described screening for *UF* membranes is performed with a complex supernatant of *H. elongata* ΔectC cultivation (see subsection 4.2.3) these fouling effects most likely have an influence.

As already described for the *MF* screening, the most suitable *UF* membrane for the purification of γ-NADA was selected according to the weight-sum method for multi objective optimization [180–183]. Thus, *Synder MQ50* and the operation conditions of 10 L h^{-1} and 2 bar were identified and used in further longterm and cascade experiments (see subsection 4.3.2).

Nanofiltration

For the nanofiltration (*NF*) step, seven membranes were initially screened based on their γ-NADA rejection and desalting ability. Here, a Δp_{TM} of 10 and 40 bar and a Q_F of 10 and 60 L h^{-1} were tested at a constant temperature of 35 °C. In Figure 4.12 γ-NADA (a) and NaCl (b) rejection are shown for the tested membranes at the respective parameter conditions (listed in Table 3.11).

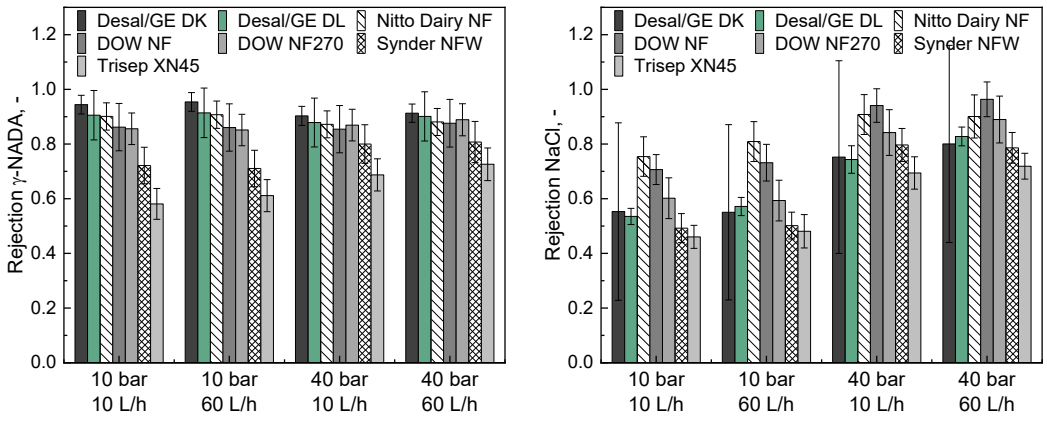

(a) γ-NADA rejection. **(b)** NaCl rejection.

Figure 4.12: Nanofiltration membrane screening; γ-NADA and NaCl rejection tested for 7 different membranes, namely *Desal/GE DK*, *Desal/GE DL*, *Nitto Dairy NF*, *DOW NF*, *DOW NF270*, *Synder NFW*, *Trisep XN45* shown with increasing *MWCO* from left to right. Screening parameters transmembrane pressure (Δp_{TM}) and feed flux (Q_F) were set to 10 and 40 bar and 10 and 60 L h^{-1}, respectively.

It is generally known that in *NF* the rejection of uncharged, (organic) molecules is primarily dependent on the steric hindrance of the *MWCO* of the respective membrane [52, 54]. Also the polarity of the compound plays a role since a dipole character promotes a better orientation towards the charged membrane surface and with this, an increased permeation ability [78]. The screening results shown in Figure 4.12 fit well with the described separation effects. The γ-NADA rejection, shown in Figure 4.12a, appears to be *MWCO* dependent. Bar charts, representing the tested membranes, are presented in ascending order, suggesting a lower rejection with higher *MWCO*. γ-NADA and in general most compatible solutes are known to be both, uncharged but have a zwitterionic character, however, in this screening a charged surface for all tested membrane is assumed and thus, polarity effects can be neglected. Same as for γ-NADA, the protein rejection decreases with increasing pore size (see Figure A.9c). Here, a sieving effect depending on the pore size is assumed to be dominant. Regarding the rejection of NaCl in Figure 4.12b, a completely different picture emerges. Although having a moderate *MWCO*, compared to the other *NF* membranes, the highest rejection of NaCl is achieved

with *Nitto Dairy NF* and *DOW NF*. As expected, the lowest rejection is obtained with the membranes having the highest *MWCO*. In contrast to the rejection of uncharged solutes, the ion rejection in *NF* can be explained by *Donnan* exclusion – electrostatic interaction between the membrane and the solute dominate the separation and thus affect the permeation [52, 54, 189]. Multivalent ions are retained much better than monovalent ions and further, rejection decreases with increasing ion concentration in the feed stream [48, 52]. Thus, the specific membrane characteristic of the tested membranes, and not the pore size, mainly influences the retention of NaCl, however with increasing pore size, the dominant effect changes.
In case of *Desal/GE DK*, *Desal/GE DL*, *Nitto Dairy NF*, *DOW NF* and *DOW NF270*, neither the applied Δp_{TM} nor Q_F affect the concentration of γ-NADA in the retentate. However for the membranes with the biggest *MWCO*, *Synder NFW* and *Trisep XN45*, a slight pressure dependence is observable. In contrast to the effects in the γ-NADA retention, all membranes show an increased rejection with increased Δp_{TM}, however stay unaffected by Q_F. As explained in Melin & Rautenbach [48], the convective transport through the membrane increases in contrast to the diffusive transport with increasing pressure, thus the rejection of salt increases. Lai & Nguyen [190] observed a contrary effect when processing fish sauce. Here NaCl rejection decreases with increasing Δp_{TM}, however it is explained by the higher permeate flux and thus a promoted electromigration through the membrane. Yet, as shown in Figure A.10c, Q_P is not positively influenced by Δp_{TM}. Only *Desal/GE DK* and *Nitto Dairy NF* show a slight dependence on Δp_{TM} - a higher pressure results in a reduced permeate flux. Due to the comparatively high pressure in *NF*, Q_P is in the same range as for *UF* and *MF* . Surprisingly, the three membranes with the smallest *MWCO* show the highest Q_P when a Δp_{TM} of 10 bar is applied. This might result from fouling, since in the described screening, a complex mixture from cultivation with various species of organic contaminants was used. Guo *et al.* [191] showed that macro-molecular foulants such as proteins and polysaccharides as well as small molecules trigger organic fouling in *NF* processes. A higher *MWCO* of the membrane and with this a bigger pore size promotes penetration of molecules and support internal membrane fouling . With increased Δp_{TM}, Q_P of the screened membranes converge. With increased pressure, the fouling is also supported for the membranes with smaller pore size and thus, Q_P converges. In the *NF* membrane screening of Boussu *et al.* [192], a higher Q_P is traced back to the membrane characteristics – *Desal* membranes are described to be more hydrophilic and thus prevent intense fouling. Also in the screening described in this section, the *Desal* membranes are the ones with the highest Q_P and further the most stable Q_P was obtained with *Desal/GE DL* under the tested condition.

This *Desal/GE DL* membrane was finally selected, again based on the weight-sum method for multi objective optimization [180–183]. With this membrane, the process conditions of 10 bar and 10 L h^{-1} showed the best filtration performance. For the ranking following

resulting parameter were taken into account in descending order: γ-NADA rejection, NaCl and protein permeation, Q_P.

The performed and above described membrane and parameter screening for the purification of γ-NADA demonstrated clearly, that an initial screening is crucial for an efficient final filtration process. The individual membrane behavior, the membrane material [187, 192, 193], hydrodynamic conditions [187, 188, 194] and the composition of the feed stream [188, 191, 192, 195, 196] influence the whole process due to their responsibility on concentration polarization, gel layer formation, sieving effects, charge effects and fouling like adsorption, cake building and pore blocking. In addition, these fouling and separation effects cannot be traced back to only one parameter, but also arise from combinations of these and further affecting each other [191, 197, 198]. This is supported by the fact, that nearly every fouling effect is described for every filtration size. Thus, a prediction only narrows the membranes and conditions and membranes to be tested, making a screening indispensable. In the following subsection 4.3.2 the chosen membranes *Synder V0.2*, *Synder MQ50* and *Desal/GE DL* were used in the cascade process consisting of successive *MF*, *UF* and *NF*, respectively.

4.3.2 Purification of Nγ-acetyl-L-2,4-diaminobutyric acid from cultivation with a filtration cascade

The filtration cascade, consisting of successively performed microfiltration (*MF*), ultrafiltration (*UF*), and nanofiltration (*NF*), follows the up-stream cultivation process in the 50 L reactor with 1.0 M NaCl (see subsection 4.2.3). The prior screening of the membranes for the three steps in subsection 4.3.1 resulted in the following membranes: *Synder V0.2* for *MF*, *Synder MQ50* for *UF* and *Desal/GE DL* for *NF*. For each step the lower Q_F of 10 L h^{-1} was chosen with a Δp_{TM} of 3 bar, 2 bar and 10 bar for *MF*, *UF* and *NF*, respectively (see Table 3.12). The cascade starts with processing the cultivation broth after cell separation and disruption (see subsection 4.2.3 and Table 4.2) with a *MF* cross-flow step. The permeate was collected and fed downstream in *UF*. Again, the *UF* permeate was collected for the subsequent *NF*, where γ-NADA was finally concentrated in the retentate.

Each filtration step was monitored over the whole process time, which is presented in Figure 4.13, Figure 4.14 and Figure 4.15 for *MF*, *UF* and *NF*, respectively. Temperature, Δp_{TM}, Q_F and Q_P were recorded online, while permeate samples were analyzed periodically according to subsection 3.2.6 to get first, a snapshot of the current permeation behavior and second, a deeper insight into the long-term performance of the membranes and the respective filtration step.

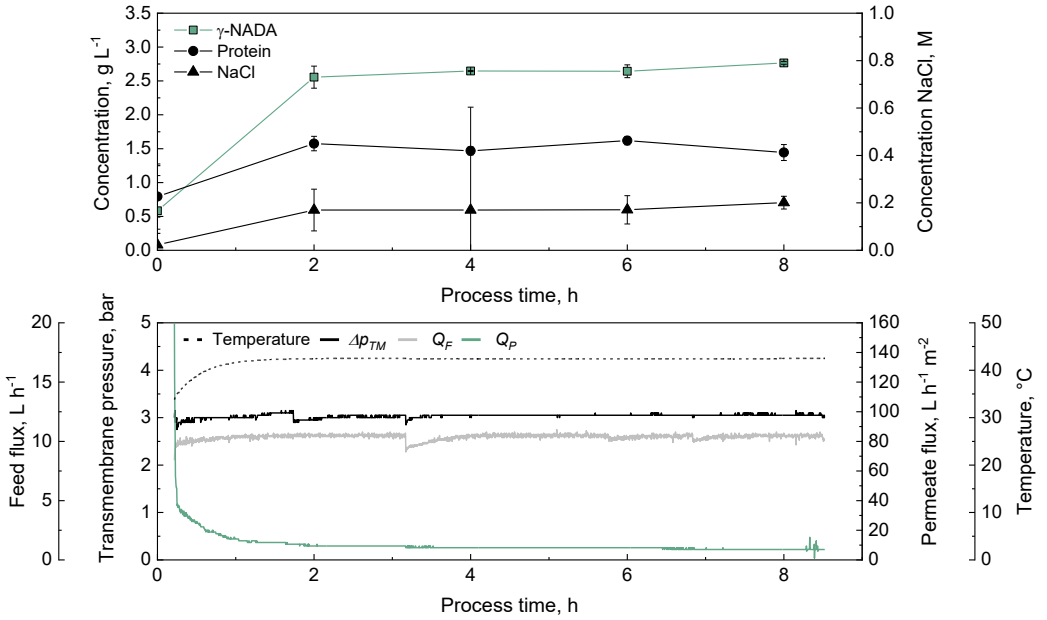

Figure 4.13: First longterm *MF* process for the purification of γ-NADA with the previously screened *Synder V0.2* membrane and with 3 bar and 10 L h^{-1} for Δp_{TM} and Q_F, respectively (see subsection 4.3.1). permeate samples were taken periodically over the process and γ-NADA, protein and NaCl content was analyzed as described in subsection 3.2.6. Temperature, Δp_{TM}, Q_F and Q_P were recorded online.

In each filtration step, Q_F and Δp_{TM} were set to a value of 10 L h^{-1} and the respective pressure and thus remain constant over the processing time. The temperature was set to 45 °C in *MF* and 35 °C in *UF* and *NF*; however, it was beyond control. After a sharp rise at the beginning of the process due to transport delay in the tubing, in both *MF* and *UF* γ-NADA and NaCl concentration in the permeate stay constant over time (see Figure 4.13 and Figure 4.14) in the range of the respective feed concentration (see Table 4.3) meaning a complete permeation of these feed components. In *MF* also, the permeating protein concentration remains constant over time, significantly differing from the initial feed concentration of 3.3±0.7 g L^{-1}. Here, the protein was effectively retained and separated from the target stream with a remaining protein concentration of 1.0±0.1 g L^{-1} in the final permeate suspension (see Table 4.3). This protein separation is nicely visualized in Figure A.11; feed and concentrate sample shows a dense protein band, whereas, in the permeate, the protein concentration is too low to be resolved. Comparing these results with the screening in subsection 4.3.1 and Figure 4.10b, an even higher protein rejection and, thus, a better purification of the process stream was obtained. Due to the accumulation of the retained foulants on the *MF* membrane surface, membrane fouling and concentration polarization occur likely, and thus, Q_P decreases with ongoing process [191].

Table 4.3: γ-NADA, protein and NaCl concentration in the inset feed stream and the permeate and concentrate after respective filtration step.

Process stream	Microfiltration			Ultrafiltration			Nanofiltration		
	$\mathbf{c}_{\gamma-NADA}$ [g $\mathbf{L}^{-1}$]	$\mathbf{c}_{Protein}$ [g $\mathbf{L}^{-1}$]	$\mathbf{c}_{NaCl}$ [M]	$\mathbf{c}_{\gamma-NADA}$ [g $\mathbf{L}^{-1}$]	$\mathbf{c}_{Protein}$ [g $\mathbf{L}^{-1}$]	$\mathbf{c}_{NaCl}$ [M]	$\mathbf{c}_{\gamma-NADA}$ [g $\mathbf{L}^{-1}$]	$\mathbf{c}_{Protein}$ [g $\mathbf{L}^{-1}$]	$\mathbf{c}_{NaCl}$ [M]
Feed	2.5±0.3	3.3±0.7	0.2±0.1	2.4±0.1	1.2±0.0	0.2±0.0	1.8±0.0	1.4±0.0	0.2±0.0
Permeate	2.7±0.1	1.0±0.1	0.2±0.1	2.4±0.0	1.8±0.1	0.2±0.1	1.0±0.0	1.3±0.0	0.1±0.0
Concentrate	2.3±0.5	4.7±1.3	0.2±0.1	2.6±0.0	1.9±0.1	0.3±0.0	15.8±1.0	4.8±0.2	0.2±0.1

The same applies to the *UF* process in Figure 4.14. The set values temperature, Δp_{TM} and Q_F stay constant over the whole process time of 32 h, while Q_P decreases to around 8 L m^{-2} h^{-1} due to membrane fouling. As mentioned above, γ-NADA and NaCl concentration stay constant in the permeate samples (see Figure 4.14). Applied to both feed, permeate and concentrate concentration do not differ significantly after the *UF* step (see Table 4.3), meaning an unhindered permeation of these species. This is in good agreement with first, the expected results due to the *MWCO* of the *Synder MQ50* membrane and second, the results from the membrane screening described in subsection 4.3.1. In the long-term experiment, an even higher permeation for both species was obtained. In contrast to the screening in subsection 4.3.1, in the long-term experiment, the *MF* step was performed upstream of the *UF*. As described above, in the *MF* process, colloids and approximately 70 % of the protein content were retained and thus, drastically lowering the fouling content for the *UF* step. A higher foulant concentration has a negative impact on the fouling behavior of the membrane [188, 199, 200], thus explaining the lower permeation of the solutes in the screening.

Regarding the protein content, the situation appears different. Throughout the process, the protein concentration, shown in Figure 4.14, increases to 2.2±0.0 g L^{-1} in the last examined permeate sample. Thus, the final $c_{Protein}$ in permeate and concentrate after the *UF* step are comparable with a concentration of 1.8±0.1 g L^{-1} and 1.9±0.1 g L^{-1}, respectively, which indicates that no protein is rejected. This is inconsistent with the findings in subsection 4.3.1 – here, a protein permeation of only 27.1±2.1 % under the chosen conditions was evaluated. The concentration in the initial feed of 1.2±0.0 g L^{-1} also does not fit the comparatively high permeate and concentrate values, and thus, the mass balance does not work out. Yet, the conclusions from the *SDS*-gel in Figure A.11 are better aligned with the expected results. While the protein concentration in feed and permeate of *UF* is below the resolution limit, protein bands are visible in the concentrate, meaning a rejection of protein in *UF* indeed. The discrepancies might originate from several reasons: firstly, the *BCA*-assay is not the most accurate quantification method [201]. Since $c_{Protein}$ in permeate and concentrate in Table 4.3 and the protein amount visualized in Figure A.11 differ, the *BCA*-assay as used

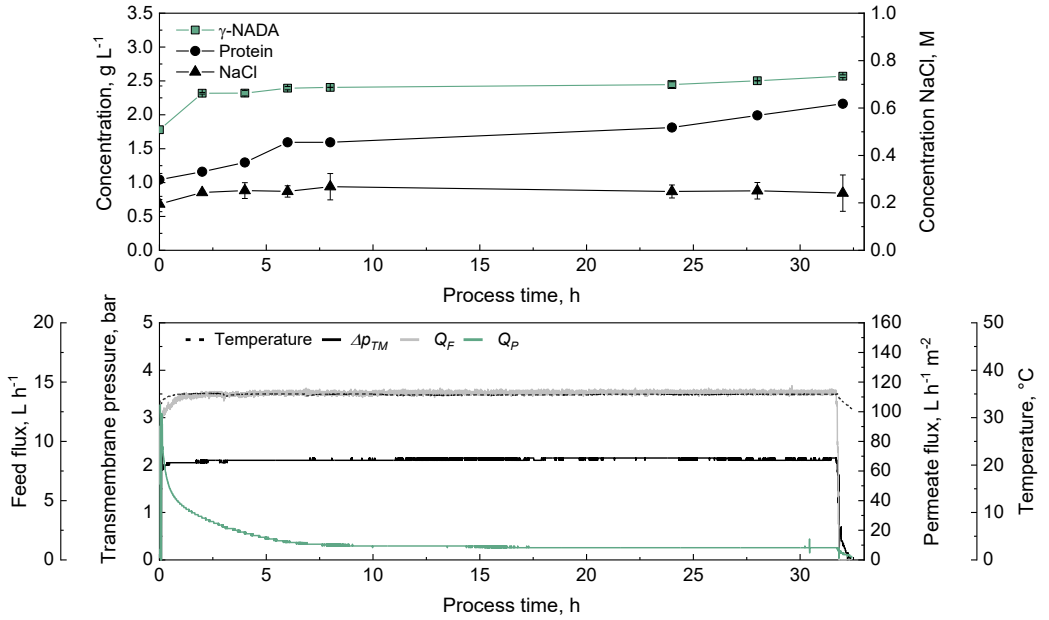

Figure 4.14: Longterm *UF* process for the purification of γ-NADA with the previously screened *Synder MQ50* membrane and with 2 bar and 10 L h^{-1} for Δp_{TM} and Q_F, respectively (see subsection 4.3.1). permeate samples were taken periodically over the process and γ-NADA, protein and NaCl content was analyzed as described in subsection 3.2.6. Temperature, Δp_{TM}, Q_F and Q_P were recorded online.

quantification method might be prone to errors when using complex solutions. Second, the detected protein concentration in the permeate might result from small peptides which can pass the membrane's *MWCO* of 50 kDa, react in the assay [202, 203] but cannot be resolved in the gel. As already described, the *UF* membrane screening was performed with the supernatant of ultracentrifuged, lysed cell suspension (see section 3.2.4) and not with permeate from previous *MF*. The feed composition in *UF* screening consists of 3.1 g L^{-1} γ-NADA, 3.0 g L^{-1} protein and 0.1 M NaCl, which differs from the feed content in the longterm experiment (see Table 4.3), in particular for γ-NADA and the protein amount. The protein concentration might be more effectively reduced with the applied *MF* than with ultracentrifugation. This alters the retention property of the downstream *UF* membrane and explains the discrepancies between subsection 4.3.1 and the long-term experiment.

Going on in the process with the *NF* step shown in Figure 4.15, the set parameters temperature, Δp_{TM} and Q_F remain stable at their respective values of 35 °C, 10 bar and 10 L h^{-1}. Yet, at around 22.7 h the recorded signals of Δp_{TM} and Q_F become noisy. Additionally, the concentration of γ–NADA and protein in the permeate change at the end of the process. In the first hours, the constant γ-NADA concentration in the permeate fits the rejection values in the membrane screening (see Figure 4.12a). However, at some point in the process,

the concentration in the permeate rises (see Figure 4.15). The same trend is observed for the protein concentration in the permeate. The NaCl concentration stays constant at around 0.2 M in the permeate samples throughout the process. This is also the measured concentration in the initial feed sample (see Table 4.3). Thus NaCl permeates unimpeded through the membrane. As already seen for *MF* and *UF*, Q_P falls with the ongoing process.

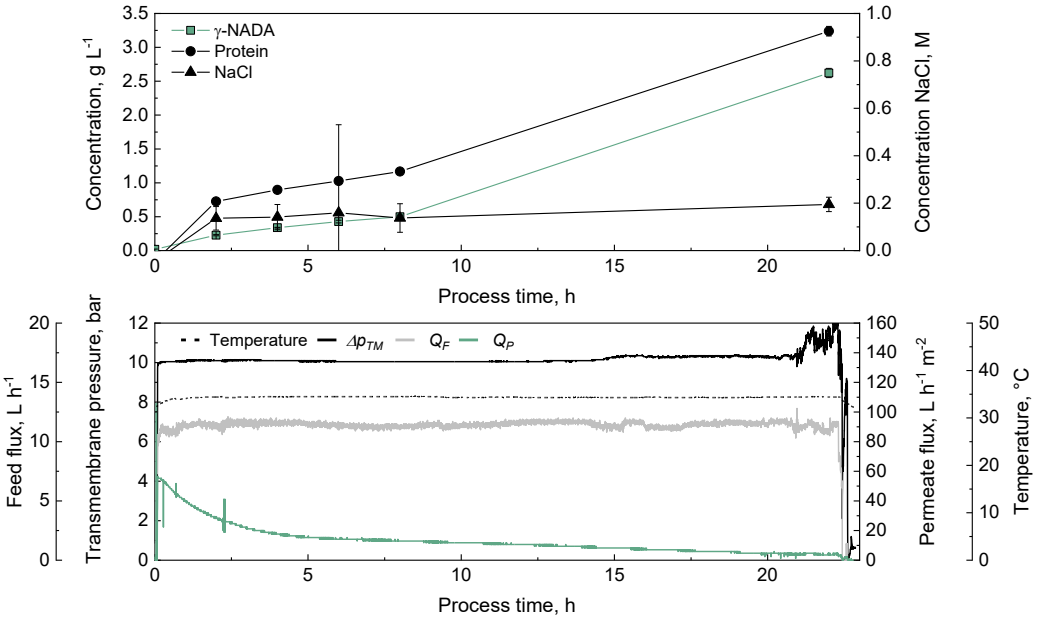

Figure 4.15: Longterm *NF* process for the purification of γ-NADA with the previously screened *Desal/GE DL* membrane and with 10 bar and 10 L h^{-1} for Δp_{TM} and Q_F, respectively (see subsection 4.3.1). permeate samples were taken periodically over the process and γ-NADA, protein and NaCl content was analyzed as described in subsection 3.2.6. Temperature, Δp_{TM}, Q_F and Q_P were recorded online.

As already mentioned above, the noisy signals of Δp_{TM} and Q_F may indicate damage or even breakthrough of the membrane at approx. 22.7 h due to the sustained loading. Since both protein and γ-NADA were concentrated before, the high concentration in the permeate samples compared to the feed (see Table 4.3) at 32 h is explainable. This could also explain the relatively high γ-NADA concentration in the total permeate (see Table 4.3) compared to expected values according to the *NF* membrane screening in Figure 4.12a. Nevertheless, a final γ-NADA concentration of 15.8±1.0 g L^{-1} is reached in the concentrate. As already seen for the protein content in the *UF* step, the expected amount of permeated protein based on the screening in subsection 4.3.1 does not match with the obtained protein in the long-term experiment shown in Table 4.3. However, the untypical high concentration in the permeate could be explained by the perceived problems in operation at the end of the process. But again, the protein concentration in all process streams – feed, permeate and concentrate

– does not fit the mass balance. Considering the *SDS*-gel in Figure A.11, $c_{Protein}$ in the concentrate (Table 4.3) does not match with the very light protein band.

Table 4.4: Balance of filtration cascade, for the target molecule γ-NADA, consisting of serial *MF*, *UF* and *NF* step. Cascade was performed with the respective membranes and conditions from the screening in subsection 4.3.1. permeate of the prior step was used as feed in *UF* and *NF*. Disrupted and stored suspension from the cultivation (subsection 4.2.3) was used as feed in *MF*.

Process step	c_{before} [g L^{-1}]	c_{after} [g L^{-1}]	V_{before} [L]	V_{after} [L]	m_{before} [g]	m_{after} [g]	VCF [-]	CF [-]	Yield [%]	Recovery [%]	Purity [%]
Microfiltration	2.5±0.3	2.7±0.1	5.2	3.6	13.2±0.3	9.5±0.1	1.5	1.5±0.2	72.4±2.0	72.0±2.0	15.8±1.7
Ultrafiltration	2.4±0.1	2.4±0.0	3.5	3.3	8.4±0.1	7.9±0.0	1.1	1.0±0.0	93.8±0.6	93.2±0.6	13.1±0.9
Nanofiltration	1.8±0.0	15.8±1.0	3.4	0.2	6.1±0.0	3.2±0.9	16.6	8.8±0.6	52.8±16.3	24.0±16.4	44.8±16.3
Total	2.5±0.3	15.8±1.0	5.2	0.2	13.2±0.3	3.2±0.9	25.8	6.2±0.9	24.2±7.5	11.0±7.5	44.8±16.3

Having previously considered each filtration step individually, the balance of the whole filtration cascade to purify γ-NADA from saline cultivation broth is shown in Table 4.4. Here, the γ-NADA concentration (c) and mass (m) before and after the respective step, the processed volume (V), the volume concentration factor (VCF), the concentration factor (CF), yield, recovery and purity of γ-NADA are presented for each filtration step and the total cascade. As already described, c_{before} and c_{after} in feed and permeate of *MF* and *UF* stayed in the same concentration range, since γ-NADA permeates constantly unhindered (see Figure 4.13 and Figure 4.14). In *NF* γ-NADA was finally concentrated to c_{after} of 15.8±1.0 g L^{-1} with a purity of 44.8±16.3 %. Overall, 5.2 L of lysed cell suspension from cultivation (see subsection 4.2.3) was processed and concentrated to a final V_{after} of 0.2 L after *NF*. Of the original m_{before} of 13.2±0.3 g γ-NADA, m_{after} of 3.2±0.9 g could be recovered, meaning a yield of 24.2±7.5 %. Most of the target was lost in *MF* and *NF* steps with a yield of 72.4±2.0 % and 52.8±16.3 %, respectively. In *UF*, a yield 93.8±0.6 % was obtained in the process. Since in both *MF* and *UF* γ-NADA permeates without rejection, the operation mode of filtration, namely cross-flow filtration (Figure 2.5b), is the main reason for the loss of the target during filtration. Cross-flow filtration has the advantages of a better process control [54], yet a tangential flow creates disadvantages. Some feed volume has to be preserved, and some target is lost. An alternative to cross-flow could be dead-end filtration (see Figure 2.5a), which is more detailed described in subsection 2.3.1. Here, the complete feed volume passes the membrane while a dense filter cake is formed with an ongoing process [54]. Thus, no volume loss occurs; however, the filter cake formation limits Q_P and makes the filtration step at some point uneconomic.

In the *NF* step, the reduced yield may result from the increased permeation at the end of the process (see Figure 4.15). If the retention of the target would have maintained at the constant level of approx. 0.5 g L^{-1} and best at the level shown in Figure 4.12a in subsection 4.3.1, the yield would increase significantly. Due to the dead volume of the filtration plant (*Cube80-VA*)

in both permeate and concentrate, recovery and yield differ - when regarding the concentrate in *NF*, less than half of the theoretical yield can be recovered (see Table 4.4).

In summary, the obtained results from the screening in subsection 4.3.1 could be mostly applied to the long-term cascade process of subsequent *MF*, *UF*, and *NF*. However, fouling in filtration processes occurs in mainly two steps (reviewed in [204]); thus, differences in short- and long-term performance were expected. Here, Wang & Tang [187] showed that the initial, sharp drop of Q_P results from the interaction and thus adsorption of foulants and the membrane surface; the long-term behavior of Q_P results from the interaction of the accumulated cake layer and remaining contaminants in the feed stream. Baker [205] even defines a usual Q_P in *UF* after the first drop - 50 L m^{-2} h^{-2}. The slow decrease in Q_P results from secondary fouling. Both effects are dependent on the feed composition. This reveals the benefits of the cascade filtration process; each upstream step minimizes the foulant content in the next feed stream and lowers the fouling tendency. This positive effect is, for example, shown by Alves *et al.* [206] for the purification of xylitol and Lai & Nguyen [190] for the processing of fish sauce. Further, membranes' lifetime depends on the overall loading during the filtration process[207]. In the *MF* process (see Figure 4.13), a high concentration of undissolved, lysed cell particles and other organic macro- and small molecules from cultivation (see subsection 4.2.3) are present in the feed stream, which likely exceed the holding capacity of the membrane. Thus, this process step was performed three times, which is the main reason for the reduced yield in *MF* compared to *UF* (see Table 4.4). The intense loading due to the long process time might also be the case of the disturbances in the *NF* step (Figure 4.15). The more permeate volume is processed, the higher the fouling resistance [191], and thus the exceeded capacity cause the observed inconsistencies. Although this was assumed to be the main reason for the insufficient rejection and recovery of γ-NADA in *NF*, a further optimization for the used *Desal/Ge DL* membrane was performed and is discussed in the next subsection 4.3.3.

An aspect, which has not been discussed here so far, is the potential behavior of γ–NADA in water and its effect on proteins during filtration. For the related compatible solutes ectoine and hydroxyectoine, the formation of a defined hydration shell in water is described [21, 140]. Zeman *et al.* [23] further shows that the water structure, arranged around the solutes, is stabilized with increasing concentration. Yet, it is also reported that salt can compensate for the water-forming effect of ectoine due to its contrary impact on the water structure [20, 208]. Especially during *NF* (Figure 4.15), the concentration ratios of γ–NADA with water and salt changes during the separation process. An increasing γ–NADA concentration and a reduction of NaCl related to the compatible solute in the concentrate might, in theory, increase the arranging of structured water molecules and, thus, the filtration resistance. This effect would be beneficial for the retention of γ–NADA in the concentrate, yet it would slow

down Q_P and decrease the efficiency of the process. These effects cannot be clarified based on the data shown here, although they might become relevant when a larger volume is processed. Here, a higher concentration and desalination of γ–NADA would be reached, and thus, effects might become more dominant.

4.3.3 Optimization

After identifying the *Desal/GE DL* membrane in the nanofiltration screening (see section 4.3.1) a more extensive optimization was performed. Since no effect of the feed flow rate was detected in the screening, this parameter was set constant to 10 L h^{-1}. The temperature (T) and the transmembrane pressure (Δp_{TM}) were varied from 25 to 45 °C and 5 to 40 bar, respectively, while the respective other was kept constant.

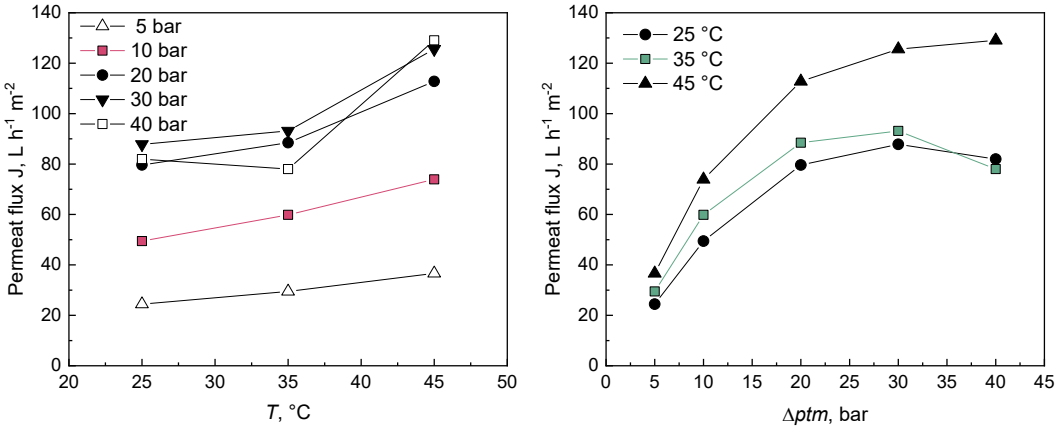

(a) Temperature dependence. **(b)** Transmembrane pressure dependence.

Figure 4.16: Permeate flux dependent on T (a) and Δp_{TM} (b). *Cross-flow* nanofiltration was performed with the *Desal/GE DL* flat sheet membrane with a filtration area of 0.0085 m^2 and a feed flow rate of 10 L h^{-1}. Permeate flux J was measured online via conductivity in the *Cube80-VA* system from *SIMA-tec*.

Figure 4.16 shows the resulting permeate flux Q_P dependent on both, the temperature (Figure 4.16a) and the transmembrane pressure (Figure 4.16b). Both, a higher temperature and a higher pressure have a positive effect on Q_P. While Q_P increases linear with increasing T, the impact of Δp_{TM} appears asymptotic to a maximum. However, the steeper rise of Q_P clarifies, that the effect of increasing Δp_{TM} is more dominant than the effect of increasing T. A higher applied transmembrane pressure compacts the membrane, which might result in a more effective permeate flux through the pores [209]. Mänttäri *et al.* [210] support the effect of T on Q_P. Further, Bandini & Morelli [211] and Goulas *et al.* [209] consider it unlikely that the pore size is affected by swelling through temperature effects. Supporting this, Tsuru

et al. [212] explains the temperature effect for the filtration of neutral solutes as follows: firstly, an increased temperature results in a reduced viscosity of the solvent and thus, in a reduced membrane resistance. Secondly, water molecules adsorb to the membrane and pore surface, restricting the available effective pore diameter. With increasing the temperature the amount of adsorbed water molecules is reduced. Thus the effective pore size expands and the permeate flux rises. Finally, the energy barrier generated by the pore wall friction can be overcome more easily due to an increased thermal energy of the water molecules. Also Goulas *et al.* [209] and Schmidt *et al.* [63] transferred these effects to their observation during nanofiltration of sugar molecules.

Figure 4.17 completes the data described above with the dependencies of the rejection R_i, the fractionation purity ΔR_i and the quotient of the flux QJ_S from temperature T and pressure changes Δp_{TM}. The constant values are 35 °C and 10 bar when screening the respective other. Further temperature and transmembrane pressure settings are shown in Figure A.14 and Figure A.15. R_{NADA} remains constant around 100 % rejection with both, increasing T (see Figure 4.17a) and Δp_{TM} (see Figure 4.17b). Regarding the impurities, same is true for the protein content. The rejection is not as effective as for γ-NADA, however still a rejection of 80 % is measured. In contrast, R_{NaCl} decreases slightly with increasing T and increases from 0.3 to 0.6 with increasing Δp_{TM} from 5 to 40 bar. Different transport mechanism might be the reason for the divergent dependencies - convective transport is reported to be dependent on Δp_{TM}, while diffusive transport is independent of Δp_{TM} [209, 213]. Further, Roy & Warsinger [65] show in a model an decreased R_{NaCl} with increasing temperature and explains it with changes in the membrane structure, and the solvent behavior. The lower R_{NaCl} and $R_{Protein}$ and the higher R_{NADA}, the more effective is the desalting and purification of γ-NADA in the nanofiltration process. This effect is further illustrated with the fractionation purity ΔR_i in Figure 4.17c and Figure 4.17d, which is defined in Equation 4.3.

$$\Delta R_i = R_{NADA} - R_{Impurity} \quad [-] \quad (4.3)$$

ΔR_i is higher for NaCl than for the protein impurities over the whole temperature range, meaning a better separation of the salt from γ-NADA in the nanofiltration process. This agrees with the high permeation of NaCl in contrast to the respective lower protein permeation, already discussed in the screening in subsection 4.3.1 and the *NF* step in the cascade process in subsection 4.3.2. As already seen in Figure 4.17a, R_i does not differ much with increasing temperature, thus also ΔR_i is hardly affected (see Figure 4.17c). Same constant behaviour is seen for $\Delta R_{Protein}$ with varying Δp_{TM}. However with increasing Δp_{TM} to a

maximum of 40 bar, ΔR_{NaCl} is reduced by one third (see Figure 4.17d), originating from the effect of Δp_{TM} on R_{NaCl} discussed above.

The fractionation efficiency QJ_i unites statements about both, quality and efficiency of the process, since the permeability of the respective compound as well as the permeate flux are considered, respectively (see Equation 4.4).

$$QJ_i = \frac{J_i}{J_{NADA}} \quad [-] \quad (4.4)$$

In Figure 4.17e and Figure 4.17f the effect of temperature T and pressure Δp_{TM} on QJ_i are show, respectively. While QJ_i of both, protein and NaCl impurities, constantly decreases with increasing T, it has a local optimum at 10 bar when considering Δp_{TM}. Same is true for QJ_i at 25 °C, however at 45 °C, the maximum shifts to higher Δp_{TM} (compare Figure A.15a and Figure A.15b). Further, Figure A.14 shows a flattening of the temperature dependency with increasing Δp_{TM}.

As is it also described in Schmidt *et al.* [63] it is hard to define an optimum since increased temperature and pressure positively affect the process efficiency (Figure 4.16a and Figure 4.16b) but reduce the separation between the target γ-NADA and the impurities NaCl and proteins (see Figure 4.17). The best permeate flux is achieved with the highest T and the highest Δp_{TM}; in contrast the best purification and desalting of γ-NADA were achieved at low pressure conditions and at a room temperature of 25 °C. Since one of the major drawback in the cascade process in subsection 4.3.2 was the γ-NADA yield of the *NF* step probably due to fouling at the end of the process, a suggestion for a better process would focus on an reduction of fouling and increased separation of the feed components. Fouling is reduced with lower Δp_{TM}, which would perfectly match with the better separation of γ-NADA and contaminants. Since it was shown, that T did not have a very decisive impact on the rejection R_i and the fractionation purity ΔR_i, this parameter could be increased to have the positive effect in Q_P.

Nevertheless, the cascade process in subsection 4.3.2 resulted in a final γ-NADA concentration of 15.8±1.0 g L^{-1}. In the following section section 4.4, the crystallization of γ-NADA will be discussed. Here, conditions are examined model solutions, yet, crystallization is also applied downstream of the performed filtration cascade to obtain γ-NADA with a high purity.

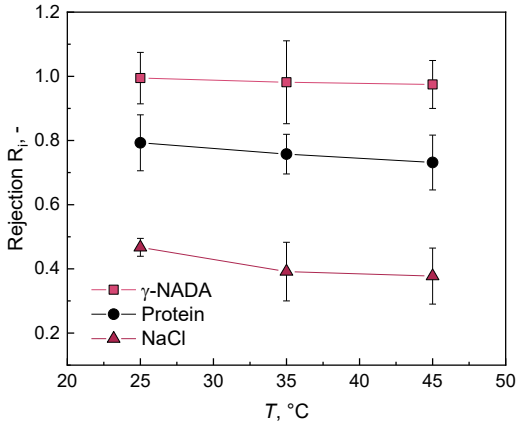

(a) Temperature dependent rejection.

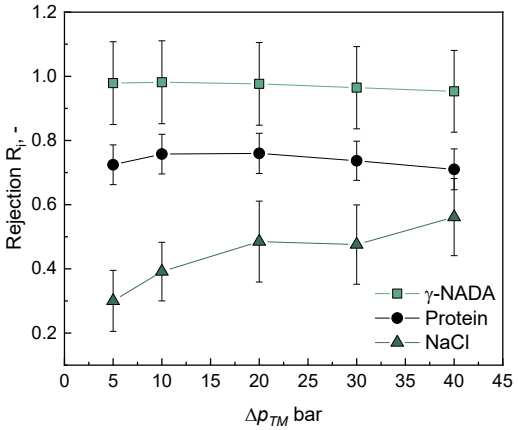

(b) Pressure dependent rejection.

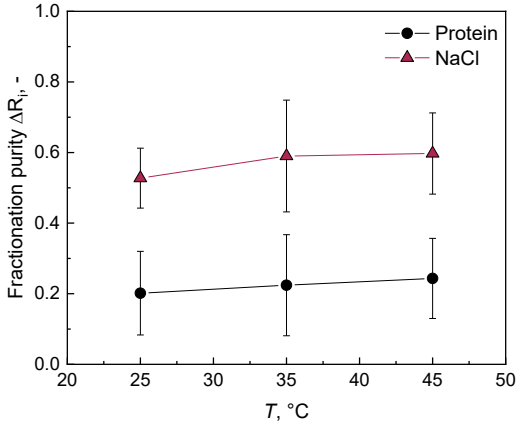

(c) Temperature dependent fractionation purity.

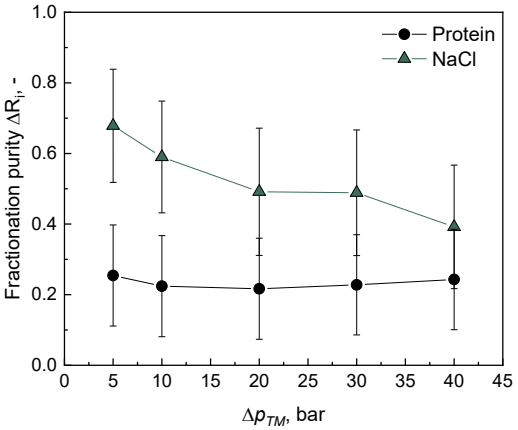

(d) Pressure dependent fractionation purity.

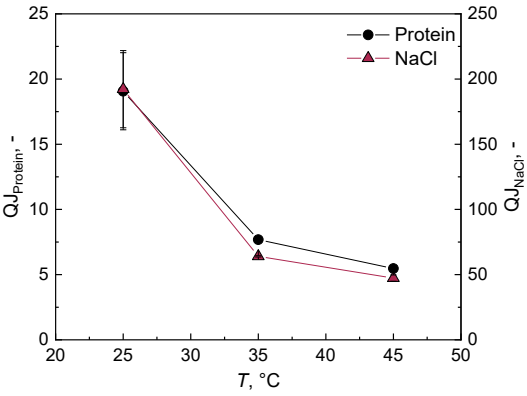

(e) Temperature dependent permeate flux quotient.

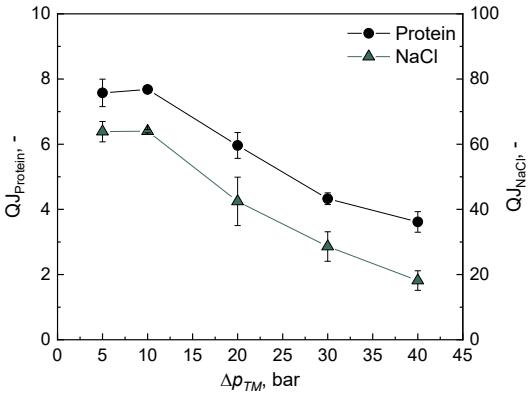

(f) Pressure dependent permeate flux quotient.

Figure 4.17: Impact of the temperature T and the transmembrane pressure Δp_{TM} on the rejection R_i of γ-NADA, proteins and NaCl, the fractionation purity ΔR_i and the ratio of the permeate fluxes of NADA and the impurities - protein and NaCl. The respective constant values were set to $\Delta p_{TM} = 10$ bar and $T = 35$ °C. The nanofiltration membrane *Desal/GE DL* was used with a feed flow rate of 10 L h^{-1}. Results of the remaining setups are shown in Figure A.15 and Figure A.14 for constant pressure and constant temperature, respectively.

4.4 Crystallization of Nγ-acetyl-L-2,4-diaminobutyric acid

4.4.1 Solvent identification

The choice of the right solvent in which crystallization of the respective substance should take place is crucial for cooling and antisolvent crystallization. As in detail described in subsection 2.4.1, both crystallization methods require a solvent in which firstly, crystallization of the respective substance can in general take place and secondly, fits to the process conditions to promise a high target purity and yield.

The first step is the identification of the solvent or solvent pair for cooling and antisolvent crystallization, respectively. Hosokawa *et al.* [122] name a list of 15 solvents, commonly used for the crystallization of small molecules such as γ-NADA. First of all, to narrow the experimental effort, a model-based pre-screening was performed to examine the solubility of γ-NADA in the respective solvents in a temperature range up to 80 °C (see Figure 4.18a). On the basis of quantum chemical calculations, the here used Conductor-like Screening Model for Real Solvents (*COSMO-RS*) [214–216] simulates the thermodynamic characteristics of the used solvents and the target species γ–NADA. Also the maximum solubility in solvent mixtures of water with either acetonitrile, methanol (*MeOH*), ethanol (*EtOH*) or propanol at 25 °C was simulated (see Figure 4.18b).

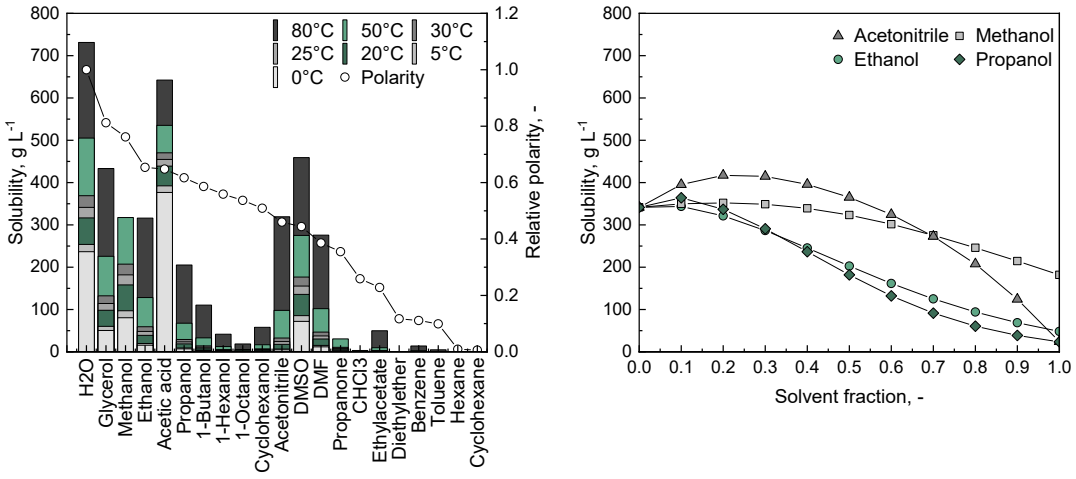

(a) Temperature dependent solubility. **(b)** Solubility in solvent mixtures at 25°C.

Figure 4.18: Temperature dependent (a) and solvent concentration dependent (b) solubility of NADA in different solvents, simulated with *COSMO-RS*.

Figure 4.18a shows the solubility of γ-NADA, obtained with the *COSMO-RS* modeling [215–217], for the examined solvents and temperatures, arranged with decreasing relative polarity. Firstly, a temperature dependence of the solubility of γ–NADA in the different solvents is visible, however differently pronounced. Secondly, the solvents with the highest relative polarity, water, glycerol, *MeOH*, *EtOH* and acidic acid, are among the solvents with the best solubility for γ-NADA. However, acetonitrile (*ACN*), dimethyl sulfoxide (*DMSO*) and dimethylformamid (*DMF*), solvents with only a moderate relative polarity, show a even higher solubilisation potential than *MeOH* and *EtOH*. In hexane and cyclohexan, the less polar solvents, γ-NADA is nearly insoluble. In the simulation, the polarity of the solvent appears to have an impact on the solubility, however does not allow a clear assignment and prediction.
In antisolvent crystallization, the target molecule, which is dissolved in a appropriate solvents, is solidified by adding a second solvent (antisolvent) with very poor solubility for the molecule but a good miscibility with the first solvent [218]. Figure 4.18b shows the simulative results of the solubility of γ-NADA in step-wise solvent fractions of *ACN*, *MeOH*, *EtOH* and propanol. Since the solubility of γ-NADA in the pure solvents (see Figure 4.18a) was poor at 25 °C, the decrease with increasing solvent fraction was expected. Adding *EtOH* and propanol show a sigmoidal effect on the solubility with increasing fraction, while adding *ACN* results first in a rise and then, at approximately 0.3, in a steep fall. Increasing the methanol concentration has the lowest effect on the solubility, with *MeOH*, being the solvent of the four tested with the comparatively highest solubility of γ-NADA.

The simulative pre-screening was performed to pre-select the most promising solvents and thus, narrow the experimental effort. The solubility of γ-NADA was experimentally studied in the solvents showing the best solubility in the *COSMO-RS* simulative screening (see Figure 4.18a): water, *MeOH*, *EtOH* and acetic acid. Glycerol was excluded, since the high viscosity limits good processing and purification. Since in the process, γ–NADA is biotechnological produced with *H. elongata* ΔectC in high saline medium (see section 4.2), the solubility was also examined in 1 M NaCl. The solubility of γ–NADA in aqueous solvent mixtures is in detail described later in subsection 4.4.3.

Figure 4.19 shows the temperature–dependent solubility of γ–NADA in the tested solvents. In water, 1 M NaCl and *EtOH* the solubility rises with increasing temperature. In *MeOH* the solubility decreases with increasing temperature, while in acetic acid, the solubility remains temperature-independent. In pure *ACN*, γ–NADA was not soluble at all, independent of the applied temperature. In general, the solubility of most substances increases with increasing temperature. This results from the definition of the enthalpy of solution. If the dissolution reaction has a positive Gibbs free energy, is endothermic, the solubility increases with increasing temperature and vice versa. Romero & Oviedo [219] present a comparable solubility

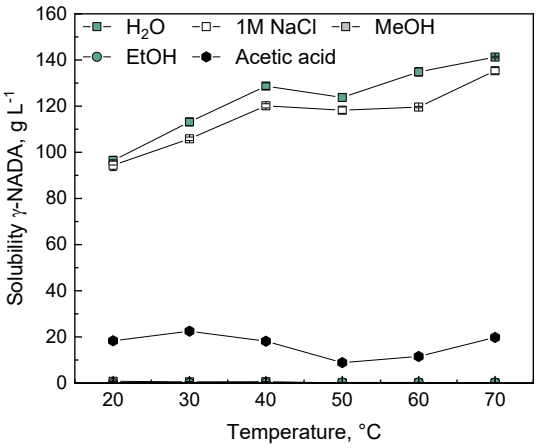

Figure 4.19: Experimentally determined temperature–dependent solubility of γ–NADA in different solvents. γ–NADA was dissolved over night at the respective temperature condition to saturation.

behavior for an γ–aminobutyric acid in water with increasing temperature. Comparing the solubility results from the *COSMO-RS* model and the experimentally measured ones, the trend in general agrees - the solubility is highest in water and reduced in solvents like *EtOH* and *MeOH*. Yet, the solubility data in the simulation were largely overestimated (see Figure 4.18a and Figure 4.19). A high solubility of compatible solutes in H_2O is characteristic for this molecule class [132]. However, compared with related molecules, the solubility of γ–NADA in water is comparatively low - 96.4±1.9 g L^{-1} at 20 °C. Held *et al.* [220] describes a significant higher solubility of ectoine and hydroxyectoine with 6.5 M and 7.2 M at 25 °C, respectively. Yet, as can be seen in Table 4.1 in subsection 4.2.2, the maximum solubility exceeds the required solute concentration for the cultivation and growth in 0.5 M NaCl and 1.0 M NaCl by a multiple, not limiting the application of the *H. elongata* strain. The effect of temperature on the solubility of γ–NADA is especially high in *EtOH*. Here the theoretical yield when performing cooling crystallization from 50 °C to 20 °C is approximately 81 %, while using H_2O as crystallization solvent the yield is 22 %. However, H_2O tends to be the more appropriate solvent for the cooling crystallization of γ–NADA, since the whole biotechnological production and purification is performed in aqueous conditions (see section 4.2 and section 4.3). Further, the amount of required solvent is reduced with higher solubility and, in more or less all DSP steps, a higher initial start concentration results in a better process yield. Also for ectoine different crystallization processes are described. Onraedt *et al.* [221] shows the crystallization of ectoine in *EtOH* after concentrating and drying, while in Sauer & Galinski [26] the crystallization is performed in H_2O right after a chromatography step. In the industrial production of ectoine, crystallization is used as final purification step [2].

Comparing the solubility results from the *COSMO-RS* model and the experimentally measured ones, the trend in general agrees - the solubility is highest in water and reduced in solvents like *EtOH* and *MeOH*. Yet, the solubility data in the simulation were largely overestimated: for example 505.3 g L^{-1} in H_2O at 50 °C compared to 129.4±0.5 g L^{-1} at the same conditions in the experiment (see Figure 4.18a and Figure 4.19). For carboxylic acids Schröder *et al.* [222] describes an overestimation with *COSMO-RS* as well, yet less pronounced. In the experiments, γ–NADA was not soluble in *ACN* and less soluble in *MeOH* than in *EtOH*, which not coincides with the model data. Discrepancies might originate from several factors: the calculation requires the input of the compound structure, which might not be accurate enough to simulate the solubility of the zwitterionic character of γ–NADA. Further, the thermodynamic changes of the solvent behavior due to temperature changes influence the theoretical calculation more dominant than in experiments. Thirdly, for the calculation the hydrolyzed ectoine material (see Table 3.13) was used, which does not only consists of γ–NADA, but also of impurities. Thus, solubility of pure γ–NADA might be slightly higher; however checking the solubility with impurities illustrates better the process conditions. Nevertheless, the *COSMO-RS* simulation model clearly gave an idea which solvents might be suitable for the crystallization of γ–NADA, yet for detail investigations the experimental determination of the solubility was crucial. An alternative to *COSMO-RS* simulation might be *PC-SAFT* which was for example used by Ruether & Sadowski [223] to model the solubility of standard drugs in solvents and respective mixtures. Also Held *et al.* [220] used this method to determine the solubility of ectoine and hydroxyectoine in water.

Of all tested solvents, H_2O was chosen as most suitable solvent for the cooling crystallization of γ–NADA. Firstly, H_2O is cheap, easily accessible, environmentally harmless and thus, easily disposable. Secondly, the concentration of γ–NADA in H_2O is temperature dependent; the key aspect for using the solvent in cooling crystallization. Cooling a saturated solution from 50 °C to 20 °C would result in a theoretical yield of 25.5±1.5 %, according to the solubility results in Figure 4.19. Thirdly, the biotechnological production of γ–NADA is performed in aqueous environment. As shown in Figure 4.19, the effect of 1 M NaCl on the maximum solubility of γ–NADA is negligible. Further, processing of the intracellular target with cell separation, disruption (see subsection 4.2.3) and filtration (seesubsection 4.3.2) reduced the NaCl concentration after *NF* to 0.2 M (see Table 4.3). Thus, H_2O represents the process conditions very well and can be used in the following, ideal crystallization experiments to develop a potent crystallization process for γ–NADA.

4.4.2 Cooling Crystallization

In the previous screening, discussed in subsection 4.4.1, H_2O was identified as suitable solvent for the cooling crystallization. To demonstrate not only the ability of γ–NADA to crystallize, but also to show a simultaneous purification, hydrolyzed ectoine material, kindly provided by *bitop* AG (see Table 3.13), was used as substrate and saturated model solution. As described in [224], this material consists of 49.2±2.5 wt% γ–NADA, 17.5±4.5 wt% α–NADA, 2.6±0.2 wt% ectoine and 30.8±1.1 wt% NaCl. Unless otherwise described, the hydrolyzed material was dissolved at 50 °C overnight to maximum saturation in H_2O. Supernatant was subsequently cooled down to 20 °C under stirring conditions of 300 rpm to crystallize the desired target γ–NADA.

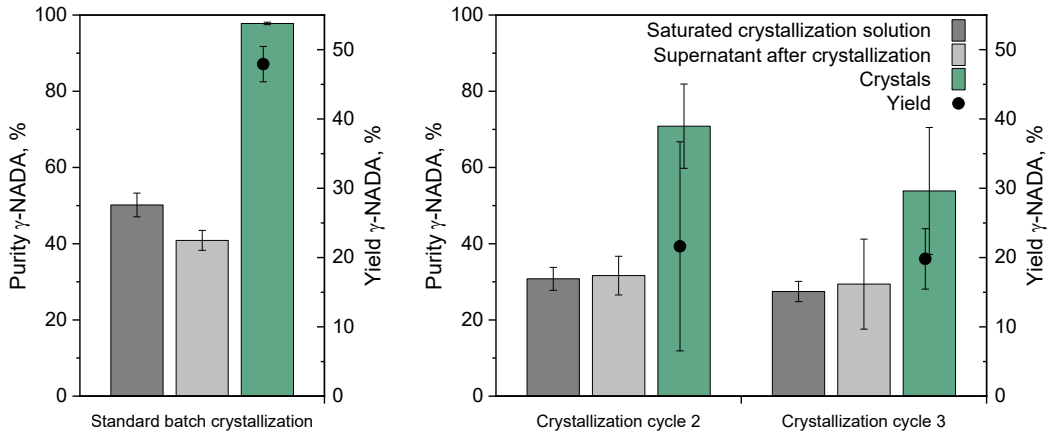

(a) Standard batch cooling crystallization.

(b) Cooling crystallization with recycled, saturated crystallization solution.

Figure 4.20: Cooling crystallization of γ–NADA in H_2O. Saturated solution was cooled down from 50 °C to 20 °C at a constant impeller speed of 300 rpm. For standard batch cooling crystallization (a) hydrolyzed ectoine material was saturated over night in H_2O. During recycled batch cooling crystallization (b) remaining supernatant after crystallization was resaturated with hydrolyzed ectoine material over night.

As shown in Figure 4.20a, the saturated solution of hydrolyzed ectoine material at 50 °C in the standard batch cooling crystallization consist of 50.2±3.1 % γ–NADA which corresponds to a concentration of 118.2±4.1 g L^{-1}. NaCl, with a concentration of 1.2±0.1 M made up the majority of the impurities and matching the cultivation condition described in section 4.2. Since the solubility of γ–NADA noticeably decreases with decreasing temperature (see Figure 4.19 in subsection 4.4.1) the dissolved fraction of the target molecule in the supernatant is reduced to 40.9±2.6 % when cooling down the solution to 20 °C and let crystallization occur for 21 h. The obtained γ–NADA crystals had a purity of 97.8±0.32 % and the yield of the cooling crystallization step was calculated to 47.9±2.56 %. As described in Martin *et al.*

[100], the obtained γ–NADA crystals from a standard batch cooling crystallization result in a needle- to rod shape and are shown in Figure 4.21a. They occur relatively uniform in length and thickness and do not cluster.
The above described yield mainly results from the temperature dependent solubility behavior of the target, however several methods can be applied to increase the overall process yield: cooling to lower temperature, seeding and a continuous setup. A continuous process was tested with successively performed batch cooling crystallization steps, while resaturating the recycled supernatant from the upstream crystallization with hydrolyzed ectoine material. As in the first crystallization step (Figure 4.20a) mainly γ–NADA crystallized, the resaturation of the remaining supernatant resulted in a reduced amount of γ–NADA in the saturated crystallization solution of crystallization cycle 2 (see Figure 4.20b). The vacant solvent molecules dissolve the provided substrate with the same distribution as in the first saturation step. Since, the supernatant after crystallization is already enriched with impurities, the total percentage amount of γ–NADA decreases. The saturated solution consist of 30.8±3.0 % γ–NADA at a concentration of 88.0±4.1 g L^{-1}. The crystallization step did not significantly reduce the amount of γ–NADA in the supernatant and also the resaturation for the third crystallization cycle did not change the percentage of the molecule in solution. The yield was decreased to 21.6±15.1 % and 19.8±4.4 % in crystallization cycle 2 and 3, respectively. Yet, the decrease in purity makes it clear that the obtained crystals consist more and more of impurities, mainly NaCl (24.8±20.1 % and 41.3±4.6 % in cycle 2 and 3, respectively). Darmali *et al.* [225] reviews the impact of low and high impurity content in the crystal purity in continuous systems. In conclusion, the cooling crystallization of γ–NADA from a saturated model solution containing hydrolyzed ectoine material in H_2O worked very well. After only one process step, γ–NADA was 97.8±0.32 % pure. Here, the NaCl conditions (1.2±0.1 M) were even higher than in the cultivation (see section 4.2) or after processing in the upstream filtration (see section 4.3). Enriching the recycled supernatant with new substrate and again performing a cooling crystallization significantly reduced both, yield and purity of the obtained crystals. This means for the process a continuous crystallization is feasible, yet with some drawbacks, especially regarding yield and purity. If the process stream after filtration already has a good purity, several continuous crystallization cycles could be presumably performed without sacrificing yield and purity.

Impurities in general did not disturb the batch crystallization of γ–NADA. As it is shown in Figure 4.21b, crystals of γ–NADA are formed even in complex fermentation supernatant after separation of the cells (see subsection 4.2.2), enriched with hydrolyzed ectoine material. The crystals occur in the same needle to rod shape as in Figure 4.21a, however smaller in size. Amongst other, the nucleation rate in general is dependent on the impurity content [226], as it is for example shown by Rauls *et al.* [227]. Here, the nucleation rate increases when the impurity content exceeds a certain level, thus more but smaller crystals occur. The

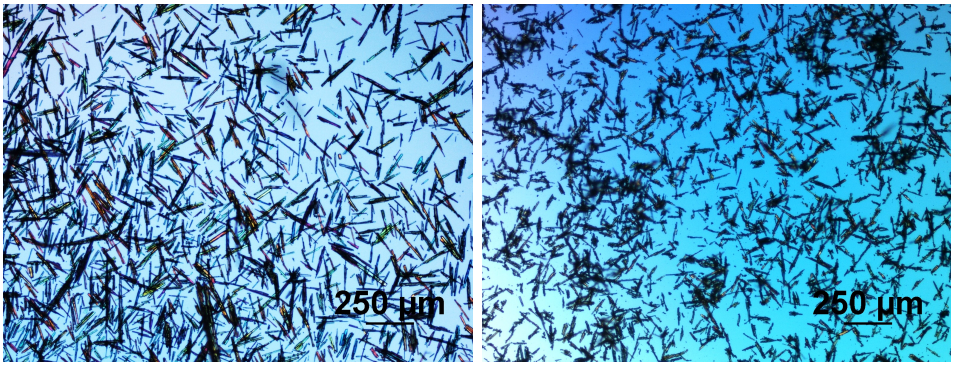

(a) Cooling crystallization of γ–NADA in H_2O. **(b)** Cooling crystallization of γ–NADA in fermentation supernatant.

Figure 4.21: γ–NADA crystals from cooling crystallization in H_2O (a) and fermentation supernatant after cell separation, described in subsection 4.2.2 (b). Saturated hydrolyzed ectoine material was cooled down from 50 to 20 °C at 300 rpm stirring in a mL-reactor system.

obtained yield remains comparable to the crystallization in H_2O, yet it is difficult to make a clear statement about the purity. HPLC analysis show some signals at 280 nm, indicating protein or DNA inclusion in or deposits on the crystals. The smaller crystals and with this the denser solid content complicates the washing step, thus, the organic impurity content in the crystals might originate from the poorer washing conditions. The effect of impurities on the species involved in crystallization and the crystallization itself is diverse: changes in solubility and supersaturation conditions [227, 228], variation of solvent characteristics, influencing nucleation [228, 229], crystal growth rates [230] and support side specific growth and with this varied product morphology, polymorphism [231, 232] and crystal size [227].

A widely used method to achieve both, a faster and also a more effective crystallization of the target molecule. Figure 4.22 shows the kinetics of the cooling crystallization process of γ–NADA, with different amount of seeding material. Erdemir *et al.* [92] recommends 0.1 - 1.0 % seed amount as seed slurry to prevent oiling-out and best control nucleation, yet examples of more than 10 % seeding amount are reported [233]. As can be seen in Figure 4.22, the seeding content was tested in the recommended range, however seeds were added in dry form. The positive effect of the seeding crystals on the kinetics of the crystallization process is obvious. The steep decline of supernatant concentration maps the crystallization of γ–NADA. This decrease occur much faster, the more seeds are used. As can be seen in Figure 4.21 and is reported in Martin *et al.* [100], γ–NADA crystallizes in needle-shape. Here, the growth relevant surface of the crystals (tips of the needles) is low, thus more seeding material is in general required [234]. Yet, especially the kinetic of the crystallization without any seeding material stands out, since the begin of crystallization is shifted to much higher process times.

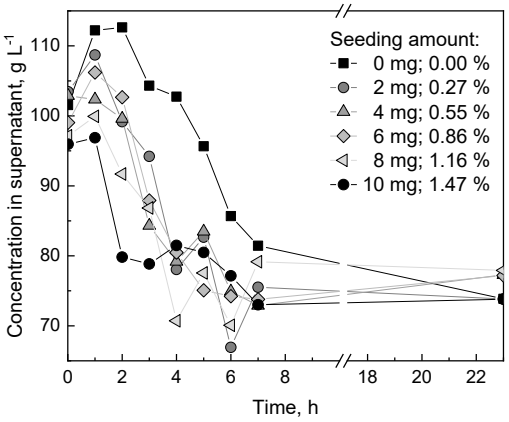

Figure 4.22: Kinetic of the cooling crystallization process of γ–NADA in H_2O represented by the supernatant concentration over the process time. Seeding material consisting of γ–NADA crystals was used in different amount. Saturated solution was cooled down from 50 to 20 °C and 300 rpm stirring.

Crystallization is in general hard to control. This is reflected in the data, since from approx. 4 h, supernatant concentration occurs bumpy and data from different seeding amount merges. After 7 h, the equilibrium concentration is reached under mainly every seeding condition, meaning the end of the crystallization process. Only the crystallization without seeding material clearly requires longer process times, in this case over night. Decision on a seeding condition might be a trade-off between control of the crystallization process, efficiency and amount of probably expensive seeding material. Yet, the needle-shaped crystals of γ–NADA in general require more seeding amount [234] and the experiment in Figure 4.22 shows the fastes crystallization with the highest seeding content of 1.47 %, seeding in this range is recommended for the cooling crystallization of γ–NADA.

In general, triggering the kinetic of the crystallization is crucial since longer process times limit the efficiency of the process. In a lab-scale reactor system (*OptiMax 1001 Synthesis workstation, Mettler Toledo Inc*) the effect of varied cooling rates (Figure 4.23a) and varied impeller speed (mixing conditions, Figure 4.23b) on the crystallization kinetic were tested. The focused beam reflectance measurement (*FBMR*) probe (*Mettler Toledo Inc.*) tracks the particle formation in the crystallization process. Additionally, performing cooling crystallization of γ–NADA in a 500 mL reactor, validates the general scale-up ability of the crystallization process.

Figure 4.23 shows the tracked crystallization of γ–NADA in the reactor scale. As shown in Figure 4.23a the cooling rate might affect the kinetic of γ–NADA crystallization, however no clear statement can be made about an existing trend. While with a cooling rate of 10 K min^{-1} the visible crystallization starts after approximately 2 h, the longest initiating time is observed

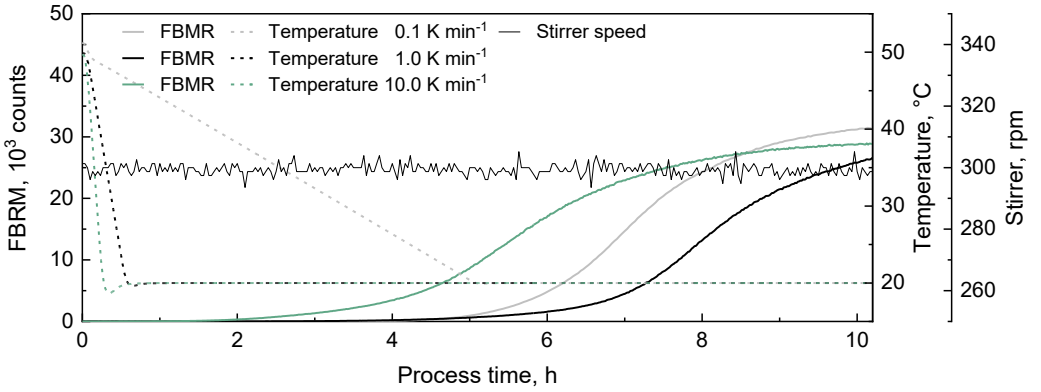

(a) Variation of cooling rates.

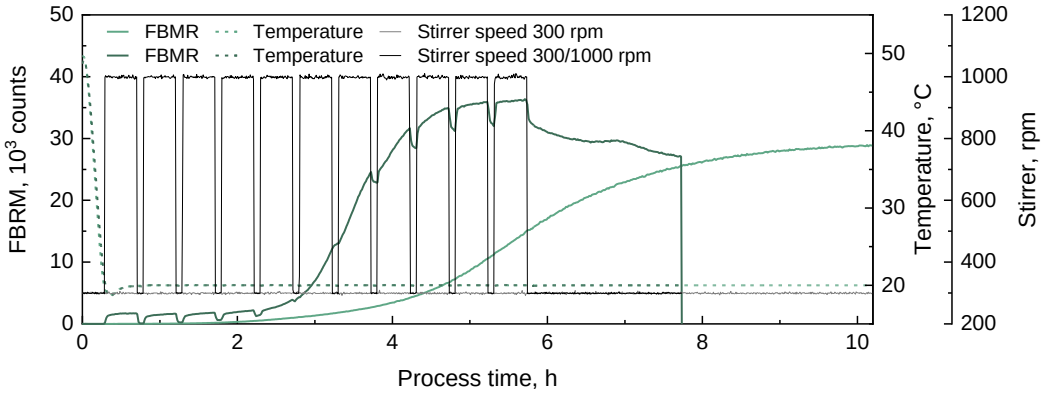

(b) Variation of impeller speed.

Figure 4.23: Cooling crystallization of γ–NADA in H_2O in 500 mL reactor system (*OptiMax 1001 Synthesis workstation, Mettler Toledo Inc*). Saturated solution was cooled down from 50 °C to 20 °C with different cooling rates at a constant impeller speed of 300 rpm (a) and with different varying impeller speed and constant cooling rate of 10 K min^{-1} (b).

with a cooling rate of 1 K min^{-1}, approximately 5 h. When cooling the solution down with 0.1 K min^{-1}, the crystallization starts in between. As already discussed above, control of a crystallization could be challenging. This becomes clear with the time range of several hours in which the γ–NADA crystallization starts in Figure 4.23a. As no clear trend is visible, it could be assumed that the cooling rate does not affect the γ–NADA cooling crystallization, yet the effect results more from less control of the nucleation in the reactor. Further, it is more likely, that cooling rates affect the morphology of the product, however not discussed in detail here. Yet, shown in Figure A.16, the observed morphology of the crystals do not change with different cooling rates. In contrast, changing the impeller speed operation from a constant speed of 300 rpm to an alternating sequence of 1000 rpm to 300 rpm significantly shifts the crystallization start (defined by an increase of the FBMR counts) to a earlier process time (see

Figure 4.23b). As mixing is intensified with a faster impeller speed, shear forces increase and with this present crystals were crushed. Thus, available surface for ongoing crystallization increases. Further, the nucleation rate could be triggered due to a changed mixing intensity profile [234]. Comparing the cooling crystallization in the reactor in Figure 4.23 with the small scale cooling crystallization shown in Figure 4.22 a comparable crystallization process is observed. Not only do the kinetic of the unseeded small scale crystallization process in Figure 4.22 is comparable to the up-scaled version with 10 K min^{-1} (Figure 4.23a, but the needle-shaped crystal morphology, shown in Figure A.16 are also similar (see Figure 4.21). Thus, a scale-up of the cooling crystallization process of γ–NADA is feasible. A better control of the system can definitely achieved with for example seeding. The alternating changes in stirring speed can further increase efficiency of the process, however attention should be paid to the final size of the crystals. This affects downstream process steps, however needle-shaped crystals in general have the drawback of being a more difficult initial situation for e.g. washing and filtration [234].

4.4.3 Solvent Crystallization

As shown in Figure 4.19 the required concentration of γ-NADA to perform cooling crystallization in aqueous solutions is very high compared to the reachable concentration of 15.8 ± 1.0 g L^{-1} after *NF* filtration (see Table 4.4 in subsection 4.3.2). The required saturated concentration at 50 °C is 123.7 ± 1.7 g L^{-1} for cooling crystallization in H_2O. This means a 7.8 fold higher concentration after *NF* as was reached, which is hardly possible with the used filtration set-up. Thus, also antisolvent crystallization was examined, which is advantageous regarding the mandatory concentration after *NF* and further can be performed at room temperature meaning no additional energy input.

Antisolvent crystallization in model solutions

As it was discussed in subsection 4.4.1, the pure solvents ethanol (*EtOH*) and methanol (*MeOH*) showed a very poor solubility for γ–NADA in both, simulation (Figure 4.18a) and experiments (Figure 4.19). Assuming that γ–NADA is in general very low soluble in polar solvent, a third potential antisolvent isopropanol (*2-propanol*) was included in the examination of the antisolvent crystallization. Figure 4.24 shows the maximum solubility of γ-NADA in increasing fractions of the antisolvents *EtOH* (Figure 4.24a), *MeOH* (Figure 4.24b) and *2-propanol* (Figure 4.24c) at 25 °C. Further the supernatant concentration when batch-wise increasing the amount of solvent is shown for each solvent fraction, starting with

a saturated γ-NADA concentration in H_2O at 25 °C. The supersaturation according to Equation 2.13 is shown over the solvent fraction.

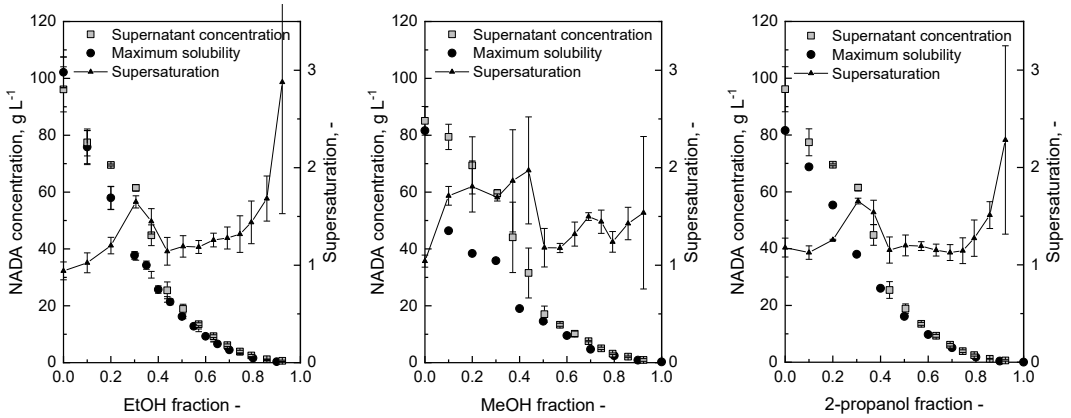

(a) Ethanol. **(b)** Methanol. **(c)** 2-propanol.

Figure 4.24: Maximum solubility, supernatant concentration after step-wise increasing the solvent fraction and nascent supersaturation of γ-NADA at 25 °C in different solvent concentration using *EtOH* (a), *MeOH* (b) and 2-propanol (c). Maximum solubility was fitted with a cubic spline fit (1000 iteration) to calculate supersaturation.

The maximum solubility of γ-NADA decreases with increasing solvent fraction, valid for all tested solvents. Here, a steep drop of solubility is observed at lower solvent concentration, while the effect weakens with increasing solvent amount. In contrast, the supernatant concentration when step-wise raising the solvent fraction follows a more sigmoidal behavior. Thus, in a solvent concentration range from around 0.1 to 0.4, the supernatant concentration exceeds the maximum solubility of the respective fraction. Here, a supersaturation greater than 1 is generated and thus, nucleation and further crystallization can occur. This behavior is important since the addition of antisolvent alone dilutes the saturated solution, thus the maximum solubility of the component in solution should fall below the dilution concentration to initiate a stable nucleation [235]. The behavior of γ-NADA in the solvents *EtOH* and *2-propanol* and the respective aqueous mixtures is very similar (compare Figure 4.24a and Figure 4.24c). Here, the growing challenge of process control with increasing solvent fraction becomes visible by the magnifying error deviation in the supersaturation. The behavior of the target in the *MeOH* system generally occurs less controllable (Figure 4.24b). Standard deviation of both, supernatant concentration when stepwise adding *MeOH* and the supersaturation are high. This might result from the solvent handling, however a less controllable system complicates the whole process. Yet, crystallization of γ–NADA is proofed in all examined solvents by the occurring solid material. The resulting crystals, shown exemplarily for *EtOH* in Figure 4.25, have a needle-shaped appearance and look more branched with increasing *EtOH* concentration (compare Figure 4.25a and Figure 4.25b). The same shape is

also described for the cooling crystallization of γ–NADA in subsection 4.4.2 and in Martin *et al.* [100], yet the branched morphology might indicated polymorphism with increasing solvent concentration (twinning reviewed in [99, 236, 237].

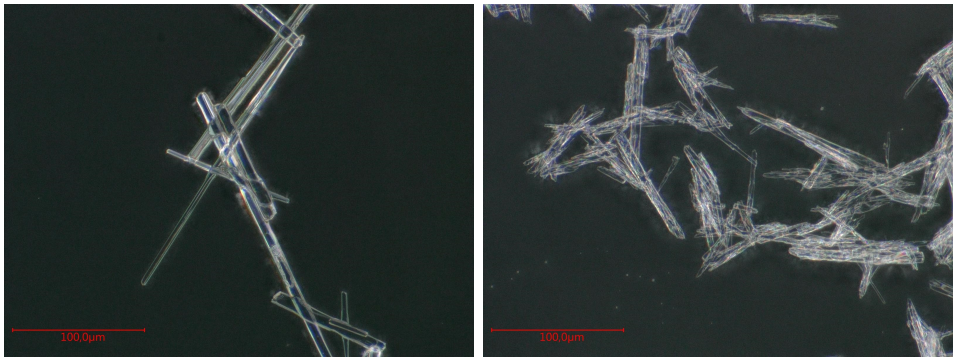

(a) *EtOH* fraction of 0.4. **(b)** *EtOH* fraction of 0.9.

Figure 4.25: Microscope pictures of γ-NADA crystals after *EtOH* anti-solvent crystallization at 40 % (a) and 90 % EtOH concentration (b). 1000x magnification.

As shown in Figure 4.24, supersaturation and crystallization can be performed with the three tested solvents. *EtOH* was chosen as most promising solvent. Firstly, a clear division between the maximum solubility and supernatant concentration is shown (see Figure 4.24a) which enables crystallization. Secondly, *EtOH* is generally available, cheap and less harmful if swallowed. The previous antisolvent crystallization experiments in Figure 4.24 were performed with an initial, maximum saturated γ–NADA solution in H_2O at 25 °C. Yet, after *NF* filtration a concentration of 15.8 ± 1.0 g L^{-1} γ–NADA was obtained (see subsection 4.3.2). Thus, crystallization was performed with *EtOH* as antisolvent and with the undersaturated starting conditions in a comparable range of the process: 15.3±0.2 g L^{-1} γ–NADA and 0.16±0.02 M NaCl.

Figure 4.26 shows the obtained saturation of γ–NADA and NaCl (scatter plot) and the supernatant concentration of the small molecule (line-symbol plot) when step-wise adding *EtOH*. Until an *EtOH* fraction of 0.55 the γ–NADA concentration in the supernatant decreases almost linear with increasing *EtOH* volume just describing the dilution effect. In the same context, the saturation level of γ–NADA remains at the factor 1. At a solvent fraction of 0.6, a drop of the saturation to a saturation of approximately 0.4 along with a drop of the supernatant concentration was observed. With further increasing the *EtOH* volume, the saturation was reduced to 0.14±0.01, meaning a theoretical yield of 86 % at an *EtOH* fraction of 0.9. The saturation of a 0.16 M NaCl solution in H_2O increases slightly with increasing *EtOH* fractions meaning no loss in the supernatant due to solidification. A future idea of the process is an extracellular production of γ–NADA with an *H. elongata* mutant. γ–NADA would be excreted to the surrounding medium with 1 M NaCl. As shown in subsection 4.3.2,

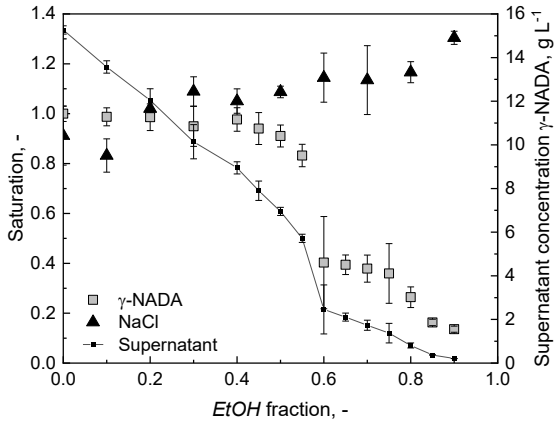

Figure 4.26: Antisolvent crystallization with *EtOH* of γ–NADA and NaCl in H_2O at 25 °C, starting in a concentration range adapted to the process concentration shown in subsection 4.3.2: 15.3±0.1 g L^{-1} γ–NADA and 0.16±0.02 M NaCl. γ–NADA and NaCl crystallization was performed independent of each other.

γ–NADA concentration in the retentate of the *NF* process was concentrated, but the NaCl concentration stays constant. Thus, to prove the applicability of the crystallization process also for the potential future conditions, a starting concentration of 1 M NaCl was validated, resulting in nearly the same solubility behavior as with 0.16 M, however a slight decrease in the saturation at a *EtOH* fractions of 0.9 was observed (see Figure A.17). The results shown in Figure 4.26 clearly demonstrate firstly, the successful implementation of antisolvent crystallization with *EtOH* for the crystallization of γ–NADA from the concentrated solution after *NF* (see subsection 4.3.2). Secondly, the simultaneous purification from the saline environment was shown, since both applied initial NaCl concentration (see Figure 4.26 and Figure A.17) stay in solution with increasing *EtOH*. It should be noted, however, that both, γ–NADA and NaCl experiment were performed independent of each other in H_2O. Solution from the process contain a mixture of both, γ–NADA and NaCl, as well as other organic impurities like small proteins and peptides, which could disturb the crystallization of γ–NADA.

Antisolvent crystallization of γ–NADA from processed *NF* concentrate

The previously validated antisolvent crystallization with *EtOH* was subsequently performed with the *NF* concentrate produced from *H. elongata* ΔectC cultivation (subsection 4.2.3) and downstream filtration (subsection 4.3.2). As can be seen in Figure A.18, neither stepwise adding the solvent (see Figure A.18a and Figure A.18b), nor seeding (Figure A.18c) or changing the antisolvent to *2-propanol* (Figure A.18d) resulted in a successful crystallization

of γ–NADA. In none of the experiments the supernatant concentration of γ–NADA falls below the dilution concentration and thus, stays in solution.

The described process, consisting of the cultivation of *H. elongata* ΔectC in 1 M NaCl and the filtration cascade, was performed a second time to obtain new *NF* concentrate. After cultivation, the *MF* starts with a feed volume of 1.25 L which resulted in 99 mL *NF* concentrate containing 3.15±0.05 g L^{-1} γ–NADA. The reduced concentration compared to the *NF* concentrate in Table 4.4 was caused by the lower volume which was available in this process. Since in *NF*, also protein is retained, here the obtained protein concentration of 0.2±0.1 g L^{-1} is also lower compared to subsection 4.3.2. The NaCl concentration of 0.15±0.03 M is in a comparable range due to the unhindered permeation of NaCl, which was shown in the *NF* process. To start with equivalent concentration conditions the concentrate after *NF* was lyophilized and subsequently adjusted with H_2O to the required concentration range. As already described in subsection 4.3.2 the dead volume of the filtration system *Cube 80VA* is high for the concentrate loop. Thus, the same above described procedure to adjust the concentration was performed for *recycled concentrate*. Here, the recycled solution contains 4.47±0.05 g L^{-1} γ–NADA and 2.26±0.35 g L^{-1} protein. NaCl was not quantified, however, as shown in subsection 4.3.2, NaCl concentration does not change significantly over the process. Thus, same amount as in the concentrate can be assumed.

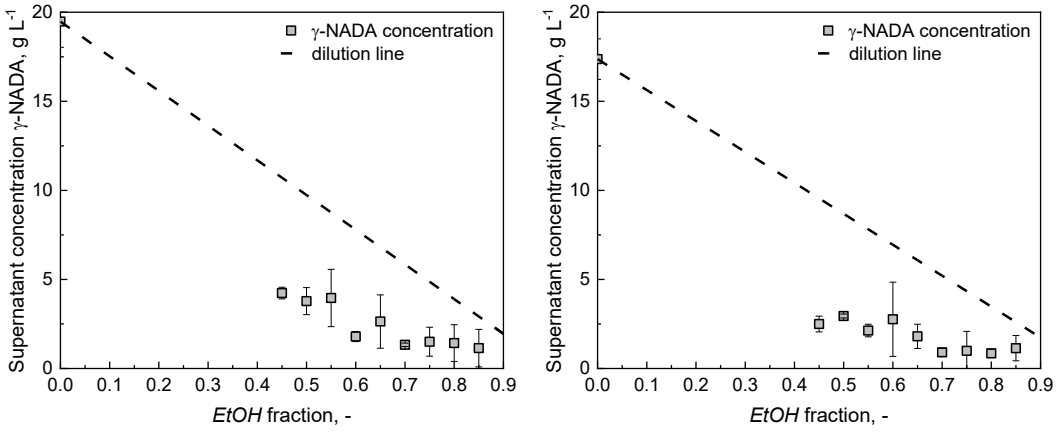

(a) Concentrate. **(b)** Recycled concentrate.

Figure 4.27: Triplicates of antisolvent crystallization of γ–NADA after *NF* at 25 °C, described in subsection 4.3.2. *EtOH* was used as antisolvent with an initial 45 % solvent step to exclude organic impurities and further step-wise increasing the *EtOH* concentration to maximum of 0.85.

Figure 4.27a shows the antisolvent crystallization of γ–NADA from the adjusted *NF* concentrate. The initial solvent step to an *EtOH* fraction of 0.45 already reduces the γ–NADA concentration below the dilution line, indication a successful crystallization. At the highest

EtOH percentage, 1.14±1.05 g L^{-1} remain in the solution and resulting in a theoretical yield of 60.8±36.1 %. The remaining γ–NADA concentration is in very good agreement with the solubility data shown in Figure 4.24a; 1.19±0.11 g L^{-1} stay in the supernatant when step-wise adding the antisolvent to the pure γ–NADA solution. Similar behavior was observed with the recycled *NF* concentrate, shown in Figure 4.27b. At a *EtOH* fraction of 0.85 a slightly reduced, theoretical yield of 52.2±27.3 % was achieved.
Downstream of the antisolvent crystallization, a cooling crystallization of the solution containing an *EtOH* fraction of 0.85 was performed. Starting from 25 °C, the solution was cooled down to 4 °C and stirred over night. In Table 4.5 amount of obtained γ–NADA crystals is shown.

Table 4.5: Comparison of obtained amount of γ–NADA crystals from antisolvent and cooling crystallization in *NF* concentrate. Theoretical mass refers to the calculated amount of γ–NADA in the supernatant at the *EtOH* fraction of 0.45 and 0.85 to described the theoretical yielded mass of γ–NADA crystals. * theoretical yielded mass of concentrate 1 was excluded from calculation

Sample	**Weight crystals** [mg]	**Yield** [%]	**Yield related to 0.45 *EtOH*** [%]	**Purity** [%]	**Theoretical yielded mass γ–NADA after antisolvent crystallization**
Concentrate 1	27.29	29.4	72.79	89.6	-35.72
Concentrate 2	27.99	29.4	68.85	98.6	22.71
Concentrate 3	12.31	12.9	35.37	95.1	19.56
Total	22.53±8.86	23.9±9.5	59.01±20.56	94.4±4.6	21.23±2.23*

After cooling crystallization an average of 22.53±8.86 mg γ–NADA crystals was obtained in the three experiments. Regarding the theoretical yielded mass of γ–NADA, which is calculated from the amount of γ–NADA in the supernatant at an *EtOH* fraction of 0.85 and 0.45, 21.23±2.23 mg could be obtained directly after antisolvent crystallization. Thus, the additional cooling crystallization did not significantly improve the yielded amount of crystals, which was 23.9±9.5 %. Nevertheless, obtained crystals showed a high purity of 94.4±4.6 %, comparable with the purities from crystallization in model solutions in subsection 4.4.2. The reduced yield might results from the set-up of the antisolvent experiment. After the initial step adding *EtOH* to a fraction of 0.45, precipitate was discarded, assuming that only proteins and organic contaminants are removed. The assumption was made based on the findings in Figure 4.26, here γ–NADA crystallization did not occur until a solvent fraction of 0.55. Further, unsuccessful antisolvent crystallization of *NF* concentrate in Figure A.18 supported the hypothesis, that until a certain *EtOH* concentration, no crystallization of γ–NADA occur. Yet, as shown in Figure 4.27a at an *EtOH* fraction of 0.45, the γ–NADA concentration in the supernatant fell far below the dilution line, indicating an already started crystallization.

Calculating the yield based on the amount of γ–NADA in the supernatant at an *EtOH* fraction of 0.45, 52.11±23.67 % were achieved. In conclusion, approximately 60 % of the initial γ–NADA after *NF* got lost due to the set-up failure, however this step made the high achieved purity possible. In summary, 67.6 mg γ–NADA crystals were obtained from 90 mL *NF* concentrate, however 99 mL were obtained after the *NF* step. Thus, 74.4 mg γ–NADA crystals could be obtained as expected from 99 mL *NF* concentrate, originating from initial 2.75 L of cell broth from the cultivation of *H. elongata* ΔectC. Thus, in total, 27.1 mg L^{-1} γ–NADA with a purity of 94.4±4.6 % were gained after the whole downstream process.

The significant difference in the starting conditions for the antisolvent crystallization shown in Figure A.18 and Figure 4.27 is the difference in purity (compare Table 4.4 and Table A.1). While *NF* concentrate, originating from 50 L cultivation (subsection 4.2.3) was 44.8±16.3 % pure, the purity of *NF* concentrate of the process described above was 20.6±5.3 %. The reduced purity did not result from a less performing filtration process, but from the lower volume which was concentrated. Since NaCl permeates nearly unhindered in the *NF* process, thus stays constant in the concentrate, the purity depends on the final reachable γ–NADA concentration, which is less, the less volume is processed. Yet, purity might be a reason while the antisolvent crystallization was successful for only one of the conditions. As already discussed in subsection 4.4.2, impurities shape the crystallization process [227] and in this case, since the final γ–NADA purity is high, enhance process performance [230, 238]. A second reason for the discrepancies in successful antisolvent crystallization might be the starting concentration of γ–NADA. The crystallization described here starts with 19.5±1.4 g L^{-1} γ–NADA, while after *NF* from 50 L cultivation a concentration of 15.8 ± 1.0 g L^{-1} (see Table 4.4) was reached. For crystallization a critical saturation is key to initiate nucleation. Thus, the slightly higher concentration could tip the scales in favor of a successful antisolvent crystallization run. A better process control could be achieved with seeding, simultaneously overcoming the drawback of reduced concentration since the metastable zone of nucleation can be influenced [239].

Summed up, antisolvent crystallization and in detail antisolvent crystallization with *EtOH* was proofed suitable for γ–NADA purification, from both ideal aqueous solutions (Figure 4.24 Figure 4.26) and biotechnologically produced *NF* concentrate (Figure 4.27). From *NF* concentrate, 67.6 mg crystalline γ–NADA with a purity of 94.4±4.6 % was obtained, which corresponds to a yield of 23.9±9.5 %. It became clear, that the upstream process step of filtration shapes and affects the crystallization process, yet a better process control could be reached with, for example, seeding. Since in the process set-up, an initial antisolvent step to an *EtOH* fraction of 0.45 was performed, the yield could be drastically increased with a smaller starting step. The total process will be in detail more discussed at the following.

4.5 Downstream process for Nγ-acetyl-L-2,4-diaminobutyric acid

In the previous sections, the potential of the product γ–NADA (section 4.1), the cultivation of the producer strain *H. elongata* ΔectC (section 4.2) and the downstream processing with a filtration cascade (section 4.3) and a subsequent crystallization (section 4.4) was demonstrated and discussed. Here, the whole process will be discussed, thus not focusing on the preliminary examinations.

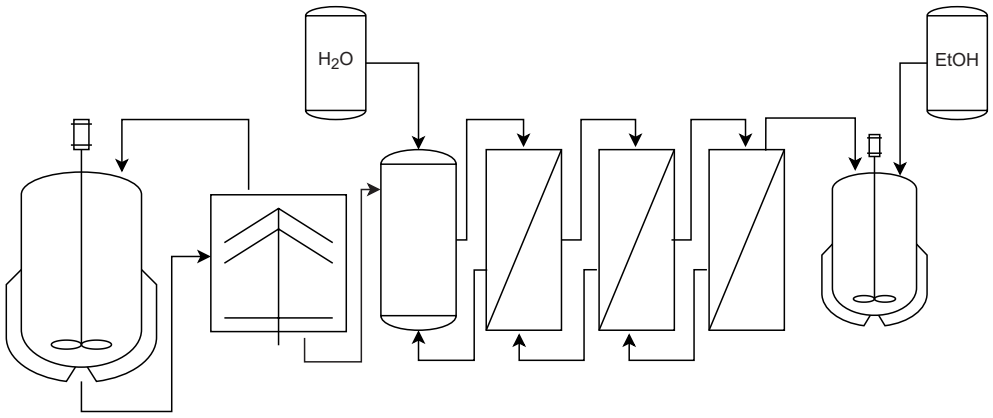

Figure 4.28: Production and purification process for γ–NADA from saline fermentation of *Halomonas elongata* ΔectC. Cultivation, filtration and crystallization are in detail discussed in section 4.2, section 4.3 and section 4.4.

Figure 4.28 shows the whole performed production and purification process of the compatible solute γ–NADA from cultivation of *H. elongata* ΔectC in MM63 medium with 1 M NaCl. The *H. elongata* strain, lacking of ectoine synthase (Figure 2.1) was cultivated in a batch process. Up to now, γ–NADA is produced intracellular [159], as also *H. elongata* wildtype produces the native compound ectoine intracellular. In industrial production of ectoine a *leaky mutant* is used, which excludes ectoine in the surrounding medium and thus ectoine yield is not dependent on the obtained cell dry weight [2]. Yet, for γ–NADA production, cells were separated via centrifugation and with a disc separator for *lab*-scale (see subsection 4.2.2) and *pilot*-scale cultivation (see subsection 4.2.3), respectively. Cell disruption was performed with osmotic shock by adding H_2O and additional freeze-thaw [118] to release the intracellular small molecule. A filtration cascade consisting of a microfiltration (*MF*), ultrafiltration (*UF*) and nanofiltration (*NF*) was performed downstream in *cross-flow* mode and the *NF* concentrate was used in an antisolvent crystallization step. Here, *EtOH* was step-wise added to solubilize γ–NADA. An additional cooling step resulted in γ–NADA crystals with a purity of 94.4±4.6 %.

The yield of the respective *DSP* steps are given in Table 4.2, Table 4.4 and Table 4.5. Since the filtration process (subsection 4.3.2) was not performed with the whole volume from cultivation (subsection 4.2.3 and final crystallization was performed with a newly processed cultivation broth (subsection 4.4.3) a whole balance can only calculated theoretically. After cultivation of *H. elongata* ΔectC a mass of 75.6±4.5 g γ–NADA was obtained. As the total filtration cascade and the crystallization step result in a yield of 24.2±3.53 % and 25.5±1.9 %, respectively, a theoretical final mass of γ–NADA crystals of 3.2±0.3 g could be calculated. This results in a overall process yield of 4.0±1.7 %. The low total yield results mainly from three drawbacks. Firstly, the set-up of the filtration plant which has a very high dead-volume compared to the membrane size. Secondly, the membrane size defines the maximum load and thus limits the processable feed volume. As is discussed in subsection 4.3.2 and is especially shown for *NF* in Figure 4.15, the breakthrough of the membrane reduced the yield of the *NF* step to 52.8±16.3 % (see Table 4.4). A larger membrane size thus would improve both, the total processable volume and the processable volume per time, simultaneously making the process more economic. Thirdly, as already described in section 4.4.3, loss in antisolvent crystallization results from the initial solvent step to a fraction of 0.45. Here, organic impurities, yet also γ–NADA, solidifies, meaning a loss of 179 mg of γ–NADA. Adapting the antisolvent crystallization with this knowledge, a much higher, maximum yield of above 86 % could be obtained in the crystallization step and with this, the overall process yield increases to 14.3±1.6 %. However, the high purity of over 94 % was probably just possible, due to this initial step which separated remaining organic impurities.
As a further measure, *UF* step could be omit. Table 4.4 shows that with performing *UF* no significant increase in purity was obtained, yet, as discussed in subsection 4.3.2, also the limits of the protein analysis could be a reason for the missing effect. However, less process steps in *DSP* always increase overall yield and financial expense.

As already mentioned, ectoine in large scale is produced with both, a *leaky mutant* and the "bacterial milking" procedure [2]. As described in Sauer & Galinski [26], the "bacterial milking" results in 155 mg g_{cells}^{-1} ectoine yield per process cycle. As osmotic shock works for the release of γ–NADA from the cells, the "bacterial milking" procedure is very likely also applicable for the *H. elongata* ΔectC strain and with a final γ–NADA concentration in a batch of 50 L of 0.35±0.02 g g_{AFDW}^{-1} (Table 4.1 in subsection 4.2.2), the described yield for ectoine [26] could theoretically be exceeded. Onraedt *et al.* [221] also showed a bacterial milking idea for ectoine from *Brevibacterium epidermis* with first H_2O and additional extraction cycles with *EtOH*. To separate NaCl and ectoine, cooling crystallization in *EtOH* was performed in repetitive cycles and a total process yield of 55%. Yet, the same observation of decreasing crystallization efficiency due to increasing impurity content was made as described for γ–NADA cooling crystallization in H_2O in subsection 4.4.2. Ectoine extraction with *aqueous biphasic system* from *Halomonas salina* is described by Wan *et al.* [240] and Ng *et al.* [241]

with poly(propylene) glycol and ionic liquids, respectively. Here, ectoine was also previously released from cells with osmotic shock. Both system are reported to gain high yields and purities. Chen *et al.* [242] describes a *DSP*, which has more similarities to the current project than those previously described and also the initial volume after cultivation is comparable to that of γ–NADA in subsection 4.2.3. Here [242], a filtration and desalination step is performed as initial purification step after acidification for cell lysis. Ectoine is further purified with chromatography, extraction and refining steps and the final yield and purity are described as 43 % yield and 95 %, respectively. Here, some steps require relative intense heating procedures and thus energy consumption might be very high.

5 Summary and Outlook

Compatible solutes, produced by halophilic microorganisms, have a high potential in the cosmetic and medical market. One of the most successful ones, biotechnologically produced in tons per year with the producer strain *Halomonas elongata*, is ectoine [2]. The precursor molecule Nγ-acetyl-L-2,4-diaminobutyric acid (γ-NADA) did not gain much attention yet. However, in vivo and in vitro, its stabilizing characteristics are already described [27, 41, 42]. Recently, Ahmadi *et al.* [1] proved the applicability of the molecule to be polymerized and act as drug delivery systems in dermal treatments, making the molecule more valuable and opening up a market. As demand for the compound requires the supply, here, the development and validation of both, a production process of γ-NADA with a genetically modified *H. elongata* strain (*H. elongata* ΔectC) and a downstream process (*DSP*) is shown.

Summary

First, however, the potential of γ–NADA as a protein stabilizer was demonstrated. Compared to the established compatible solutes ectoine, hydroxyectoine, and trehalose, γ-NADA showed the best thermal stabilization of BSA and streptavidin, two out of three tested proteins, in every tested NaCl concentration. The third protein, amylase, was nearly unaffected by the presence of ectoine, hydroxyectoine, and γ-NADA, yet with trehalose, the stabilizing effect was significant, thus assuming a different stabilization cause. Overall, the potential of γ-NADA as a stabilization additive was demonstrated, underlining the need for a potential production and purification process. The producer strain *H. elongata* ΔectC, kindly provided by Bundesanstalt für Materialforschung und -prüfung (*BAM*), is lacking ectoine synthase and thus accumulating γ-NADA as final, metabolic compatible solute [159]. The organism's required, intracellular compatible solute concentration depends on the surrounding salinity. Thus, the effect of NaCl in the cultivation process was examined using 0.5 M and 1.0 M in the cultivation medium. The final concentration of γ-NADA increased almost linear with increasing salt concentration, resulting in 0.62$\pm$0.03 g L^{-1} and 1.30$\pm$0.18 g L^{-1} in 0.5 M and 1.0 M NaCl, respectively. Related to the process time, which was 15.7$\pm$0.9 h and 22.5$\pm$0.3 h, the space time yield increases from 0.04$\pm$0.00 to 0.06$\pm$0.01 g L^{-1} h^{-1}. This economic factor

was the basis for deciding the higher salt content in the scaled-up process. Here, the up-scale to 50 L was performed with constant aeration and high salt media. The growth rate and process time remained constant compared to the *lab*-scale. Although, final OD_{600} was reduced, the final γ-NADA concentration increases to 1.51±0.10 g L^{-1} and with this the space time yield increases to 0.07±0.00 g L^{-1} h^{-1}.

As initial *DSP* step, a filtration cascade with a microfiltration (*MF*), ultrafiltration (*UF*), and nanofiltration (*NF*) should be implemented. First, a membrane and parameter screening identified the most suitable membrane, fitting transmembrane pressure (Δp_{TM}) and feed flow rate (Q_F) for the respective filtration size. The decision was made based on the permeation/rejection of γ-NADA and the impurities NaCl and proteins and the permeate flow rate (Q_P). Also, the cleanability and reusability of the membranes were considered. For *MF* the *Synder V0.2* membrane with a Δp_{TM} of 3 bar and a Q_F of 10 L h^{-1}, for *UF* the *Synder MQ50* with a Δp_{TM} of 2 bar and a Q_F of 10 L h^{-1} and for *NF* the *Desal/GE DL* membrane with a Δp_{TM} of 10 bar and a Q_F of 10 L h^{-1} were finally chosen. Yet, for *MF* and *NF*, an optimization was performed, screening a broader range of Δp_{TM}, also including temperature (T) - 25°C, 35°C and 45°C. As Q_F did not show a relevant effect on the filtration performance, it was set constant to 10 L h^{-1}. For *MF*, a higher T of 45°C was chosen after optimization for the long-term and cascade process; for *NF*, a clear statement cannot be made, since a higher T and higher Δp_{TM} positively affects Q_P, however, a lower T and lower Δp_{TM} shows a better separation of species and less fouling. The finally screened parameters and membranes for the cascade process are summarized in Table 5.1.

Table 5.1: Summary of filtration parameters in the longterm and cascade process to purify and concentrate the process stream and separate γ-NADA.

Filtration step	**Membrane type**	$\boldsymbol{Q_F}$ **[L** $\mathbf{h^{-1}}$**]**	$\boldsymbol{\Delta p_{TM}}$ **[bar]**	$\boldsymbol{T}$ **[°C]**
MF	*Synder V0.2*	10	3	45°C
UF	*Synder MQ50*	10	2	35°C
NF	*Desal/GE DL*	10	10	35°C

The cascade process started with a *MF* and a feed volume of, in total, 5.2 L, yet fouling was very pronounced, and thus, three filtration rounds had to be performed to process the total volume. The permeate was collected and used as feed in *UF*. Here, the long-term filtration process ran stable over the whole process time with an excellent yield of nearly 94 %. Again, collected permeate was used as feed in the downstream *NF*. γ-NADA was finally concentrated and desalinated since NaCl permeates unhindered. However, *NF* showed that the maximum load of a flat sheet membrane is limited, as a breakthrough was observed at the end of the process. Yet, a final concentration of γ-NADA of 15.8±1.0 g L^{-1} was obtained, which was the starting condition for the subsequent antisolvent crystallization.

Suitable solvents for both cooling and antisolvent crystallization were initially screened to design a potent crystallization process. Here, H_2O combined a temperature-dependent solubility and the fact that γ-NADA is biotechnologically produced and processed in an aqueous medium. Thus, H_2O was chosen as a suitable solvent for cooling crystallization. As the solubility of γ-NADA was high in H_2O and low in *EtOH*, changes with increasing *EtOH* fractions and performed well in crystallization-pretests, *EtOH* was selected as antisolvent to crystallize γ-NADA from the aqueous surrounding. Cooling crystallization, under the conditions of cooling from 50°C to 20°C and 300 rpm constant stirring, was performed with model solutions consisting of saturated γ-NADA and several foreign species: ectoine, α–NADA and NaCl. Here, a purity of 97.8±0.32 % and a yield of nearly 48 % was reached, yet when performing in a continuous set-up, process efficiency significantly decreases to lower purities and yield. Seeding and increasing shear forces with changing impeller speed fastens the crystallization kinetics. However, cooling crystallization at this point was not applicable for the process stream from *NF*, as the concentration was too low. Thus, antisolvent crystallization with *EtOH* was performed. Here, pretests with saturated γ-NADA solutions showed a good crystallization behavior when decreasing the concentration to the process conditions. The crystallization of γ-NADA from *NF* concentrate and an additional cooling crystallization to 4°C resulted in 67.6 mg crystals with a purity of 94.4±4.6. Yet, as a large proportion of γ-NADA was accidentally lost in the first solvent fraction step, the yield was reduced to 24 %. The overall process yield was theoretically calculated to 4.0±1.7 %. The significant drawbacks were identified as the loss in the crystallization step and the set-up of the filtration plant, as here, a high dead volume was accepted. Nevertheless, a proof of concept for the *DSP* of γ-NADA from *H. elongata* ΔectC was demonstrated, which overcomes more energy intense process steps like electrodialysis or extraction. In the following, potential next steps are discussed.

Outlook

Regarding the shown production and purification process of γ-NADA, future attention should be paid to improving process yield and efficiency. The process yield generally depends on the initial concentration and overall amount of the target in the process. Thus, the cultivation and production process for γ-NADA should be improved. As γ-NADA is intracellularly produced by *H. elongata* ΔectC, the 'bacterial milking' procedure, where the solute is washed-out in regular passages with osmotic down-shocking [2, 26], could improve space-time-yield. After each cycle, the enriched supernatant is collected, and cells are reused in the next producing cycle. Another process improvement would be a *fed-batch* cultivation (compare subsection 2.2.1). Here, side products due to a high initial glucose concentration would be reduced, and the substrate would be directed to the solute production. Additionally,

an overall higher cell content and, with this, a higher target concentration could be easily obtained. Further, the feeding strategy in *fed-batch* cultivation could take advantage of the salt dependence of γ-NADA production. The initial batch could start with a NaCl concentration at the maximum growth rate for maximum cell amount. The subsequent feeding could increase NaCl in the cultivation by feeding both substrate and NaCl, thus increasing target production. This would be comparable to bioprocesses, where protein expression is controlled by an operon and can be induced with a specific agent. Further, if a *leaky*-mutant for γ-NADA could be designed, the production of the target is independent of the biomass content, resulting in a higher product concentration [2]. Further, NaCl in the system could be reduced as no intracellular solute limit is reached, and thus growth rate increases, which is advantageous regarding the efficiency of the process. The cultivation of *H elongata* ΔectC could be more sustainable when taking advantage of the high salt concentration required. With this, the requirements for sterility are very low, and open, continuous, non-sterile processes might be possible. Further, the use of waste or sea water instead of defined medium compositions would develop the process in the right, more economical, and ecological direction [7, 8].

If a potential *leaky* strain would be used in cultivation, the *MF* step could be directly integrated into the cultivation process and separate the enriched supernatant from the cells without needing a cell separation step such as centrifugation. Here, the high NaCl conditions, which the halophilic strain requires, almost exclude the risk of contamination on the membrane system. This application would also be possible when performing the 'bacterial milking' procedure, but the advantage of less contamination risk no longer exists. In general, the filtration cascade and the obtained yields could more or less easily be improved by scaling the membrane size to a more preparative scale. This would increase the permeate flux Q_P, increase the maximum load the membrane can tolerate, and thirdly, losses due to dead volume could be reduced with another setup. Another idea to decrease the dead volume, at least in *MF*, would be changing from *cross-flow* to *dead-end* mode. Here, the drawbacks of an increasing filter cake and with this decreasing Q_P have to be taken into account, yet the whole process volume after cell lysis would be yielded in the permeate [243]. However, above a specific process volume, the relative dead volume becomes negligibly small, which in turn would make a *cross-flow* setup advantageous. As *UF* did not show relevant improvement of the purity of γ-NADA, it would be worth checking if skipping the *UF* step and performing *NF* directly after cell debris separation in *MF* would show the same process performance. Economizing a process step, in general, increases yield and efficiency of a *DSP*.

The yield of a cooling crystallization process is typically dependent on the temperature dependence of the molecule in the solvent - the steeper the solubility curve, the higher the theoretical yield. Yet, a high solubility is also advantageous as less solvent is needed for saturation. Since γ-NADA is produced in aqueous conditions, choosing H_2O as solvent is obvious. However, the efficiency of the process could be increased with faster nucleation and

crystallization kinetics, e.g., more focus on seeding and parameter settings in the process. Another setup and a scale-up for the antisolvent crystallization, which was finally performed as the final process step in the biotechnological production of γ-NADA, would round off the process. Antisolvent crystallization was yet only performed in *lab*-scale of 5 mL; a scale-up would bring the idea closer to industrial conditions. Further, the crystallization of γ–NADA has been performed only in a *batch*-setup. However, adapting the process to a continuous workflow would benefit from fewer batch-to-batch variations and better control. Here, the process setup could be adjusted to, for example, a *plug-flow* setup [108, 244] (compare subsection 2.4.3) - various strategies are conceivable: Alvarez & Myerson [108] demonstrated better control of the crystal size of the amino acid L-glutamic acid with a customized *PFR* for antisolvent crystallization, but also a *PFR* setup with several temperature sections, as modeled by Kwon *et al.* [107], could be an option. The obtained γ-NADA crystals also require more examination, yet needle-shaped morphology and crystal structure were shown in Martin *et al.* [100]. However, relevant process characteristics like crystal size distribution (*CSD*), metastable zone width (*MSZW*), and thermodynamic examinations have not been considered yet. All could contribute to gaining more quality control over the crystallization process and shaping the final solids to suitable morphology.
Finally, the application range of γ-NADA should be further investigated. The potential of γ-NADA to stabilize several proteins was shown here. Ahmadi *et al.* [1] opened up another field and demonstrated that polymerized γ-NADA can act as drug delivery system for dermal treatment. Several other applications are possible, as the potential and application of other molecules of this class are shown and reviewed various times.

6 Bibliography

1. Ahmadi, V., Zabihi, F., Rancan, F., Staszak, A. A., Nie, C., Dimde, M., Achazi, K., Wiehe, A., Vogt, A. & Haag, R. Amphiphilic co-polypeptides self-assembled into spherical nanoparticles for dermal drug delivery. *ACS Applied Nano Materials* **4,** 6709–6721 (2021).
2. Kunte, H. J., Lentzen, G. & Galinski, E. Industrial production of the cell protectant ectoine: protection mechanisms, processes, and products. *Current Biotechnology* **3,** 10–25 (2014).
3. Tuesta-Popolizio, D. A., Velázquez-Fernández, J. B., Rodriguez-Campos, J. & Contreras-Ramos, S. M. Thalassobacillus, a genus of extreme to moderate environmental halophiles with biotechnological potential. *World Journal of Microbiology and Biotechnology* **37,** 1–13 (2021).
4. Coker, J. A. Extremophiles and biotechnology: current uses and prospects. *F1000Research* **5** (2016).
5. Wakai, S. Biochemical and thermodynamic analyses of energy conversion in extremophiles. *Bioscience, Biotechnology, and Biochemistry* **83,** 49–64 (2019).
6. Yin, J., Chen, J.-C., Wu, Q. & Chen, G.-Q. Halophiles, coming stars for industrial biotechnology. *Biotechnology Advances* **33,** 1433–1442 (2015).
7. Johnson, K., Jiang, Y., Kleerebezem, R., Muyzer, G. & Van Loosdrecht, M. C. M. Enrichment of a mixed bacterial culture with a high polyhydroxyalkanoate storage capacity. *Biomacromolecules* **10,** 670–676 (2009).
8. Yue, H., Ling, C., Yang, T., Chen, X., Chen, Y., Deng, H., Wu, Q., Chen, J. & Chen, G.-Q. A seawater-based open and continuous process for polyhydroxyalkanoates production by recombinant halomonas campaniensis LS21 grown in mixed substrates. *Biotechnology for Biofuels* **7,** 1–12 (2014).
9. Galinski, E. A. Osmoadaptation in bacteria. *Advances in Microbial Physiology* **37,** 273–328 (1995).
10. Oren, A. Thermodynamic limits to microbial life at high salt concentrations. *Environmental Microbiology* **13,** 1908–1923 (2011).
11. Kunte, H. J., Trüper, H. G. & Stan-Lotter, H. in *Astrobiology* 185–200 (Springer, 2002).

12. Lanyi, J. K. Salt-dependent properties of proteins from extremely halophilic bacteria. *Bacteriological Reviews* **38,** 272 (1974).

13. Dennis, P. P. & Shimmin, L. C. Evolutionary divergence and salinity-mediated selection in halophilic archaea. *Microbiology and Molecular Biology Reviews* **61,** 90–104. ISSN: 1092-2172 (1997).

14. Kunte, H. J. Osmoregulation in bacteria: compatible solute accumulation and osmosensing. *Environmental Chemistry* **3,** 94–99 (2006).

15. Martinac, B. Mechanosensitive channels in prokaryotes. *Cellular Physiology and Biochemistry* **11,** 61–76 (2001).

16. Grammann, K., Volke, A. & Kunte, H. J. New type of osmoregulated solute transporter identified in halophilic members of the bacteria domain: trap transporter teaabc mediates uptake of ectoine and hydroxyectoine in halomonas elongata dsm 2581t. *Journal of Bacteriology* **184,** 3078–3085 (2002).

17. Vandrich, J., Pfeiffer, F., Alfaro-Espinoza, G. & Kunte, H. J. Contribution of mechanosensitive channels to osmoadaptation and ectoine excretion in halomonas elongata. *Extremophiles* **24,** 421–432 (2020).

18. Empadinhas, N. & Da Costa, M. S. Diversity, distribution and biosynthesis of compatible solutes in prokaryotes. *Contributions to Science,* 95–105 (2009).

19. Crowley, E. Compatible solute ectoine review: protection mechanisms and production methods. *Journal of Undergraduate Studies at Trent (JUST)* **5,** 32–39 (2017).

20. Sahle, C. J., Schroer, M. A., Jeffries, C. M. & Niskanen, J. Hydration in aqueous solutions of ectoine and hydroxyectoine. *Physical Chemistry Chemical Physics* **20,** 27917–27923 (2018).

21. Smiatek, J., Harishchandra, R. K., Rubner, O., Galla, H.-J. & Heuer, A. Properties of compatible solutes in aqueous solution. *Biophysical Chemistry* **160,** 62–68. ISSN: 0301-4622 (2012).

22. Panuszko, A., Bruździak, P., Kaczkowska, E. & Stangret, J. General mechanism of osmolytes' influence on protein stability irrespective of the type of osmolyte cosolvent. *The Journal of Physical Chemistry B* **120,** 11159–11169 (2016).

23. Zeman, J., Holm, C. & Smiatek, J. The effect of small organic cosolutes on water structure and dynamics. *Journal of Chemical & Engineering Data* **65,** 1197–1210 (2019).

24. Galinski, E. A., Pfeiffer, H. & Trüper, H. G. 1,4,5,6-tetrahydro-2-methyl-4-pyrimidinecarboxylic acid: a novel cyclic amino acid from halophilic phototrophic bacteria of the genus ectothiorhodospira. *European Journal of Biochemistry* **149,** 135–139 (1985).

25. Schwibbert, K., Marin-Sanguino, A., Bagyan, I., Heidrich, G., Lentzen, G., Seitz, H., Rampp, M., Schuster, S. C., Klenk, H. & Pfeiffer, F. A blueprint of ectoine metabolism from the genome of the industrial producer halomonas elongata dsm 2581t. *Environmental Microbiology* **13,** 1973–1994. ISSN: 1462-2912 (2011).

26. Sauer, T. & Galinski, E. A. Bacterial milking: a novel bioprocess for production of compatible solutes. eng. *Biotechnology and Bioengineering* **57,** 306–13 (3 Feb. 1998).

27. García-Estepa, R., Canovas, D., Iglesias-Guerra, F., Ventosa, A., Csonka, L. N., Nieto, J. J. & Vargas, C. Osmoprotection of salmonella enterica serovar typhimurium by Ny-acetyldiaminobutyrate, the precursor of the compatible solute ectoine. *Systematic and Applied Microbiology* **29,** 626–633. ISSN: 0723-2020 (2006).

28. Göller, K. & Galinski, E. A. Protection of a model enzyme (lactate dehydrogenase) against heat, urea and freeze-thaw treatment by compatible solute additives. *Journal of Molecular Catalysis B: Enzymatic* **7,** 37–45 (1999).

29. Barth, S., Huhn, M., Matthey, B., Klimka, A., Galinski, E. A. & Engert, A. Compatible-solute-supported periplasmic expression of functional recombinant proteins under stress conditions. *Applied and Environmental Microbiology* **66,** 1572–1579 (2000).

30. Salmannejad, F. & Nafissi-Varcheh, N. Ectoine and hydroxyectoine inhibit thermal-induced aggregation and increase thermostability of recombinant human interferon alfa2b. *European Journal of Pharmaceutical Sciences* **97,** 200–207 (2017).

31. Jorge, C. D., Borges, N., Bagyan, I., Bilstein, A. & Santos, H. Potential applications of stress solutes from extremophiles in protein folding diseases and healthcare. *Extremophiles* **20,** 251–259 (2016).

32. Tran, B.-H., Dao, V.-A., Bilstein, A., Unfried, K., Shah-Hosseini, K. & Mösges, R. Ectoine-containing inhalation solution versus saline inhalation solution in the treatment of acute bronchitis and acute respiratory infections: a prospective, controlled, observational study. *BioMed Research International* **2019** (2019).

33. Unfried, K., Krämer, U., Sydlik, U., Autengruber, A., Bilstein, A., Stolz, S., Marini, A., Schikowski, T., Keymel, S. & Krutmann, J. Reduction of neutrophilic lung inflammation by inhalation of the compatible solute ectoine: a randomized trial with elderly individuals. *International Journal of Chronic Obstructive Pulmonary Disease* **11,** 2573 (2016).

34. Bünger, J., Degwert, J. & Driller, H. The protective function of compatible solute ectoin on the skin, skin cells and its biomolecules with respect to uv radiation, immunosuppression and membrane damage. *IFSCC Mag* **4,** 127–131 (2001).

35. Marini, A., Reinelt, K., Krutmann, J. & Bilstein, A. Ectoine-containing cream in the treatment of mild to moderate atopic dermatitis: a randomised, comparator-controlled, intra-individual double-blind, multi-center trial. *Skin Pharmacology and Physiology* **27,** 57–65 (2014).

36. Dao, V. A., Bilstein, A., Overhagen, S., Géczi, L., Baráth, Z. & Mösges, R. Effectiveness, tolerability, and safety of ectoine-containing mouthwash versus those of a calcium phosphate mouthwash for the treatment of chemotherapy-induced oral mucositis: a prospective, active-controlled, non-interventional study. *Oncology and Therapy* **6,** 59–72 (2018).

37. Kanapathipillai, M., Lentzen, G., Sierks, M. & Park, C. B. Ectoine and hydroxyectoine inhibit aggregation and neurotoxicity of alzheimer's β-amyloid. *FEBS Letters* **579,** 4775–4780. ISSN: 0014-5793 (2005).

38. Borjian-Boroujeni, M. & Nayeri, H. Interaction of bovine lactoperoxidase with hydroxyectoine: stabilizing effect study. *Biologia* **76,** 1285–1296 (2021).

39. Liss, I. N-acetyldiaminobuttersäure, eine neue Aminosäure aus dem Latex von Euphorbia pulcherrima Willd ex Klotzsch. *Phytochemistry* **1,** 87–88. ISSN: 0031-9422 (1962).

40. Fowden, L. Amino acid complement of plants. *Phytochemistry* **11,** 2271–2276 (1972).

41. Cánovas, D., Vargas, C., Iglesias-Guerra, F., Csonka, L. N., Rhodes, D., Ventosa, A. & Nieto, J. J. Isolation and characterization of salt-sensitive mutants of the moderate halophile halomonas elongata and cloning of the ectoine synthesis genes. *Journal of Biological Chemistry* **272,** 25794–25801 (1997).

42. Cánovas, D., Borges, N., Vargas, C., Ventosa, A., Nieto, J. J. & Santos, H. Role of Nγ-acetyldiaminobutyrate as an enzyme stabilizer and an intermediate in the biosynthesis of hydroxyectoine. *Applied and Environmental Microbiology* **65,** 3774–3779. ISSN: 0099-2240 (1999).

43. Chmiel, H. *Bioprozesstechnik* 2nd ed. (Spektrum Akademischer Verlag, 2006).

44. Dötsch, A., Severin, J., Alt, W., Galinski, E. A. & Kreft, J.-U. A mathematical model for growth and osmoregulation in halophilic bacteria. *Microbiology* **154,** 2956–2969 (2008).

45. Maier, R. M., Pepper, I. L., Pepper, I. L., Gerba, C. P. & Gentry, T. J. in *Environmental Microbiology (Third Edition)* 37–56 (Academic Press, San Diego, 2015). doi:10.1016/B978-0-12-394626-3.00003-X. https://www.sciencedirect.com/science/article/pii/B978012394626300003X.

46. Monod, J. Recherches sur la croissance des cultures bacteriennes (1942).

47. Hobmeier, K. A. *Metabolic engineering of Halomonas elongata for enhanced production of compatible solutes* PhD thesis (Technical University of Munich, 2023).

48. Melin, T. & Rautenbach, R. *Membranverfahren: Grundlagen der Modul-und Anlagenauslegung* 3rd ed. (Springer-Verlag, 2007).

49. Davis, R. H., Basile, A. & Charcosset, C. in *Current Trends and Future Developments on (Bio-) Membranes* 29–67 (Elsevier, 2019). doi:10.1016/B978-0-12-813606-5.00002-6. https://www.sciencedirect.com/science/article/pii/B9780128136065000026.

50. Bhattacharya, P. K., Agarwal, S., De, S. & Gopal, U. R. Ultrafiltration of sugar cane juice for recovery of sugar: analysis of flux and retention. *Separation Science and Technology* **21,** 247–259 (2001).

51. Van der Bruggen, B., Koninckx, A. & Vandecasteele, C. Separation of monovalent and divalent ions from aqueous solution by electrodialysis and nanofiltration. *Water Research* **38,** 1347–1353 (2004).

52. Van der Bruggen, B. Nanofiltration. *Encyclopedia of Membrane Science and Technology,* 1–23 (2013).

53. Epsztein, R., Shaulsky, E., Dizge, N., Warsinger, D. M. & Elimelech, M. Role of ionic charge density in donnan exclusion of monovalent anions by nanofiltration. *Environmental Science & Technology* **52,** 4108–4116 (2018).

54. Van der Bruggen, B. & Luis, P. in *Fundamental Modelling of Membrane Systems* 25–70 (Elsevier, 2018). doi:10.1016/B978-0-12-813483-2.00002-2. https://www.sciencedirect.com/science/article/pii/B9780128134832000022.

55. Harrison, R. G., Todd, P. W., Rudge, S. R. & Petrides, D. P. eng. in *Bioseparation Science and Engineering* 104–141 (Oxford University Press, 2003). doi:10.1093/oso/9780195391817.003.0007. https://oxford.universitypressscholarship.com/10.1093/oso/9780195391817.001.0001/isbn-9780195391817-book-part-7.

56. Arunkumar, A., Molitor, M. S. & Etzel, M. R. Comparison of flat-sheet and spiral-wound negatively-charged wide-pore ultrafiltration membranes for whey protein concentration. *International Dairy Journal* **56,** 129–133 (2016).

57. Ribera, G., Llenas, L., Martínez, X., Rovira, M. & de Pablo, J. Comparison of nanofiltration membranes' performance in flat sheet and spiral wound configurations: a scale-up study. *Desalination and Water Treatment* **51,** 458–468 (2013).

58. Wang, Y. & Liang, Z. Solvent effects on the crystal growth structure and morphology of the pharmaceutical dirithromycin. *Journal of Crystal Growth* **480,** 18–27 (2017).

59. Wan, C. F., Yang, T., Lipscomb, G. G., Stookey, D. J. & Chung, T.-S. Design and fabrication of hollow fiber membrane modules. *Journal of Membrane Science* **538,** 96–107 (2017).

60. Baker, R. W. Membrane technology. *Encyclopedia of Polymer Science and Technology* **3** (2002).

61. Schwinge, J., Neal, P. R., Wiley, D. E., Fletcher, D. F. & Fane, A. G. Spiral wound modules and spacers: review and analysis. *Journal of Membrane Science* **242,** 129–153 (2004).

62. Wang, X.-L., Fang, Y. Y., Tu, C.-H. & Van der Bruggen, B. Modelling of the separation performance and electrokinetic properties of nanofiltration membranes. *International Reviews in Physical Chemistry* **31,** 111–130 (2012).

63. Schmidt, C. M., Mailänder, L. K. & Hinrichs, J. Fractionation of mono-and disaccharides via nanofiltration: influence of pressure, temperature and concentration. *Separation Science and Technology* **211,** 571–577 (2019).

64. Vezzani, D. & Bandini, S. Donnan equilibrium and dielectric exclusion for characterization of nanofiltration membranes. *Desalination* **149,** 477–483 (2002).

65. Roy, Y. & Warsinger, D. M. Effect of temperature on ion transport in nanofiltration membranes: diffusion, convection and electromigration. *Desalination* **420,** 241–257 (2017).

66. Bandini, S. & Vezzani, D. Nanofiltration modeling: the role of dielectric exclusion in membrane characterization. *Chemical Engineering Science* **58,** 3303–3326 (2003).

67. Donnan, F. G. Theorie der membrangleichgewichte und membranpotentiale bei vorhandensein von nicht dialysierenden elektrolyten. ein beitrag zur physikalisch-chemischen physiologie. *Zeitschrift für Elektrochemie und angewandte physikalische Chemie* **17,** 572–581 (1911).

68. Donnan, F. G. & Harris, A. B. Clxxvii.—the osmotic pressure and conductivity of aqueous solutions of congo-red, and reversible membrane equilibria. *Journal of the Chemical Society, Transactions* **99,** 1554–1577 (1911).

69. Donnan, F. G. Theory of membrane equilibria and membrane potentials in the presence of non-dialysing electrolytes. a contribution to physical-chemical physiology. *Journal of Membrane Science* **100,** 45–55 (1995).

70. Saliha, B., Patrick, F. & Anthony, S. Investigating nanofiltration of multi-ionic solutions using the steric, electric and dielectric exclusion model. *Chemical Engineering Science* **64,** 3789–3798 (2009).

71. Timmer, J. M. K., Speelmans, M. P. J. & Van Der Horst, H. C. Separation of amino acids by nanofiltration and ultrafiltration membranes. *Separation Science and Technology* **14,** 133–144 (1998).

72. Schaep, J., Van der Bruggen, B., Vandecasteele, C. & Wilms, D. Influence of ion size and charge in nanofiltration. *Separation Science and Technology* **14,** 155–162 (1998).

73. Pujar, N. S. & Zydney, A. L. Electrostatic effects on protein partitioning in size-exclusion chromatography and membrane ultrafiltration. *Journal of Chromatography A* **796,** 229–238 (1998).

74. Luo, J. & Wan, Y. Effects of ph and salt on nanofiltration—a critical review. *Journal of Membrane Science* **438,** 18–28 (2013).

75. Rohani, M. M. & Zydney, A. L. Role of electrostatic interactions during protein ultrafiltration. *Advances in Colloid and Interface Science* **160,** 40–48 (2010).

76. Teixeira, M. R., Rosa, M. J. & Nyström, M. The role of membrane charge on nanofiltration performance. *Journal of Membrane Science* **265,** 160–166 (2005).

77. Garem, A., Daufin, G., Maubois, J. L. & Leonil, J. Selective separation of amino acids with a charged inorganic nanofiltration membrane: effect of physicochemical parameters on selectivity. *Biotechnology and Bioengineering* **54,** 291–302 (1997).

78. Van der Bruggen, B., Schaep, J., Wilms, D. & Vandecasteele, C. Influence of molecular size, polarity and charge on the retention of organic molecules by nanofiltration. *Journal of Membrane Science* **156,** 29–41 (1999).

79. Luis, P. in *Fundamental Modelling of Membrane Systems* 1–23 (Elsevier, 2018). doi:10.1016/B978-0-12-813483-2.00001-0. https://www.sciencedirect.com/science/article/pii/B9780128134832000010.

80. Guo, W., Ngo, H.-H. & Li, J. A mini-review on membrane fouling. *Bioresource Technology* **122,** 27–34 (2012).

81. AlSawaftah, N., Abuwatfa, W., Darwish, N. & Husseini, G. A comprehensive review on membrane fouling: mathematical modelling, prediction, diagnosis, and mitigation. *Water* **13,** 1327 (2021).

82. Cirillo, A. I., Tomaiuolo, G. & Guido, S. Membrane fouling phenomena in microfluidic systems: from technical challenges to scientific opportunities. *Micromachines* **12,** 820 (2021).

83. Hong, H., Zhang, M., He, Y., Chen, J. & Lin, H. Fouling mechanisms of gel layer in a submerged membrane bioreactor. *Bioresource Technology* **166,** 295–302 (2014).

84. Vela, M. C. V., Blanco, S. Á., García, J. L. & Rodríguez, E. B. Analysis of membrane pore blocking models applied to the ultrafiltration of peg. *Separation and Purification Technology* **62,** 489–498 (2008).

85. Hilal, N., Ogunbiyi, O. O., Miles, N. J. & Nigmatullin, R. Methods employed for control of fouling in mf and uf membranes: a comprehensive review. *Separation Science and Technology* **40,** 1957–2005 (2005).

86. Myint, A. A., Lee, W., Mun, S., Ahn, C. H., Lee, S. & Yoon, J. Influence of membrane surface properties on the behavior of initial bacterial adhesion and biofilm development onto nanofiltration membranes. *Biofouling* **26,** 313–321 (2010).

87. Park, N., Kwon, B., Kim, I. S. & Cho, J. Biofouling potential of various nf membranes with respect to bacteria and their soluble microbial products (smp): characterizations, flux decline, and transport parameters. *Journal of Membrane Science* **258,** 43–54 (2005).

88. Myerson, A. S., Erdemir, D. & Lee, A. Y. *Handbook of Industrial Crystallization* 3rd ed. doi:10.1017/9781139026949. https://www.cambridge.org/core/books/handbook-of-industrial-crystallization/3EB3E65AEB84BDA20A0372A503DF30FE (Cambridge University Press, Cambridge, 2019).

89. Moffitt Schall, J. & Myerson, A. S. in *Handbook of Industrial Crystallization* (eds Myerson, A. S., Erdemir, D. & Lee, A. Y.) 3rd ed., 1–31 (Cambridge University Press, 2019). doi:10.1017/9781139026949.001.

90. Volmer, M. & Weber, A. Keimbildung in übersättigten gebilden. *Zeitschrift für physikalische Chemie* **119,** 277–301 (1926).

91. Becker, R. & Döring, W. Kinetische Behandlung der Keimbildung in übersättigten Dämpfen. *Annalen der Physik* **416,** 719–752 (1935).

92. Erdemir, D., Lee, A. Y. & Myerson, A. S. in *Handbook of Industrial Crystallization* (eds Myerson, A. S., Erdemir, D. & Lee, A. Y.) 3rd ed., 76–114 (Cambridge University Press, 2019). doi:10.1017/9781139026949.003.

93. Erdemir, D., Lee, A. Y. & Myerson, A. S. Nucleation of crystals from solution: classical and two-step models. *Accounts of Chemical Research* **42,** 621–629 (2009).

94. Karthika, S., Radhakrishnan, T. K. & Kalaichelvi, P. A review of classical and nonclassical nucleation theories. *Crystal Growth & Design* **16,** 6663–6681 (2016).

95. Gebauer, D., Volkel, A. & Colfen, H. Stable prenucleation calcium carbonate clusters. *Science* **322,** 1819–1822 (2008).

96. Knezic, D., Zaccaro, J. & Myerson, A. S. Nucleation induction time in levitated droplets. *The Journal of Physical Chemistry B* **108,** 10672–10677 (2004).

97. Zaccaro, J., Matic, J., Myerson, A. S. & Garetz, B. A. Nonphotochemical, laser-induced nucleation of supersaturated aqueous glycine produces unexpected γ-polymorph. *Crystal Growth & Design* **1,** 5–8 (2001).

98. Pan, W., Kolomeisky, A. B. & Vekilov, P. G. Nucleation of ordered solid phases of proteins via a disordered high-density state: phenomenological approach. *The Journal of Chemical Physics* **122,** 174905 (2005).

99. Lee, A. Y., Erdemir, D. & Myerson, A. S. in *Handbook of Industrial Crystallization* (eds Myerson, A. S., Erdemir, D. & Lee, A. Y.) 3rd ed., 32–75 (Cambridge University Press, 2019). doi:10.1017/9781139026949.002.

100. Martin, L., Klein, W., Schwaminger, S. P., Fässler, T. F. & Berensmeier, S. Crystal structure and spectroscopic analysis of the compatible solute Nγ-acetyl-l-2, 4-diaminobutyric acid. *Crystals* **10,** 1136 (2020).

101. Rauls, M., Bartosch, K., Kind, M., Lacmann, R., Mersmann, A., *et al.* The influence of impurities on crystallization kinetics–a case study on ammonium sulfate. *Journal of Crystal Growth* **213,** 116–128 (2000).

102. Jung, T., Kim, W.-S. & Choi, C. K. Crystal structure and morphology control of calcium oxalate using biopolymeric additives in crystallization. *Journal of Crystal Growth* **279,** 154–162 (2005).

103. Srinivasan, K., Sankaranarayanan, K., Thangavelu, S. & Ramasamy, P. Influence of organic solvents on the habit of nmba (4-nitro-4-methyl benzylidene aniline) crystals. *Journal of Crystal Growth* **212,** 246–254 (2000).

104. Nishio, S., Kavanagh, J. P. & Garside, J. A small-scale continuous mixed suspension mixed product removal crystallizer. *Chemical Engineering Science* **46,** 709–711 (1991).

105. Rasmuson, Å. C. in *Handbook of Industrial Crystallization* (eds Myerson, A. S., Erdemir, D. & Lee, A. Y.) 3rd ed., 172–196 (Cambridge University Press, 2019). doi:10.1017/9781139026949.006.

106. Eren, A., Civati, F., Ma, W., Gamekkanda, J. C. & Myerson, A. S. Continuous crystallization and its potential use in drug substance manufacture: a review. *Journal of Crystal Growth,* 126958 (2022).

107. Kwon, J. S.-I., Nayhouse, M., Orkoulas, G. & Christofides, P. D. Crystal shape and size control using a plug flow crystallization configuration. *Chemical Engineering Science* **119,** 30–39 (2014).

108. Alvarez, A. J. & Myerson, A. S. Continuous plug flow crystallization of pharmaceutical compounds. *Crystal Growth & Design* **10,** 2219–2228 (2010).

109. Hu, C. Reactor design and selection for effective continuous manufacturing of pharmaceuticals. *Journal of Flow Chemistry* **11,** 243–263 (2021).

110. Alvarez, A. J., Singh, A. & Myerson, A. S. Crystallization of cyclosporine in a multistage continuous msmpr crystallizer. *Crystal Growth & Design* **11,** 4392–4400 (2011).

111. Ståhl, M., Åslund, B. L. & Rasmuson, Å. C. Reaction crystallization kinetics of benzoic acid. *AIChE Journal* **47,** 1544–1560 (2001).

112. Gradl, J., Schwarzer, H.-C., Schwertfirm, F., Manhart, M. & Peukert, W. Precipitation of nanoparticles in a t-mixer: coupling the particle population dynamics with hydrodynamics through direct numerical simulation. *Chemical Engineering and Processing: Process Intensification* **45,** 908–916 (2006).

113. Bałdyga, J. & Orciuch, W. Barium sulphate precipitation in a pipe—an experimental study and cfd modelling. *Chemical Engineering Science* **56,** 2435–2444 (2001).

114. Schwarzer, H. & Peukert, W. Combined experimental/numerical study on the precipitation of nanoparticles. *AIChE Journal* **50,** 3234–3247 (2004).

115. Mersmann, A. & Kind, M. Auslegungsgrundlagen von kristallisatoren. *Chemie Ingenieur Technik* **57,** 190–200 (1985).

116. Li, J., Lai, T.-t. C., Trout, B. L. & Myerson, A. S. Continuous crystallization of cyclosporine: effect of operating conditions on yield and purity. *Crystal Growth & Design* **17,** 1000–1007 (2017).

117. Ferguson, S., Morris, G., Hao, H., Barrett, M. & Glennon, B. In-situ monitoring and characterization of plug flow crystallizers. *Chemical Engineering Science* **77,** 105–111 (2012).

118. Kaveh-Baghbaderani, Y., Blank-Shim, S. A., Koch, T. & Berensmeier, S. Selective release of overexpressed recombinant proteins from e. coli cells facilitates one-step chromatographic purification of peptide-tagged green fluorescent protein variants. *Protein Expression and Purification* **152,** 155–160 (2018).

119. SIMA-tec GmbH. *Technisches Datenblatt CUBE 80-VA* (). `https://www.sima-tec-gmbh.de/unternehmen/downloads/`.

120. Hartinger, M., Heidebrecht, H.-J., Schiffer, S., Dumpler, J. & Kulozik, U. Milk protein fractionation by means of spiral-wound microfiltration membranes: effect of the pressure adjustment mode and temperature on flux and protein permeation. *Foods* **8,** 180 (2019).

121. Zadeh, L. Optimality and non-scalar-valued performance criteria. *IEEE Transactions on Automatic Control* **8,** 59–60 (1963).

122. Hosokawa, K., Goto, J. & Hirayama, N. Prediction of solvents suitable for crystallization of small organic molecules. *Chemical and Pharmaceutical Bulletin* **53,** 1296–1299 (2005).

123. Grozdev, L. *Process development for the biotechnological production and purification of mono-, sesqui- and diterpenes* PhD thesis (Technical University of Munich, 2021). ISBN: 9783843947503.

124. Scientific, T. *Pierce™ BCA Protein Assay Kit* ().

125. Pastor, J. M., Salvador, M., Argandoña, M., Bernal, V., Reina-Bueno, M., Csonka, L. N., Iborra, J. L., Vargas, C., Nieto, J. J. & Cánovas, M. Ectoines in cell stress protection: uses and biotechnological production. *Biotechnology Advances* **28,** 782–801 (2010).

126. Jenkins, A. L., Larsen, R. A. & Williams, T. B. Characterization of amino acids using raman spectroscopy. *Spectrochimica Acta Part A: Molecular and Biomolecular Spectroscopy* **61,** 1585–1594 (2005).

127. Lambert, J. B., Shurvell, H. F., Lightner, D. A. & Cooks, R. G. *Introduction to Organic Spectroscopy* (Macmillan Publishing Company, 1987).

128. Mallamace, F., Corsaro, C., Mallamace, D., Vasi, S., Vasi, C. & Dugo, G. The role of water in protein's behavior: the two dynamical crossovers studied by nmr and ftir techniques. *Computational and Structural Biotechnology Journal* **13,** 33–37 (2015).

129. Morhardt, C., Ketterer, B., Heißler, S. & Franzreb, M. Direct quantification of immobilized enzymes by means of ftir atr spectroscopy–a process analytics tool for biotransformations applying non-porous magnetic enzyme carriers. *Journal of Molecular Catalysis B: Enzymatic* **107,** 55–63 (2014).

130. Larkin, P. & Larkin, P. in *Infrared and Raman Spectroscopy* 2nd ed., 73–115 (Elsevier, Oxford, 2011). doi:10.1016/B978-0-12-386984-5.10006-0. https://www.sciencedirect.com/science/article/pii/B9780123869845100060.

131. Oren, A., Heldal, M., Norland, S. & Galinski, E. A. Intracellular ion and organic solute concentrations of the extremely halophilic bacterium salinibacter ruber. *Extremophiles* **6,** 491–498. ISSN: 1431-0651 (2002).

132. Galinski, E. A. Compatible solutes of halophilic eubacteria: molecular principles, water-solute interaction, stress protection. *Experientia* **49,** 487–496 (1993).

133. Lippert, K. & Galinski, E. A. Enzyme stabilization be ectoine-type compatible solutes: protection against heating, freezing and drying. *Applied Microbiology and Biotechnology* **37,** 61–65 (1992).

134. Raviyan, P., Tang, J. & Rasco, B. A. Thermal stability of α-amylase from aspergillus oryzae entrapped in polyacrylamide gel. *Journal of Agricultural and Food Chemistry* **51,** 5462–5466 (2003).

135. Samborska, K., Guiavarc'h, Y., Van Loey, A. & Hendrickx, M. The thermal stability of aspergillus oryzae alpha-amylase in presence of sugars and polyols. *Journal of Food Process Engineering* **29,** 287–303 (2006).

136. González, M., Argaraña, C. E. & Fidelio, G. D. Extremely high thermal stability of streptavidin and avidin upon biotin binding. *Biomolecular Engineering* **16,** 67–72 (1999).

137. Su, N.-W., Wang, M.-L., Kwok, K.-F. & Lee, M.-H. Effects of temperature and sodium chloride concentration on the activities of proteases and amylases in soy sauce koji. *Journal of Agricultural and Food Chemistry* **53,** 1521–1525 (2005).

138. Giancola, C., De Sena, C., Fessas, D., Graziano, G. & Barone, G. Dsc studies on bovine serum albumin denaturation effects of ionic strength and sds concentration. *International Journal of Biological Macromolecules* **20,** 193–204 (1997).

139. Ahrberg, C. D. & Manz, A. Superheated droplets for protein thermal stability analyses of gfp, bsa and taq-polymerase. *RSC Advances* **6,** 42076–42080 (2016).

140. Hahn, M. B., Solomun, T., Wellhausen, R., Hermann, S., Seitz, H., Meyer, S., Kunte, H.-J., Zeman, J., Uhlig, F. & Smiatek, J. Influence of the compatible solute ectoine on the local water structure: implications for the binding of the protein g5p to dna. *The Journal of Physical Chemistry B* **119,** 15212–15220 (2015).

141. Jebbar, M., Sohn-Bösser, L., Bremer, E., Bernard, T. & Blanco, C. Ectoine-induced proteins in sinorhizobium meliloti include an ectoine abc-type transporter involved in osmoprotection and ectoine catabolism. *Journal of Bacteriology* **187,** 1293–1304 (2005).

142. Zhang, L., Wang, Y., Zhang, C., Wang, Y., Zhu, D., Wang, C. & Nagata, S. Supplementation effect of ectoine on thermostability of phytase. *Journal of Bioscience and Bioengineering* **102,** 560–563 (2006).

143. Borges, N., Ramos, A., Raven, N. D., Sharp, R. J. & Santos, H. Comparative study of the thermostabilizing properties of mannosylglycerate and other compatible solutes on model enzymes. *Extremophiles* **6,** 209–216 (2002).

144. Zaccai, G., Bagyan, I., Combet, J., Cuello, G. J., Demé, B., Fichou, Y., Gallat, F.-X., Galvan Josa, V. M., von Gronau, S. & Haertlein, M. Neutrons describe ectoine effects on water h-bonding and hydration around a soluble protein and a cell membrane. *Scientific Reports* **6,** 1–12 (2016).

145. Arakawa, T. & Timasheff, S. N. The stabilization of proteins by osmolytes. *Biophysical Journal* **47,** 411–414. ISSN: 0006-3495 (1985).

146. Eiberweiser, A., Nazet, A., Kruchinin, S. E., Fedotova, M. V. & Buchner, R. Hydration and ion binding of the osmolyte ectoine. *The Journal of Physical Chemistry B* **119,** 15203–15211 (2015).

147. Yadav, J. K. & Prakash, V. Thermal stability of α-amylase in aqueous cosolvent systems. *Journal of Biosciences* **34,** 377–387 (2009).

148. Sola-Penna, M. & Meyer-Fernandes, J. R. Stabilization against thermal inactivation promoted by sugars on enzyme structure and function: why is trehalose more effective than other sugars? *Archives of Biochemistry and Biophysics* **360,** 10–14 (1998).

149. Ajito, S., Iwase, H., Takata, S.-i. & Hirai, M. Sugar-mediated stabilization of protein against chemical or thermal denaturation. *The Journal of Physical Chemistry B* **122,** 8685–8697 (2018).

150. Soper, A. K., Ricci, M. A., Bruni, F., Rhys, N. H. & McLain, S. E. Trehalose in water revisited. *The Journal of Physical Chemistry B* **122,** 7365–7374 (2018).

151. Di Gioacchino, M., Bruni, F. & Ricci, M. A. Protection against dehydration: a neutron diffraction study on aqueous solutions of a model peptide and trehalose. *The Journal of Physical Chemistry B* **122,** 10291–10295 (2018).

152. Vreeland, R. H., Litchfield, C. D., Martin, E. L. & Elliot, E. Halomonas elongata, a new genus and species of extremely salt-tolerant bacteria. *International Journal of Systematic and Evolutionary Microbiology* **30,** 485–495 (1980).

153. Koch, A. L. Turbidity measurements of bacterial cultures in some available commercial instruments. *Analytical Biochemistry* **38,** 252–259. ISSN: 0003-2697 (1970).

154. Koch, A. L. Some calculations on the turbidity of mitochondria and bacteria. *Biochimica et Biophysica Acta* **51,** 429–441 (1961).

155. Ridley-Thomas, C. I., Austin, A., Lucey, W. P. & Clark, M. J. R. Variability in the determination of ash free dry weight for periphyton communities: a call for a standard method. *Water Research* **23,** 667–670 (1989).

156. Hobmeier, K., Goëss, M. C., Sehr, C., Schwaminger, S., Berensmeier, S., Kremling, A., Kunte, H. J., Pflüger-Grau, K. & Marin-Sanguino, A. Anaplerotic pathways in halomonas elongata: the role of the sodium gradient. *Frontiers in Microbiology* **11,** 2124 (2020).

157. Hecht, A., Endy, D., Salit, M. & Munson, M. S. When wavelengths collide: bias in cell abundance measurements due to expressed fluorescent proteins. *ACS Synthetic Biology* **5,** 1024–1027 (2016).

158. Hermann, L., Mais, C.-N., Czech, L., Smits, S. H. J., Bange, G. & Bremer, E. The ups and downs of ectoine: structural enzymology of a major microbial stress protectant and versatile nutrient. *Biological Chemistry* **401,** 1443–1468 (2020).

159. Kunte, H. J., Espinoza, G. A. & Bilstein, A. (2021).

160. Vreeland, R. H. & Martin, E. L. Growth characteristics, effects of temperature, and ion specificity of the halotolerant bacterium halomonas elongata. *Canadian Journal of Microbiology* **26,** 746–752 (1980).

161. Göller, K., Ofer, A. & Galinski, E. A. Construction and characterization of an nacl-sensitive mutant of halomonas elongata impaired in ectoine biosynthesis. *FEMS Microbiology Letters* **161,** 293–300 (1998).

162. Long, X., Tian, J., Liao, X. & Tian, Y. Adaptations of bacillus shacheensis hna-14 required for long-term survival under osmotic challenge: a multi-omics perspective. *RSC Advances* **8,** 27525–27536 (2018).

163. Cummings, S. P. & Gilmour, D. J. The effect of nacl on the growth of a halomonas species: accumulation and utilization of compatible solutes. *Microbiology* **141,** 1413–1418 (1995).

164. Ono, H., Okuda, M., Tongpim, S., Imai, K., Shinmyo, A., Sakuda, S., Kaneko, Y., Murooka, Y. & Takano, M. Accumulation of compatible solutes, ectoine and hydroxyectoine, in a moderate halophile, halomonas elongata ks3 isolated from dry salty land in thailand. *Journal of Fermentation and Bioengineering* **85,** 362–368 (1998).

165. Schmidt, F. R. Optimization and scale up of industrial fermentation processes. *Applied Microbiology and Biotechnology* **68,** 425–435. ISSN: 1432-0614 (2005).

166. Clarke, K. G. & Clarke, K. G. in *Bioprocess Engineering* 171–188 (Woodhead Publishing, 2013). doi:10.1533/9781782421689.171. https://www.sciencedirect.com/science/article/pii/B9781782421672500090.

167. Mahdinia, E., Cekmecelioglu, D. & Demirci, A. in *Essentials in Fermentation Technology* (ed Berenjian, A.) 213–236 (Springer International Publishing, Cham, 2019). doi:10.1007/978-3-030-16230-6_7. https://doi.org/10.1007/978-3-030-16230-6_7.

168. Hewitt, C. J. & Nienow, A. W. in *Advances in Applied Microbiology* 105–135 (Academic Press, 2007). doi:10.1016/S0065-2164(07)62005-X. https://www.sciencedirect.com/science/article/pii/S006521640762005X.

169. Enfors, S.-O., Jahic, M., Rozkov, A., Xu, B., Hecker, M., Jürgen, B., Krüger, E., Schweder, T., Hamer, G. & O'beirne, D. Physiological responses to mixing in large scale bioreactors. *Journal of Biotechnology* **85,** 175–185 (2001).

170. Cheryan, M. *Ultrafiltration and Microfiltration Handbook* 2nd ed. (CRC press, 1998).

171. Anis, S. F., Hashaikeh, R. & Hilal, N. Microfiltration membrane processes: a review of research trends over the past decade. *Journal of Water Process Engineering* **32,** 100941 (2019).

172. Hashino, M., Hirami, K., Ishigami, T., Ohmukai, Y., Maruyama, T., Kubota, N. & Matsuyama, H. Effect of kinds of membrane materials on membrane fouling with bsa. *Journal of Membrane Science* **384,** 157–165 (2011).

173. Koehler, J. A., Ulbricht, M. & Belfort, G. Intermolecular forces between proteins and polymer films with relevance to filtration. *Langmuir* **13,** 4162–4171 (1997).

174. Saeki, D., Nagashima, Y., Sawada, I. & Matsuyama, H. Effect of hydrophobicity of polymer materials used for water purification membranes on biofilm formation dynamics. *Colloids and Surfaces A: Physicochemical and Engineering Aspects* **506,** 622–628 (2016).

175. Dong, C., He, G., Li, H., Zhao, R., Han, Y. & Deng, Y. Antifouling enhancement of poly (vinylidene fluoride) microfiltration membrane by adding mg (oh) 2 nanoparticles. *Journal of Membrane Science* **387,** 40–47 (2012).

176. Dizge, N., Soydemir, G., Karagunduz, A. & Keskinler, B. Influence of type and pore size of membranes on cross flow microfiltration of biological suspension. *Journal of Membrane Science* **366,** 278–285 (2011).

177. Ho, C.-C. & Zydney, A. L. Effect of membrane morphology on the initial rate of protein fouling during microfiltration. *Journal of Membrane Science* **155,** 261–275 (1999).

178. Baker, R. J., Fane, A. G., Fell, C. J. D. & Yoo, B. H. Factors affecting flux in crossflow filtration. *Desalination* **53,** 81–93 (1985).

179. Rezaei, H., Ashtiani, F. Z. & Fouladitajar, A. Effects of operating parameters on fouling mechanism and membrane flux in cross-flow microfiltration of whey. *Desalination* **274,** 262–271 (2011).

180. Rizki, Z., Janssen, A. E. M., Claassen, G. D. H., Boom, R. M. & van der Padt, A. Multi-criteria design of membrane cascades: selection of configurations and process parameters. *Separation Science and Technology* **237,** 116349 (2020).

181. Marler, R. T. & Arora, J. S. Survey of multi-objective optimization methods for engineering. *Structural and Multidisciplinary Optimization* **26,** 369–395 (2004).

182. Kim, I. Y. & De Weck, O. L. Adaptive weighted sum method for multiobjective optimization: a new method for pareto front generation. *Structural and Multidisciplinary Optimization* **31,** 105–116 (2006).

183. Marler, R. T. & Arora, J. S. The weighted sum method for multi-objective optimization: new insights. *Structural and Multidisciplinary Optimization* **41,** 853–862 (2010).

184. Walters, A. *Downstream process development – microfiltration and crystallization for the purification of a compatible solute* Master's thesis (Technical University of Munich, Jan. 4, 2021).

185. Atra, R., Vatai, G., Bekassy-Molnar, E. & Balint, A. Investigation of ultra-and nanofiltration for utilization of whey protein and lactose. *Journal of Food Engineering* **67,** 325–332 (2005).

186. Shi, X., Tal, G., Hankins, N. P. & Gitis, V. Fouling and cleaning of ultrafiltration membranes: a review. *Journal of Water Process Engineering* **1,** 121–138 (2014).

187. Wang, Y.-N. & Tang, C. Y. Protein fouling of nanofiltration, reverse osmosis, and ultrafiltration membranes—the role of hydrodynamic conditions, solution chemistry, and membrane properties. *Journal of Membrane Science* **376,** 275–282 (2011).

188. She, Q., Tang, C. Y., Wang, Y.-N. & Zhang, Z. The role of hydrodynamic conditions and solution chemistry on protein fouling during ultrafiltration. *Desalination* **249,** 1079–1087 (2009).

189. Baker, R. W. in *Membrane Technology and Applications* 207–251 (John Wiley & Sons, Ltd, 2012). ISBN: 9781118359686. doi:https://doi.org/10.1002/9781118359686.ch5. eprint: https://onlinelibrary.wiley.com/doi/pdf/10.1002/9781118359686.ch5. https://onlinelibrary.wiley.com/doi/abs/10.1002/9781118359686.ch5.

190. Lai, Q. D. & Nguyen, H. D. Enhancement of fish sauce quality by application of nanofiltration. *LWT* **151,** 112181 (2021).

191. Guo, Y., Li, T.-y., Xiao, K., Wang, X.-m. & Xie, Y. F. Key foulants and their interactive effect in organic fouling of nanofiltration membranes. *Journal of Membrane Science* **610,** 118252 (2020).

192. Boussu, K., Belpaire, A., Volodin, A., Van Haesendonck, C., Van der Meeren, P., Vandecasteele, C. & Van der Bruggen, B. Influence of membrane and colloid characteristics on fouling of nanofiltration membranes. *Journal of Membrane Science* **289,** 220–230 (2007).

193. Hughes, D., Taha, T. & Zhanfeng, C. in *Handbook of Food and Bioprocess Modeling Techniques* 145–178 (CRC Press, 2006).

194. Bian, R., Yamamoto, K. & Watanabe, Y. The effect of shear rate on controlling the concentration polarization and membrane fouling. *Desalination* **131,** 225–236 (2000).

195. Shi, X., Tal, G., Hankins, N. P. & Gitis, V. Fouling and cleaning of ultrafiltration membranes: a review. *Journal of Water Process Engineering* **1,** 121–138 (2014).

196. Trinh, T. A., Li, W. & Chew, J. W. Internal fouling during microfiltration with foulants of different surface charges. *Journal of Membrane Science* **602,** 117983 (2020).

197. Bellona, C., Drewes, J. E., Xu, P. & Amy, G. Factors affecting the rejection of organic solutes during nf/ro treatment—a literature review. *Water Research* **38,** 2795–2809 (2004).

198. Contreras, A. E., Kim, A. & Li, Q. Combined fouling of nanofiltration membranes: mechanisms and effect of organic matter. *Journal of Membrane Science* **327,** 87–95 (2009).

199. Garcia-Molina, V., Esplugas, S., Wintgens, T. & Melin, T. Ultrafiltration of aqueous solutions containing dextran. *Desalination* **188,** 217–227 (2006).

200. García-Molina, V., Lyko, S., Esplugas, S., Wintgens, T. & Melin, T. Ultrafiltration of aqueous solutions containing organic polymers. *Desalination* **189,** 110–118 (2006).

201. Rogatsky, E. Pandora box of BCA assay. investigation of the accuracy and linearity of the microplate bicinchoninic protein assay: analytical challenges and method modifications to minimize systematic errors. *Analytical Biochemistry* **631,** 114321 (2021).

202. Cortés-Ríos, J., Zárate, A. M., Figueroa, J. D., Medina, J., Fuentes-Lemus, E., Rodríguez-Fernández, M., Aliaga, M. & López-Alarcón, C. Protein quantification by bicinchoninic acid (BCA) assay follows complex kinetics and can be performed at short incubation times. *Analytical Biochemistry* **608,** 113904 (2020).

203. Wiechelman, K. J., Braun, R. D. & Fitzpatrick, J. D. Investigation of the bicinchoninic acid protein assay: identification of the groups responsible for color formation. *Analytical Biochemistry* **175,** 231–237 (1988).

204. Marshall, A. D., Munro, P. A. & Trägårdh, G. The effect of protein fouling in microfiltration and ultrafiltration on permeate flux, protein retention and selectivity: a literature review. *Desalination* **91,** 65–108 (1993).

205. Baker, R. W. in *Membrane Technology and Applications* 253–302 (John Wiley & Sons, Ltd, 2012). ISBN: 9781118359686. doi:https://doi.org/10.1002/9781118359686.ch6. eprint: https://onlinelibrary.wiley.com/doi/pdf/10.1002/9781118359686.ch6. https://onlinelibrary.wiley.com/doi/abs/10.1002/9781118359686.ch6.

206. Alves, Y. P. C., Antunes, F. A. F., da Silva, S. S. & Forte, M. B. S. From by-to bioproducts: selection of a nanofiltration membrane for biotechnological xylitol purification and process optimization. *Food and Bioproducts Processing* **125,** 79–90 (2021).

207. Baker, R. W. in *Membrane Technology and Applications* 303–324 (John Wiley & Sons, Ltd, 2012). ISBN: 9781118359686. doi:https://doi.org/10.1002/9781118359686.ch7. eprint: https://onlinelibrary.wiley.com/doi/pdf/10.1002/9781118359686.ch7. https://onlinelibrary.wiley.com/doi/abs/10.1002/9781118359686.ch7.

208. Hahn, M. B., Uhlig, F., Solomun, T., Smiatek, J. & Sturm, H. Combined influence of ectoine and salt: spectroscopic and numerical evidence for compensating effects on aqueous solutions. *Physical Chemistry Chemical Physics* **18,** 28398–28402 (2016).

209. Goulas, A. K., Kapasakalidis, P. G., Sinclair, H. R., Rastall, R. A. & Grandison, A. S. Purification of oligosaccharides by nanofiltration. *Journal of Membrane Science* **209,** 321–335 (2002).

210. Mänttäri, M., Pihlajamäki, A., Kaipainen, E. & Nyström, M. Effect of temperature and membrane pre-treatment by pressure on the filtration properties of nanofiltration membranes. *Desalination* **145,** 81–86 (2002).

211. Bandini, S. & Morelli, V. Effect of temperature, ph and composition on nanofiltration of mono/disaccharides: experiments and modeling assessment. *Journal of Membrane Science* **533,** 57–74 (2017).

212. Tsuru, T., Izumi, S., Yoshioka, T. & Asaeda, M. Temperature effect on transport performance by inorganic nanofiltration membranes. *AIChE Journal* **46,** 565–574 (2000).

213. Pontalier, P.-Y., Ismail, A. & Ghoul, M. Mechanisms for the selective rejection of solutes in nanofiltration membranes. *Separation and Purification Technology* **12,** 175–181 (1997).

214. Klamt, A. Conductor-like screening model for real solvents: a new approach to the quantitative calculation of solvation phenomena. *The Journal of Physical Chemistry* **99,** 2224–2235 (1995).

215. Klamt, A. & Eckert, F. COSMO-RS: a novel and efficient method for the a priori prediction of thermophysical data of liquids. *Fluid Phase Equilibria* **172,** 43–72 (2000).

216. Eckert, F. & Klamt, A. Fast solvent screening via quantum chemistry: cosmo-rs approach. *AIChE Journal* **48,** 369–385 (2002).

217. Klamt, A. Prediction of the mutual solubilities of hydrocarbons and water with COSMO-RS. *Fluid Phase Equilibria* **206,** 223–235 (2003).

218. Karpiński, P. H. & Bałdyga, J. in *Handbook of Industrial Crystallization* (eds Myerson, A. S., Erdemir, D. & Lee, A. Y.) 3rd ed., 346–379 (Cambridge University Press, 2019). doi:10.1017/9781139026949.012.

219. Romero, C. M. & Oviedo, C. D. Effect of temperature on the solubility of α-amino acids and α, ω-amino acids in water. *Journal of Solution Chemistry* **42,** 1355–1362 (2013).

220. Held, C., Neuhaus, T. & Sadowski, G. Compatible solutes: thermodynamic properties and biological impact of ectoines and prolines. *Biophysical Chemistry* **152,** 28–39 (2010).

221. Onraedt, A. E., Walcarius, B. A., Soetaert, W. K. & Vandamme, E. J. Optimization of ectoine synthesis through fed-batch fermentation of brevibacterium epidermis. *Biotechnology Progress* **21,** 1206–1212 (2005).

222. Schröder, B., Santos, L. M. N. B. F., Marrucho, I. M. & Coutinho, J. A. P. Prediction of aqueous solubilities of solid carboxylic acids with COSMO-RS. *Fluid Phase Equilibria* **289,** 140–147 (2010).

223. Ruether, F. & Sadowski, G. Modeling the solubility of pharmaceuticals in pure solvents and solvent mixtures for drug process design. *Journal of Pharmaceutical Sciences* **98,** 4205–4215 (2009).

224. Zimmermann, L. *Process optimization – crystallization of an amino acid derivative* Bachelor's thesis (Technical University of Munich, Apr. 1, 2020).

225. Darmali, C., Mansouri, S., Yazdanpanah, N. & Woo, M. W. Mechanisms and control of impurities in continuous crystallization: a review. *Industrial & Engineering Chemistry Research* **58,** 1463–1479 (2018).

226. Paul, E. L., Tung, H.-H. & Midler, M. Organic crystallization processes. *Powder Technology* **150,** 133–143 (2005).

227. Rauls, M., Bartosch, K., Kind, M., Lacmann, R. & Mersmann, A. The influence of impurities on crystallization kinetics–a case study on ammonium sulfate. *Journal of Crystal Growth* **213,** 116–128 (2000).

228. Keshavarz, L., Steendam, R. R. E., Blijlevens, M. A. R., Pishnamazi, M. & Frawley, P. J. Influence of impurities on the solubility, nucleation, crystallization, and compressibility of paracetamol. *Crystal Growth & Design* **19,** 4193–4201 (2019).

229. Pons Siepermann, C. A. & Myerson, A. S. Inhibition of nucleation using a dilute, weakly hydrogen-bonding molecular additive. *Crystal Growth & Design* **18,** 3584–3595 (2018).

230. Podder, J. The study of impurities effect on the growth and nucleation kinetics of potassium dihydrogen phosphate. *Journal of Crystal Growth* **237,** 70–75 (2002).

231. Nicoud, L. H. & Myerson, A. S. in *Handbook of Industrial Crystallization* (eds Myerson, A. S., Erdemir, D. & Lee, A. Y.) 3rd ed., 115–135 (Cambridge University Press, 2019). doi:10.1017/9781139026949.004.

232. Mukuta, T., Lee, A. Y., Kawakami, T. & Myerson, A. S. Influence of impurities on the solution-mediated phase transformation of an active pharmaceutical ingredient. *Crystal Growth & Design* **5,** 1429–1436 (2005).

233. He, Y., Gao, Z., Zhang, T., Sun, J., Ma, Y., Tian, N. & Gong, J. Seeding techniques and optimization of solution crystallization processes. *Organic Process Research & Development* **24,** 1839–1849 (2020).

234. Tung, H.-H. Industrial perspectives of pharmaceutical crystallization. *Organic Process Research & Development* **17,** 445–454 (2013).

235. Lewis, A., Seckler, M., Kramer, H. & van Rosmalen, G. in *Industrial Crystallization: Fundamentals and Applications* 1–25 (Cambridge University Press, 2015). doi:10.1017/CBO9781107280427.002.

236. Edgar, R., Schultz, T. M., Rasmussen, F. B., Feidenhans'l, R. & Leiserowitz, L. Solvent binding to benzamide crystals: morphology, induced twinning and direct observation by surface x-ray diffraction. *Journal of the American Chemical Society* **121,** 632–637 (1999).

237. Williams-Seton, L., Davey, R. J. & Lieberman, H. F. Solution chemistry and twinning in saccharin crystals: a combined probe for the structure and functionality of the crystal-fluid interface. *Journal of the American Chemical Society* **121,** 4563–4567 (1999).

238. Davey, R. J., Schroeder, S. L. M. & Ter Horst, J. H. Nucleation of organic crystals—a molecular perspective. *Angewandte Chemie International Edition* **52,** 2166–2179 (2013).

239. Wang, H., Wang, Z., Liu, L., Gong, X. & Wang, M. Alumina hydrate polymorphism control in al–water reaction crystallization by seeding to change the metastable zone width. *Crystal Growth & Design* **16,** 1056–1062 (2016).

240. Wan, P. K., Lan, J. C.-W., Chen, P.-W., Tan, J. S. & Ng, H. S. Recovery of intracellular ectoine from halomonas salina cells with poly (propylene) glycol/salt aqueous biphasic system. *Journal of the Taiwan Institute of Chemical Engineers* **82,** 28–32 (2018).

241. Ng, H. S., Wan, P. K., Ng, T.-C. & Lan, J. C.-W. Primary purification of intracellular halomonas salina ectoine using ionic liquids-based aqueous biphasic system. *Journal of Bioscience and Bioengineering* **130,** 200–204 (2020).

242. Chen, R., Zhu, L., Lv, L., Yao, S., Li, B. & Qian, J. Optimization of the extraction and purification of the compatible solute ectoine from halomonas elongate in the laboratory experiment of a commercial production project. *World Journal of Microbiology and Biotechnology* **33,** 116. ISSN: 1573-0972 (2017).

243. Cui, Z. F., Jiang, Y., Field, R. W., Cui, Z. F. & Muralidhara, H. S. in *Membrane Technology* 1–18 (Butterworth-Heinemann, Oxford, 2010). doi:10.1016/B978-1-85617-632-3.00001-X. https://www.sciencedirect.com/science/article/pii/B978185617632300001X.

244. Besenhard, M. O., Neugebauer, P., Scheibelhofer, O. & Khinast, J. G. Crystal engineering in continuous plug-flow crystallizers. *Crystal Growth & Design* **17,** 6432–6444 (2017).

List of Figures

List of Tables

A Appendix

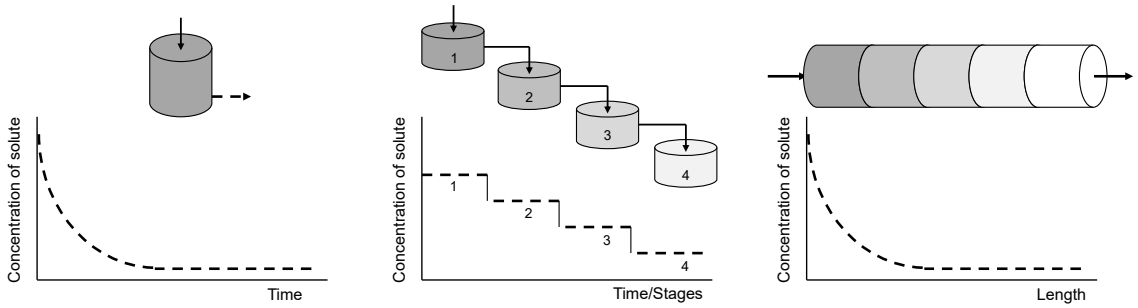

(a) Batch reactor. **(b)** *CSTR/MSMPR*. **(c)** *PFR*.

Figure A.1: Schema of operation modes for crystallization. While in the standard batch reactor (a), a batch process happens, continuous stirred-tank reactor (*CSTR*)/mixed suspension mixed product removal (*MSMPR*) and plug-flow *PF*) reactors are used for a continuous process. Adapted from Hu [109]

.

Table A.1: Balance of filtration cascade, for the target molecule γ-NADA, consisting of serial *MF*, *UF* and *NF* step. Cascade was performed with the respective membranes and conditions from the screening in subsection 4.3.1. permeate of the prior step was used as feed in *UF* and *NF*. Filtration was performed with the broth from *H. elongata* ΔectC cultivation in MM63 medium with 1 M NaCl (data not shown).

Process step	$\mathbf{c}_{before}$ [g $\mathbf{L}^{-1}$]	$\mathbf{c}_{after}$ [g $\mathbf{L}^{-1}$]	$\mathbf{V}_{before}$ [L]	$\mathbf{V}_{after}$ [L]	$\mathbf{m}_{before}$ [g]	$\mathbf{m}_{after}$ [g]	**VCF** [-]	**CF** [-]	**Yield** [%]	**Recovery** [%]	**Purity** [%]
Microfiltration	2.3±0.0	2.5±0.1	1.2	0.8	2.7±0.0	2.0±0.1	1.5	1.1±0.0	75.2±3.8	74.9±1.1	13.0±1.1
Ultrafiltration	1.8±0.0	2.1±0.3	0.8	0.6	1.4±0.0	1.3±0.2	1.3	1.2±0.1	94.5±18.1	80.8±0.0	10.1±5.2
Nanofiltration	1.5±0.0	3.36±0.0	0.6	0.1	1.0±0.0	0.3±0.0	6.4	2.2±0.0	72.4±4.6	34.2±0.5	20.6±5.3
Total	2.3±0.0	3.36±0.0	1.2	0.1	2.7±0.0	0.3±0.0	11.9	1.5±0.0	26.1±1.7	12.3±0.2	20.6±5.3

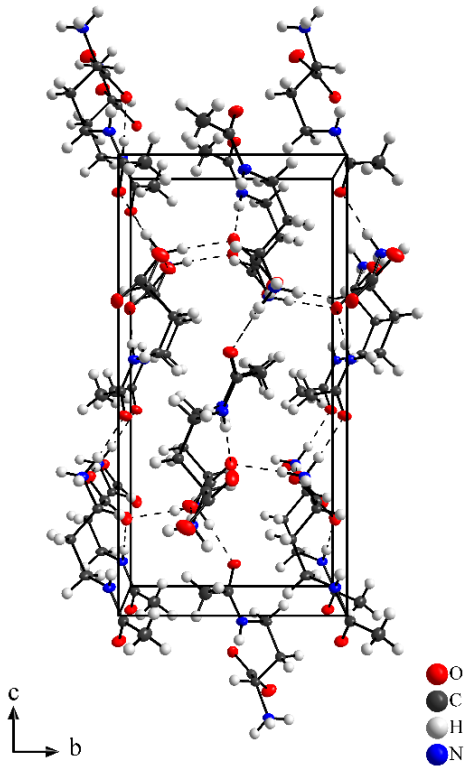

Figure A.2: Three dimensional orientation of γ–NADA molecules in the crystal lattice. Atoms are assigned as followed: carbon (C) as black, hydrogen (H) as white, oxygen (O) as red, and nitrogen (N) as blue. Adapted from [100].

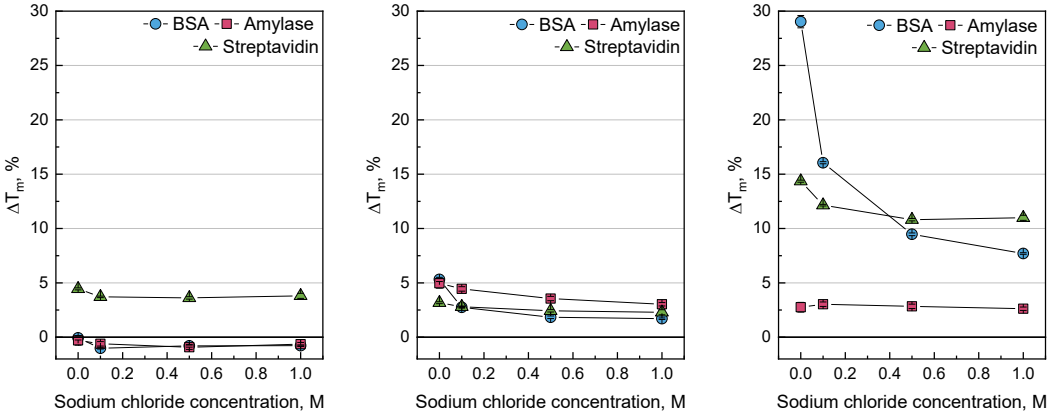

(a) Ectoine. **(b)** Hydroxyectoine. **(c)** γ–NADA.

Figure A.3: Percentage difference in thermal unfolding temperature ΔT_m between stabilized protein with the compatible solutes ectoine (a), hydroxyectoine (b) and γ–NADA (c) and native protein stability in a NaCl range of 0 - 1.0 M. All experiments were performed in 10 mM potassium phosphate buffer pH 7.6 with 0.5 g L^{-1} protein and 0.5 M compatible solute.

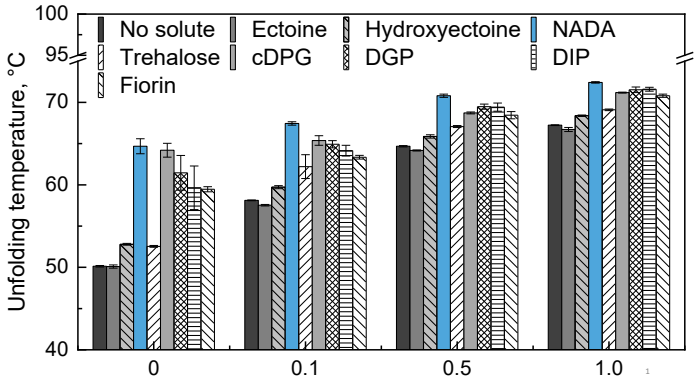

Figure A.4: Unfolding temperatures of 0.5 g L^{-1} BSA with 0.5 M of various compatible solutes at 0, 0.1, 0.5 an 1 M sodium chloride in 10 mM potassium phosphate buffer pH 7.6.

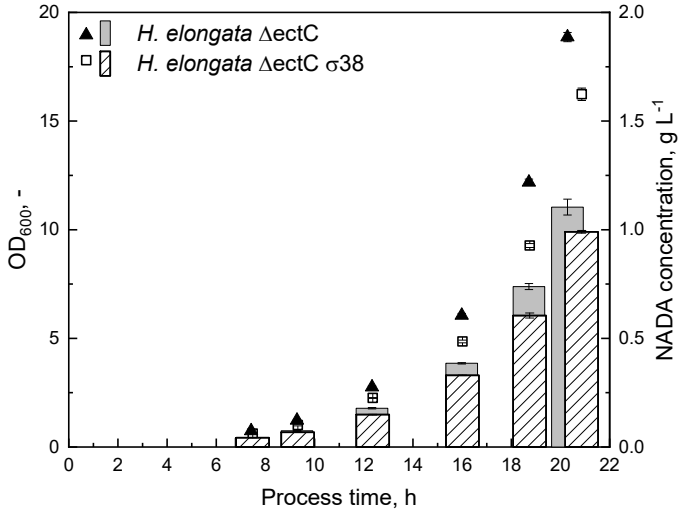

Figure A.5: Cultivation of *H. elongata* ΔectC and *H. elongata* ΔectC σ38 in MM63 medium, supplemented with 15 g L^{-1} glucose and 1 M NaCl. Cultivation was performed as described in subsection 4.2.2 in 1.5 L working volume. Scatter plot and bar charts represent OD_{600} and γ-NADA concentration, respectively for the respective *H. elongata* mutant.

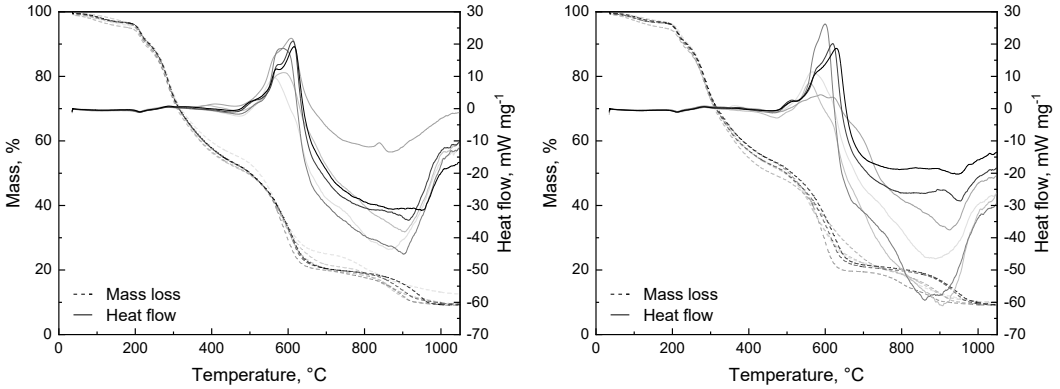

(a) *H. elongata* ΔectC. **(b)** *H. elongata* ΔectC σ38.

Figure A.6: Mass loss and heat flow per biomass data from thermal gravimetric analysis (*TGA*) for the calculation of OD-AFDW correlation (Figure A.7 and Figure 4.5) of *H. elongata* ΔectC (a) and *H. elongata* ΔectC σ38 (b) cultivation in MM63 minimal medium with 1 M NaCl. Increasing sample OD_{600} is shown in increasing grey scale.

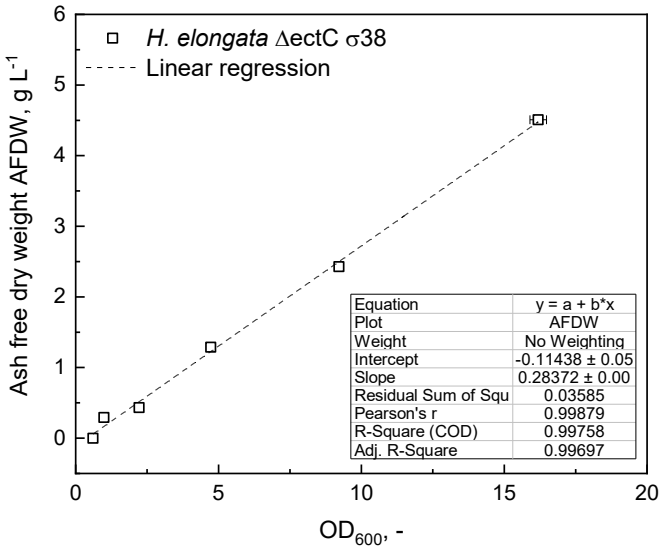

Figure A.7: Correlation of the optical density OD_{600} and the ash free dry weight *AFDW* of *Halomonas elongata* ΔectC σ38, cultivated in MM63 minimal medium with 1 M NaCl.

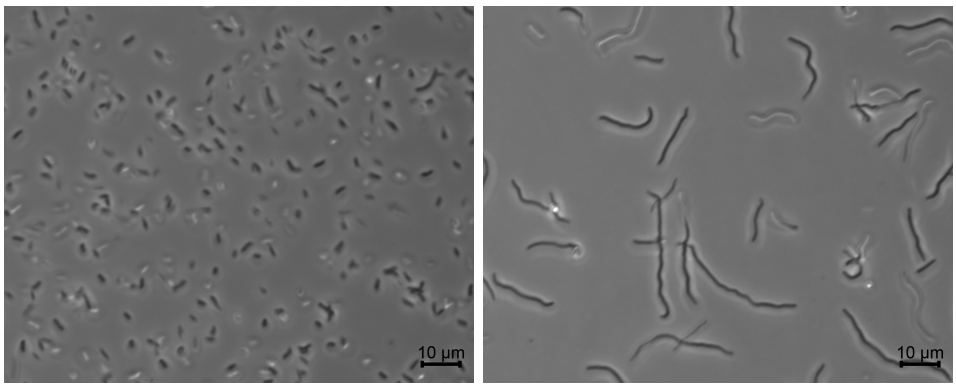

(a) σ38 in exponential phase. **(b)** σ38 in stationary phase.

Figure A.8: *H. elongata* ΔectC σ38 in both, exponential and stationary phase grown in LB complex medium with 1 M NaCl. Microscope pictures were taken in phase-contrast mode, 40x magnification and additional 2.5x optovar magnification (*Axio Observer 7, Carl Zeiss Microscopy Deutschland GmbH, Oberkochen, Germany*).

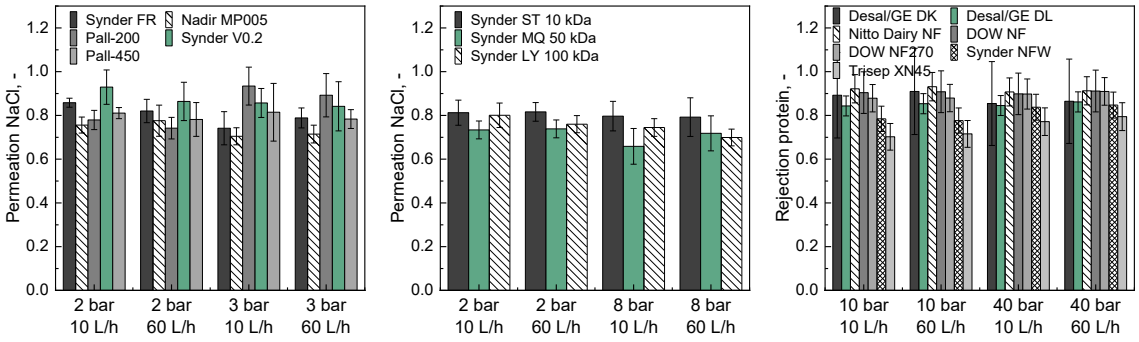

(a) *MF* - NaCl permeation. **(b)** *UF* - NaCl permeation. **(c)** *NF* - protein rejection.

Figure A.9: Rejection and permeation of NaCl and protein in the membrane screening under the respective conditions for the different filtration pore size; microfiltration(a), ultrafiltration (b) and nanofiltration (c)

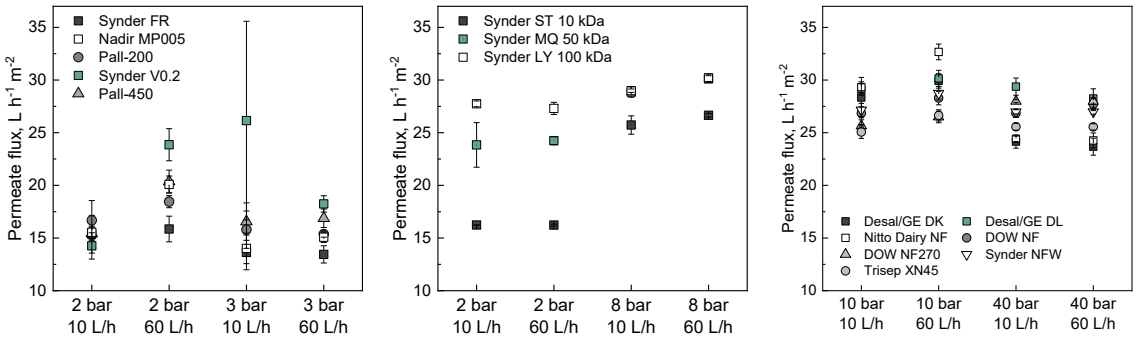

(a) Microfiltration. **(b)** Ultrafiltration. **(c)** Nanofiltration.

Figure A.10: Permeat flux during the screening of microfiltration (a), ultrafiltration (b) and nanofiltration (c) membranes at the respective *TMP* and Q_F conditions.

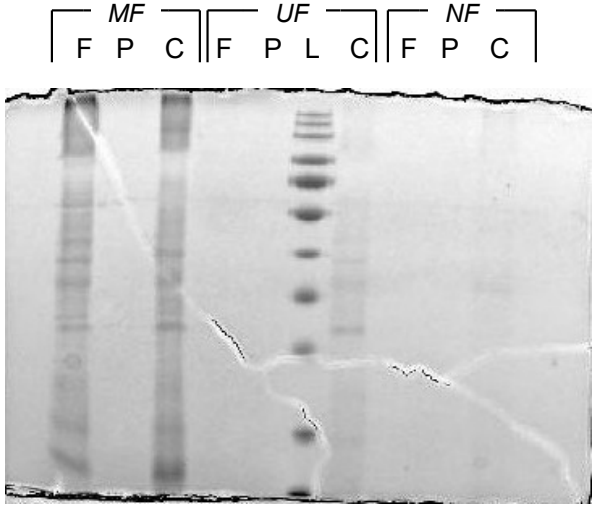

Figure A.11: *SDS*-page of filtration cascade process showing the protein content in the respective feed (F), permeate (P) and concentrate (C) samples.

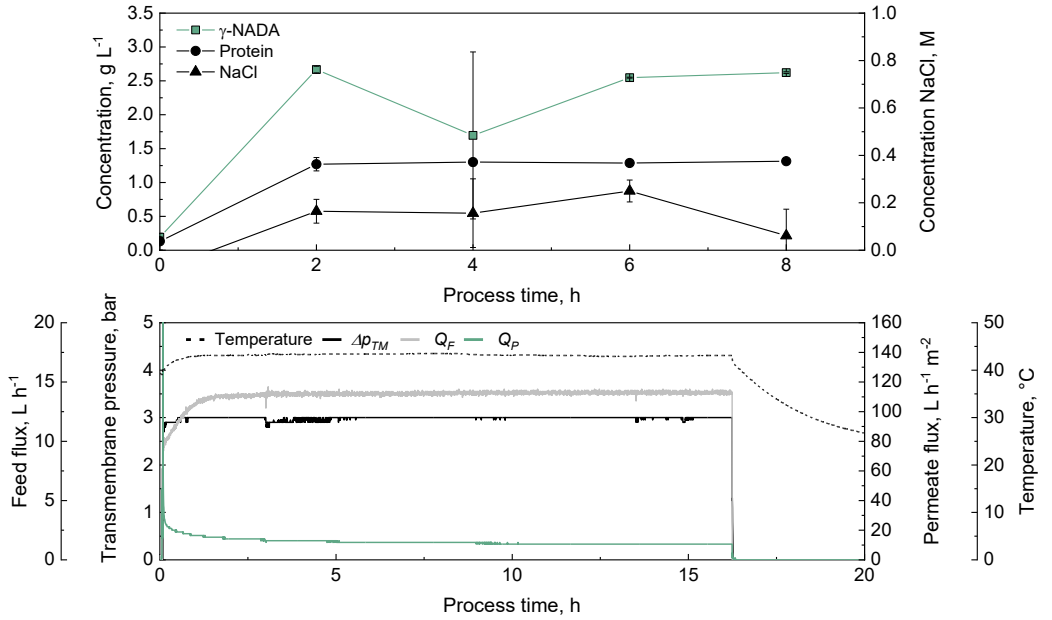

Figure A.12: Second longterm *MF* process for the purification of γ-NADA with the previously screened *Synder V0.2* membrane and with 3 bar and 10 L h^{-1} for Δp_{TM} and Q_F, respectively (see subsection 4.3.1). Permeate samples were taken periodically over the process and γ-NADA, protein and NaCl content was analyzed as described in subsection 3.2.6. Temperature, Δp_{TM}, Q_F and Q_P were recorded online.

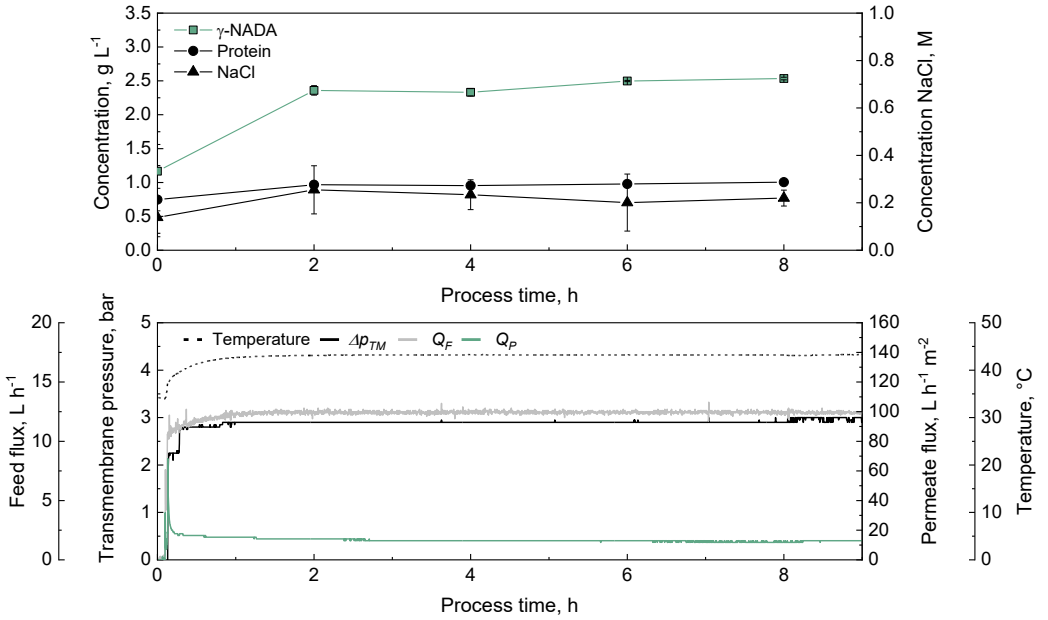

Figure A.13: Third longterm *MF* process for the purification of γ-NADA with the previously screened *Synder V0.2* membrane and with 3 bar and 10 L h^{-1} for Δp_{TM} and Q_F, respectively (see subsection 4.3.1). Permeate samples were taken periodically over the process and γ-NADA, protein and NaCl content was analyzed as described in subsection 3.2.6. Temperature, Δp_{TM}, Q_F and Q_P were recorded online.

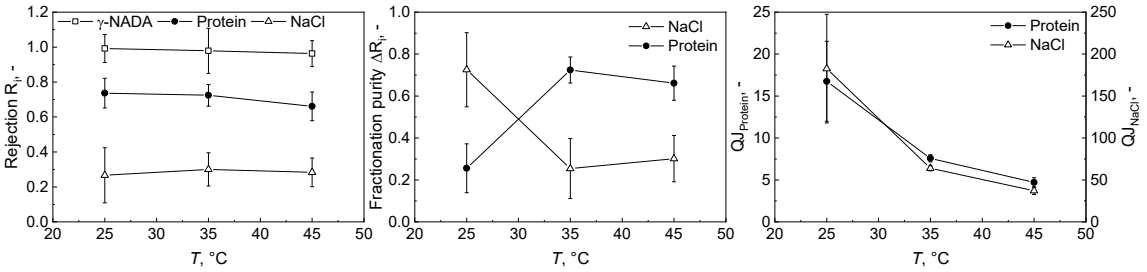

(a) $\Delta ptm = 5$ bar.

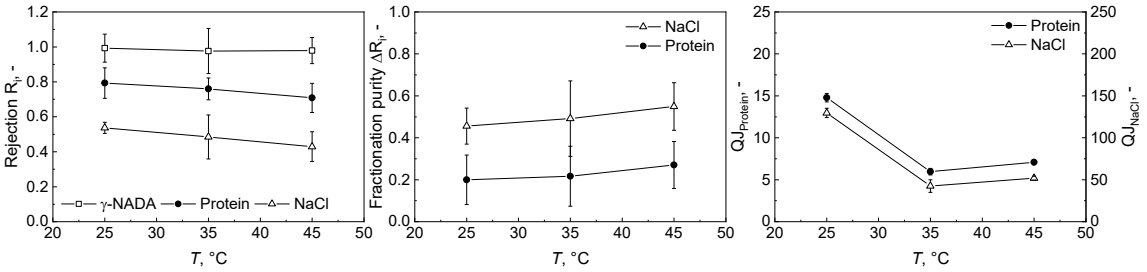

(b) $\Delta ptm = 20$ bar.

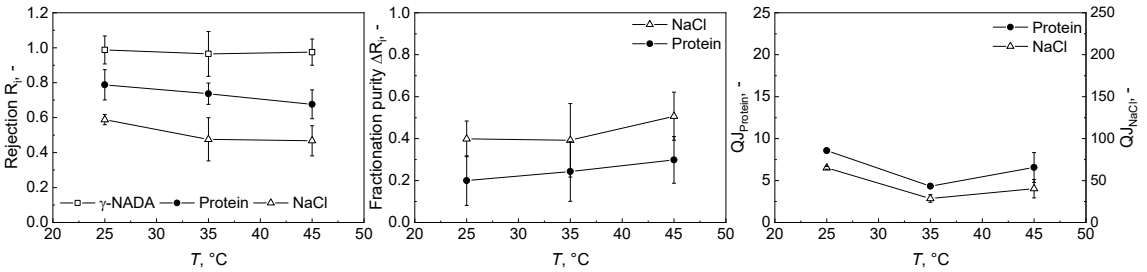

(c) $\Delta ptm = 30$ bar.

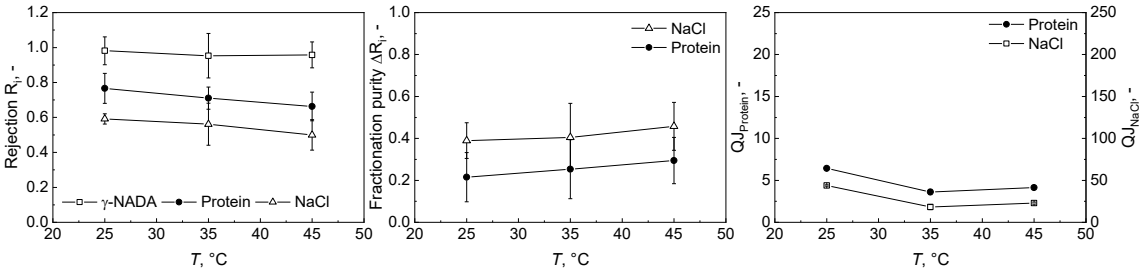

(d) $\Delta ptm = 40$ bar.

Figure A.14: Impact of the temperature on the rejection R_i, the fractionation purity ΔR_S and the ratio of the permeat fluxes of NADA and the impurities - protein ($QJ_{Protein}$) and NaCl (QJ_{NaCl}) at 5 bar (a), 20 bar (b), 30 bar (c) and 40 bar (d) transmembrane pressure Δptm.

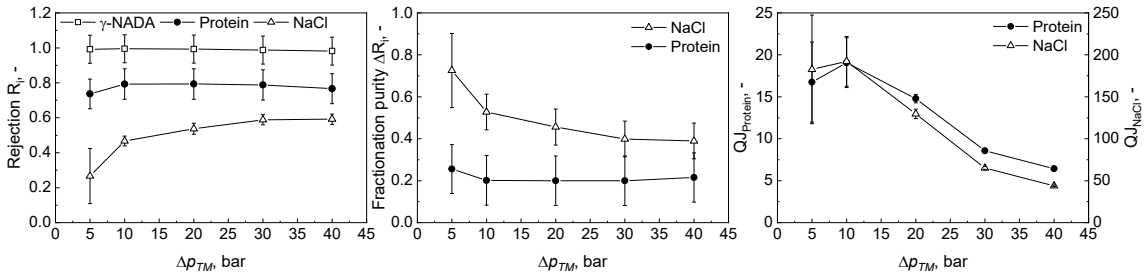

(a) $T = 25$ °C.

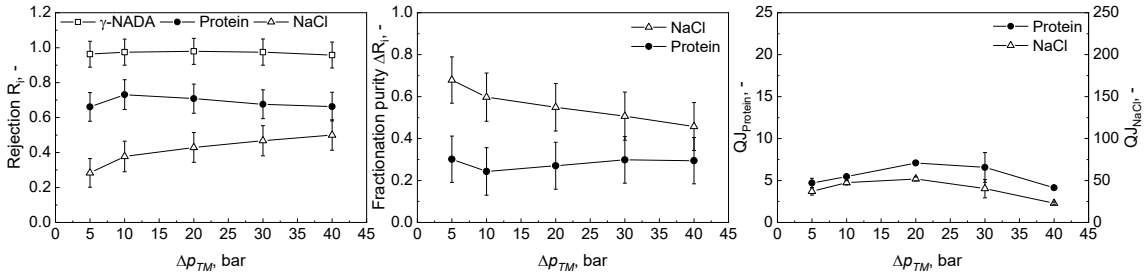

(b) $T = 45$ °C.

Figure A.15: Impact of the transmembrane pressure on the rejection R_i, the fractionation purity ΔR_S and the ratio of the permeat fluxes of NADA and the impurities - protein ($QJ_{Protein}$) and NaCl (QJ_{NaCl}) at 25 °C (a) and 45 °C (b).

(a) 0.1 K min^{-1}.

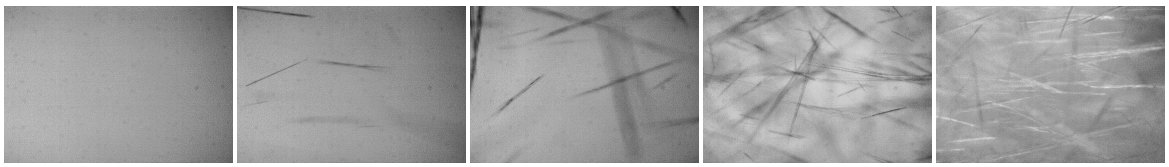

(b) 1 K min^{-1}.

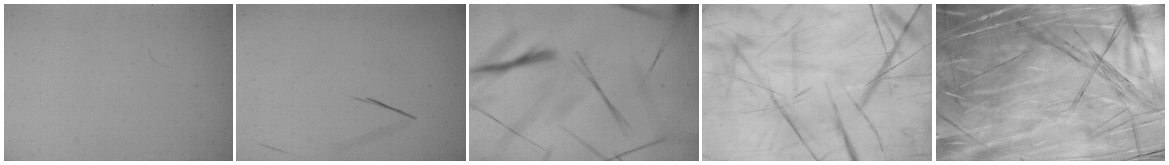

(c) 10 K min^{-1}.

Figure A.16: Selection of inline microscopy picture (*particle vision and measurement, PVM; Mettler Toledo Inc.*) of the γ–NADA crystallization process in a 500 mL reactor system (*OptiMax 1001 Synthesis workstation, Mettler Toledo Inc*). Crystallization was performed in H_2O with cooling a saturated solution of hydrolyzed ectoine material from 50 to 20 °C with different cooling rates of 0.1 K min^{-1} (a), 1 K min^{-1} (b) and 10 K min^{-1} (c). Stirring was set constant to 300 rpm.

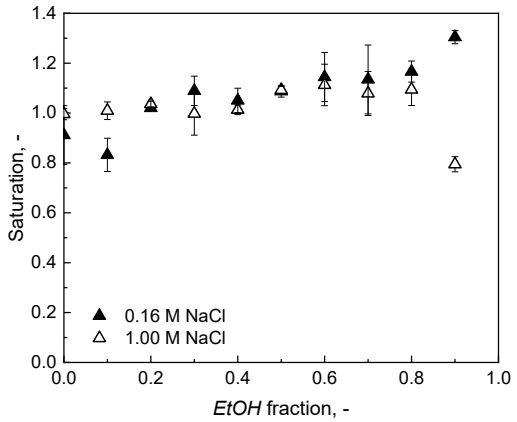

Figure A.17: Saturation of NaCl in H_2O with increasing *EtOH* fractions.

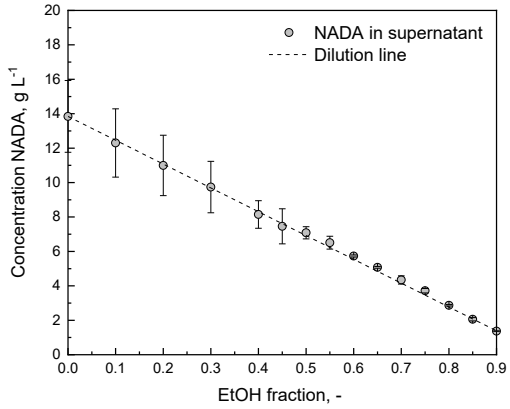

(a) Standard antisolvent crystallization.

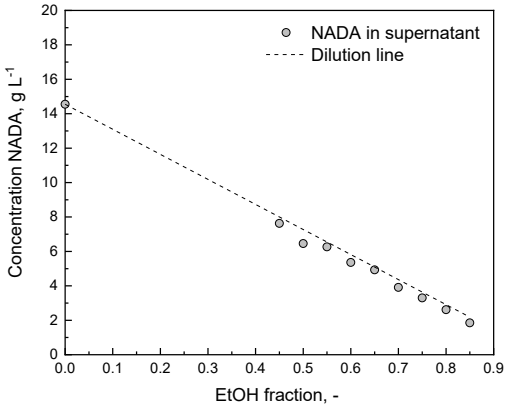

(b) Crystallization step to 45 % EtOH.

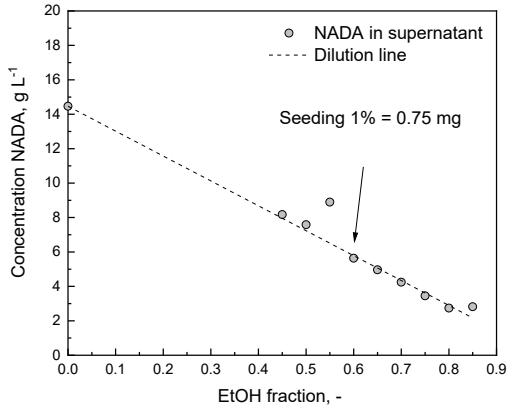

(c) Crystallization with seeding.

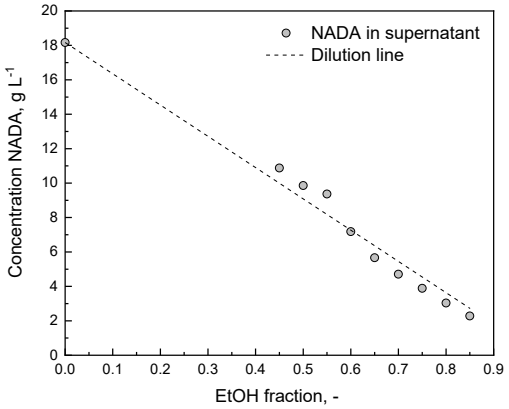

(d) Crystallization with isopropanol.

Figure A.18: Antisolvent crystallization of NADA from fermentation after nanofiltration. *EtOH* was used as antisolvent with an initial 45 % solvent step to exclude organic impurities.